Applied Physics Reviews

REVIEW ARTICLE | JANUARY 19 2024

Emerging optoelectronic artificial synapses and memristors based on low-dimensional nanomaterials

Pengshan Xie ; Dengji Li ; SenPo Yip; Johnny C. Ho

Appl. Phys. Rev. 11, 011303 (2024)
https://doi.org/10.1063/5.0173547

Applied Physics Reviews REVIEW pubs.aip.org/aip/are

Emerging optoelectronic artificial synapses and memristors based on low-dimensional nanomaterials

Cite as: Appl. Phys. Rev. **11**, 011303 (2024); doi: 10.1063/5.0173547
Submitted: 22 August 2023 · Accepted: 21 November 2023 ·
Published Online: 19 January 2024

Pengshan Xie,[1] Dengji Li,[1] SenPo Yip,[2] and Johnny C. Ho[1,2,3,a)]

AFFILIATIONS

[1]Department of Materials Science and Engineering, City University of Hong Kong, Kowloon, Hong Kong 999077, China
[2]Institute for Materials Chemistry and Engineering, Kyushu University, Fukuoka 816-8580, Japan
[3]State Key Laboratory of Terahertz and Millimeter Waves, City University of Hong Kong, Kowloon, Hong Kong 999077, China

[a)]**Author to whom correspondence should be addressed:** johnnyho@cityu.edu.hk

ABSTRACT

The Von Neumann architecture has been the foundation of modern computing systems. Still, its limitations in processing large amounts of data and parallel processing have become more apparent as computing requirements increase. Neuromorphic computing, inspired by the architecture of the human brain, has emerged as a promising solution for developing next-generation computing and memory devices with unprecedented computational power and significantly lower energy consumption. In particular, the development of optoelectronic artificial synaptic devices has made significant progress toward emulating the functionality of biological synapses in the brain. Among them, the potential to mimic the function of the biological eye also paves the way for advancements in robot vision and artificial intelligence. This review focuses on the emerging field of optoelectronic artificial synapses and memristors based on low-dimensional nanomaterials. The unique photoelectric properties of these materials make them ideal for use in neuromorphic and optoelectronic storage devices, with advantages including high carrier mobility, size-tunable optical properties, and low resistor–capacitor circuit delay. The working mechanisms, device structure designs, and applications of these devices are also summarized to achieve truly sense-storage-computer integrated optoelectronic artificial synapses.

TABLE OF CONTENTS

I. INTRODUCTION

The Von Neumann architecture, named after mathematician and computer scientist John von Neumann, is the cornerstone of modern

computing systems. However, with the continuous increase in the requirements for ultramodern computing, some shortcomings of the Von Neumann architecture are constantly amplified. One of the most significant limitations is the bottleneck caused by processing large amounts of data or running multiple programs simultaneously.[1,2] Additionally, the architecture does not take full advantage of parallel processing, which can limit its ability to handle complex computational tasks. In order to break through the limitations of traditional architecture, neuromorphic computing, inspired by the architecture of the human brain, gradually became the basis for the development of next-generation computing and memory devices.[3,4] This emerging technology shows excellent potential to provide unprecedented computational power while consuming significantly less energy than traditional computing systems. To better match the progress of the algorithm, artificial synaptic devices, specifically optoelectronic synaptic devices, have made significant progress in recent years toward emulating the functionality of biological synapses in the brain.[5–7]

Among the many different types of artificial synaptic devices, the optoelectronic artificial synapses that can mimic and even surpass the function of the human eyes are the most important. The human eye acts as a window to perceive the world; about 80% of external information is received by the human visual system.[8] The incident light contains information about wavelength, intensity, and frequency detected by the retina. Then, the optical signal is converted to neural pulses and transmitted to the brain via optical nerves and synapses.[9] Therefore, mimicking the function of visual perception will be a critical step toward robot vision and artificial intelligence (AI).[10] Currently, the mechanism to realize the artificial vision function includes trap states, band engineering, floating gate, phase change, ferroelectric polarization, etc.[11] Moreover, the optoelectronic memristors, as an important part of realizing visual neuromorphic computing, have also been vigorously developed, which can be realized by constructing metal conducting filament. Compared with electronic synaptic devices and memristors, optoelectronic devices have multiple advantages in application scenarios and performance.[12] On the one hand, the information of light signals, including color, intensity, and frequency, can be extracted by the optoelectronic synaptic devices and memristors. At the same time, the optoelectronic devices can integrate visual and electrical signals, information processing, and data memory under optoelectronic synergy.[13] On the other hand, owing to the unique advantages of broad bandwidth, high interference immunity, low resistor–capacitor circuit delay, and energy efficiency, the optoelectronic synaptic devices and memristors demonstrate the benefits in wider bandwidth, lower interconnection energy consumption, and ultrafast signal transmission.[14]

In recent decades, with the flourishing development of semiconductor materials, nanomaterial-based artificial optoelectronic synaptic devices based on zero-dimensional (0D), one-dimensional (1D), and two-dimensional (2D) materials have gained significant attention due to the unique photoelectric properties.[15–17] The high surface-to-volume ratio, clean interface without dangling bonds, high carrier mobility, and size-tunable optical properties build the performance advantages of low-dimensional materials in optoelectronic synaptic devices and memristors.[18,19]

Here, we focus on the emerging optoelectronic artificial synapses and optoelectronic memristors based on low-dimensional nanomaterials. We first introduce the device materials with different dimensions and then explain the working mechanisms of neuromorphic and optoelectronic storage devices. Section III demonstrates the different device structure designs, including different terminals and layouts. Finally, we also summarize the applications of optoelectronic artificial synapses for visual sensor systems and optoelectronic memristors. Concluding with a future outlook, we describe the important issues and obstacles that must be considered in artificial visual systems and memristors for truly human-like dynamic perception. Figure 1 shows the working mechanisms and applications of optoelectronic artificial synapses and memristors based on low-dimensional nanomaterials.

II. SYNTHESIS METHODS AND NANOSTRUCTURES OF LOW-DIMENSIONAL NANOMATERIALS

A. Zero-dimensional materials

The 0D materials, which consist of nanoparticles and quantum dots (QDs), are characterized by their size being confined in all three dimensions, generally twice smaller than the corresponding exciton Bohr radius of their semiconductor counterparts. These materials exhibit high quantum efficiency and size effect, which leads to a modulated absorption edge.[17,20] Owing to the special structures, the 0D materials demonstrate unique photoelectric properties, including several surface effects, quantum confinement effects, coulomb blockade effects, quantum hall effects, quantum tunneling effects, and so on.[21–23] Currently, 0D materials can be made from various materials, including metals, semiconductors, carbon-based, and oxides.[24] To develop a multi-purpose and high-performance neuromorphic visual system, optoelectronic sensors with ultrahigh responsivity, detectivity, and signal-to-noise ratio are necessary.[25] Therefore, the most widely used 0D materials are based on perovskites, metal, metal chalcogenides, and carbon materials for artificial visual systems.[26–29] Zhu *et al.* applied the all-inorganic perovskite $CsPbBr_3$ QDs to construct the flexible ultrasensitive optoelectronic sensor array for neuromorphic vision systems [Fig. 2(a)].[30] Sun *et al.* adopted CdSe/ZnS core–shell QDs as the light absorption layer combined with MoS_2 to construct the neuromorphic optoelectronic synaptic transistors.[31] Moreover, as shown in Fig. 2(b), a mixed-component quantum dot film was used by Jo *et al.* to realize retina-inspired color-cognitive learning.[32] The mixed QDs with different absorption bands can effectively simulate the retina's response to different light colors. In addition to that, lead-free nanocrystals (NCs) (such as $Cs_3Bi_2I_9$) were also introduced into the devices to fabricate the artificial optoelectronic synapse.[33]

At present, for different material systems, the preparation methods are also diverse. The mainstream methods for synthesizing 0D materials are mainly chemical vapor deposition (CVD), sol-gel, molecular beam epitaxy (MBE), chemical/liquid exfoliation, solvothermal method, hydrothermal method, and so on.[17] Among the many preparation methods, self-assembly methods have become popular for synthesizing 0D materials. Molecules or nanoparticles can spontaneously arrange themselves into a desired structure or pattern by leveraging non-covalent interactions, such as van der Waals (vdW) forces, hydrogen bonding, or electrostatic interactions. Under the framework of self-assembly, different preparation methods, including hydrothermal, solvothermal, spin-coating, and drop-coating, are utilized to fabricate 0D materials. Zhao *et al.* synthesized SnO_2 quantum dots/graphene oxide (GO) by the hydrothermal method.[34] Graphene oxide, which possesses numerous functional groups, is an ideal template for the targeted heterogeneous nucleation and growth of SnO_2 QDs. In the hydrothermal process, the abundant functional groups on GO can

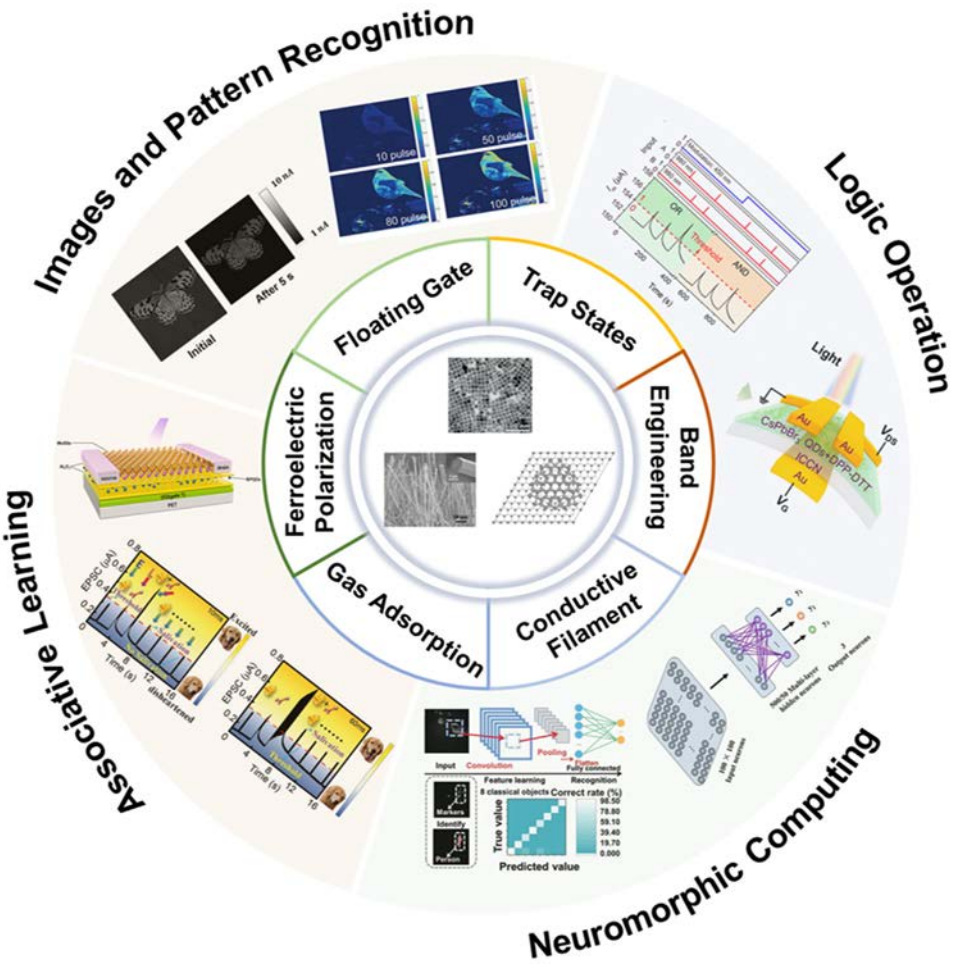

FIG. 1. Schematic of the working mechanisms and applications of optoelectronic artificial synapses and memristors based on low-dimensional nanomaterials. Transmission electron microscope (TEM) overview images of $CsPbI_3$ nanocrystals (NCs). Reproduced with permission from Tong *et al.*, Angew. Chem., Int. Ed. **55**, 13887–13892 (2016).[46] Copyright 2016 Wiley-VCH. Scanning electron microscopy (SEM) image of ZnO nanowires (NWs); inset SEM image is an enlarged view of the NW. Reproduced with permission from Hu *et al.*, Nano Energy **89**, 106282 (2021).[62] Copyright 2021 Elsevier. Alignment of single-crystalline 2D islands. Reproduced with permission from Dong *et al.*, Nat. Commun. **11**, 5862 (2020).[106] Copyright 2020 Springer Nature. Image racemization under 405 nm light. Reproduced with permission from Zhu *et al.*, Nat. Commun. **12**, 1798 (2021).[30] Copyright 2021 Springer Nature. The difference of the color with the increasing number of light pulses. Reproduced with permission from Shao *et al.*, Adv. Mater. **35**, 2208497 (2023).[220] Copyright 2023 Wiley-VCH. Two logic functions realized by using two different light inputs. Reproduced with permission from Hou *et al.*, ACS Nano **15**, 1497–1508 (2021).[237] Copyright 2021 American Chemical Society. Schematic of the flexible synaptic devices array. Reproduced with permission from Zhang *et al.*, Nano Energy **95**, 106987 (2022).[239] Copyright 2022 Elsevier. Recognition for the tagged objects with an already trained convolutional neural network (CNN). Reproduced with permission from Zhu *et al.*, Adv. Mater. **35**, 2301468 (2023).[254] Copyright 2023 Wiley-VCH. Neuron network structure for pattern recognition. Reproduced with permission from Liu *et al.*, ACS Nano **16**, 2282–2291 (2022).[255] Copyright 2022 American Chemical Society. Pavlov associative learning and extinction are mimicked by the devices.[138] Reproduced with permission from Cheng *et al.*, Small **16**, 2005217 (2020). Copyright 2020 Wiley-VCH. Schematic diagram of the heterojunction based on 0D materials. Reproduced with permission from Meng *et al.*, Nano Energy **83**, 105815 (2021).[256] Copyright 2021 Elsevier.

facilitate the *in situ* oxidation of Sn^{2+} ions, followed by the heterogeneous nucleation and growth of SnO_2 QDs on the surface of GO. Meng *et al.* adopted a one-pot solvothermal approach to synthesize a hybrid material system of $CuInS_2$ QDs supported on reduced graphene oxide (rGO) sheets.[35] Moreover, the all-inorganic cesium lead halide ($CsPbX_3$, X = Cl, Br, I) perovskite NCs were also synthesized by a simple solvothermal method.[36] For spin-coating and drop-coating methods, these two methods typically necessitate using templates, which can be self-assembled into colloidal crystals with well-defined sizes and geometry or produced as nanospheres using lithography.[37,38]

In situ synthesis refers to a method of preparing nanomaterials through either *in situ* crystallization or *in situ* polymerization.[39] Chemical vapor deposition (CVD) is one of the most widely used *in situ* growth methods, which is also used to synthesize 0D materials. Compared with other methods, the CVD offers several advantages, including controllable material composition, highly crystalline, and controlled size of 0D materials [Fig. 2(c)].[40] Liu *et al.* developed the quasi-equilibrium plasma-enhanced chemical vapor deposition (qe-PECVD) to produce graphene quantum dots (GQDs) directly on SiO_2/Si [Fig. 2(d)]. The sizes of the GQDs could be controlled from

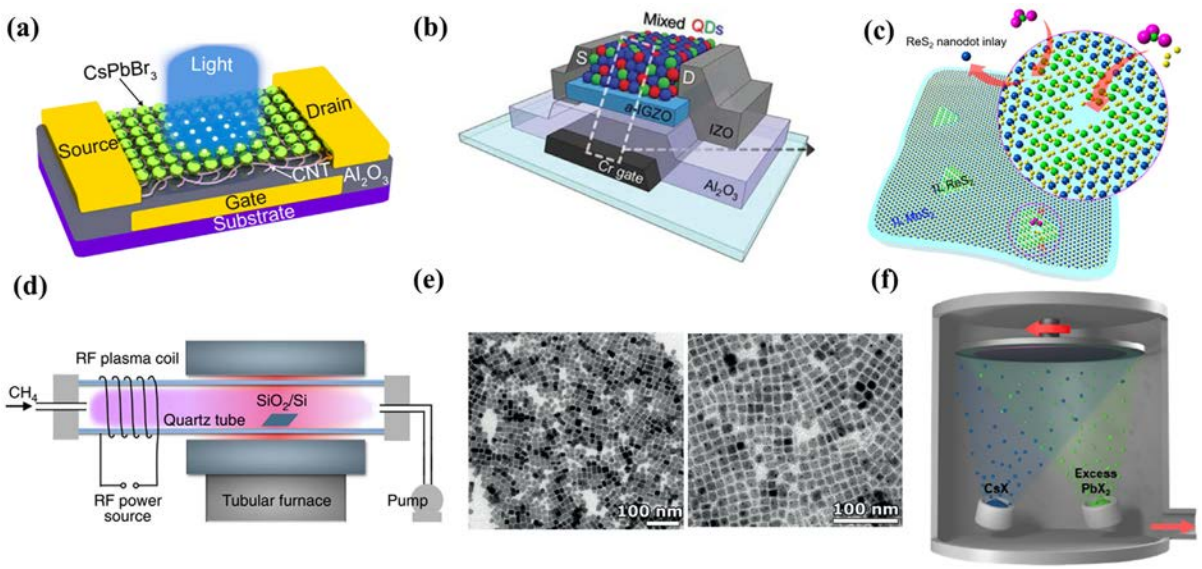

FIG. 2. (a) Schematic of the devices based on the heterojunction of carbon nanotube (CNT)/$CsPbBr_3$-QD.[30] The 40-nm-thick Al_2O_3 dielectric layer was fabricated by atomic layer deposition (ALD), and Ti/Au (5/50 nm) was applied for the electrodes. Reproduced with permission from Zhu *et al.*, Nat. Commun. **12**, 1798, (2021). Copyright 2021 Springer Nature. (b) A schematic device structure of the mixed QD/*a*-indium–gallium–zinc oxide (IGZO) phototransistor.[32] The mixed QDs were composed of CdS QDs, CdSe QDs, and CdSe QDs. Reproduced with permission from Jo *et al.*, Adv. Mater. **34**, 2108979 (2022). Copyright 2022 Wiley-VCH. (c) ReS_2 quantum dots by the two-step CVD.[40] Lateral epitaxy of ReS_2 along the inner edges fills the voids and results in the final one layer ReS_2 quantum dots embedding in one layer MoS_2 matrix. Reproduced with permission from Wang *et al.*, ACS Nano **14**, 899–906 (2020). Copyright 2020 American Chemical Society. (d) The schematic diagram of the plasma-enhanced chemical vapor deposition (PECVD) system.[41] During the CVD process, the methane plasma would be generated upstream. Reproduced with permission from Liu *et al.*, Nat. Commun. **9**, 193 (2018). Copyright 2018 Springer Nature. (e) Bright-field transmission electron microscopy (BF-TEM) overview images of $CsPbBr_3$ and $CsPbI_3$ NCs.[46] The cubic and rectangular shapes of two QDs are well shown in the figures. Reproduced with permission from Tong *et al.*, Angew. Chem., Int. Ed. **55**, 13887–13892 (2016). Copyright 2016 Wiley-VCH. (f) Scheme of depositing $CsPbX_3$ PQDs using the vapor technology.[48] During the preparation process, the precursors are sequentially deposited on the substrate in the order, and then, the QDs are formed through annealing in a nitrogen atmosphere. Reproduced with permission from Pei *et al.*, ACS Nano **16**, 2442–2451 (2022). Copyright 2022 American Chemical Society.

~3–6 nm to 45–80 nm with the increasing growth temperature.[41] Tremel's group synthesized MoS_2 and $MoSe_2$ nanoparticles with a metal-organic chemical vapor deposition (MOCVD) approach, using a gaseous precursor $Mo(CO)_6$ source of Mo. Due to the rapidly decomposing at low temperatures of the gaseous precursor, the sulfurized/selenized nanoparticles could be synthesized within a short reaction time.[42] Perovskite is currently one of the hottest optoelectronic materials. Its low-dimensional material preparation continues to attract researchers' attention. The hot-injection method remains one of the most widely utilized methods for synthesizing perovskite-QDs (PQDs), as it has demonstrated the ability to produce high-quality PQDs with a uniform size distribution.[43] Zeng's group demonstrated a room temperature-supersaturated recrystallization (RT-SR) to synthesize the $CsPbX_3$ (X = Cl, Br, I) inorganic PQDs.[44] To better control the size, morphology, and crystallization of PQDs, many other methods have been developed and applied, including the microwave-assisted synthesis, the ultrasonication synthesis method, water-triggered transformation synthesis and vapor deposition, and so on [Figs. 2(e) and 2(f)].[45–48]

B. One-dimensional materials

The process of dimensional reduction or folding of flat 2D materials can give rise to 1D structures such as nanowires (NWs), nanotubes (NTs), and nanoribbons (NRs).[49,50] The width, diameter, and atomic structure at the edges of these 1D structures play a critical role in determining the electronic and catalytic properties. 1D materials, such as zinc oxide (ZnO) NWs, III-V semiconductor NWs, organic NWs, and so on, can range in diameter from a few nanometers to hundreds of nanometers, while lengths are unrestricted and can even reach tens of hundreds of micrometers.[51,52] Due to the typically exhibiting an antenna-like shape, high aspect ratio, large surface-to-volume ratio, high carrier mobility, and a subwavelength size effect, the 1D materials usually show high photoelectric conversion efficiency and an adjustable light absorption coefficient.[53–56]

With the rapidly developing AI and artificial hardware, the 1D materials are anticipated to yield promising applications in artificial synaptic devices due to unique wide-range photoresponse, excellent electrical performance, robust stability, and, more importantly, the easy formation of large-scale arrays.[57–59] Shao *et al.* reported electrically and optically controllable carbon nanotube synaptic transistors.[60] Xie *et al.* adopted the indium gallium arsenide (InGaAs) NWs arrays to construct the organic molecule–nanowire heterojunctions with different organic semiconductors. Due to the different major carriers, tunable photoconductivity could be achieved with two different organic/inorganic heterojunctions under irradiation stimuli from the UV to the visible range, which is suitable for mimicking special functions of visual cells.[61] Moreover, Hu *et at.* regulated the synaptic plasticity of a photonic artificial synapse based on a single ZnO micro/

nanowire (MNW) synthesized by a chemical vapor deposition (CVD) method [Fig. 3(a)]. The piezo-phototronic effect was introduced with the single crystalline structure of ZnO MNW to realize the synaptic functions.[62]

Similar to 0D materials, many different methods exist to synthesize 1D materials. Presently, the difficulties in growing 1D materials include the efficient control of their size, orientation, structure, phase purity, and chemical composition.[63] In general, the top-down and bottom-up approaches are the two main strategies for synthesizing 1D materials. For the top-down approach, 1D materials are patterned by combining both lithography and etching. Among them, the typical methods include lithography, mechanical milling, chemical etching, and so on.[19,64] Zhu *et al.* utilized a top-down method to fabricate InP nanowires through inductively coupled plasma (ICP) etching. Then, the ZnO and aluminum-doped zinc oxide (AZO) p–n junction was sequentially deposited onto the NWs by the atomic layer deposition (ALD) process [Fig. 3(b)].[65] The top-down approach shows stable reproducibility and precise control during the process. However, due to approaching the physical limit of the device size, the top-down approach has to face more and more challenging issues because of the limitation in the resolution of lithography and etching techniques. Moreover, structural damage is also inevitable during the etching process, which may introduce structural defects and damage to the synthesized material. On the other hand, the bottom-up approach, which includes CVD, MOCVD, physical vapor deposition (PVD), MBE, pulsed laser deposition (PLD), metal-organic vapor epitaxy (MOVPE), template-assisted synthesis, and solution phase synthesis, shows potential in precise controlling in size, shape, and composition of the synthesized 1D material.[58,66–74] The CVD is one of the most common methods to fabricate 1D materials. Ho's group synthesized different III-V semiconductors and perovskite NWs using CVD methods.[75–79] Based on the vapor–liquid–solid (VLS) growth mechanism, the vapor-phase precursors would form a liquid eutectic alloy with catalysts, such as Au, Sn, Pd, and Ni, at the growth temperature. When the appropriate thermodynamic, kinetic, and/or supersaturation conditions are met, the crystalline wires and rods grow in a well-organized and structured manner.[19] In carbon-based 1D materials, CVD also plays a crucial role in synthesizing carbon nanotubes (CNTs) and graphene (Gr). Ahmad *et al.* synthesized single-walled carbon nanotubes (SWCNTs) based on CVD with monometallic (Fe, Co, and Ni) and bimetallic (Co-Ni and Co-Fe) catalyst particles.[80] Moreover, transition metal dichalcogenides (TMDCs), one of the most famous material systems,

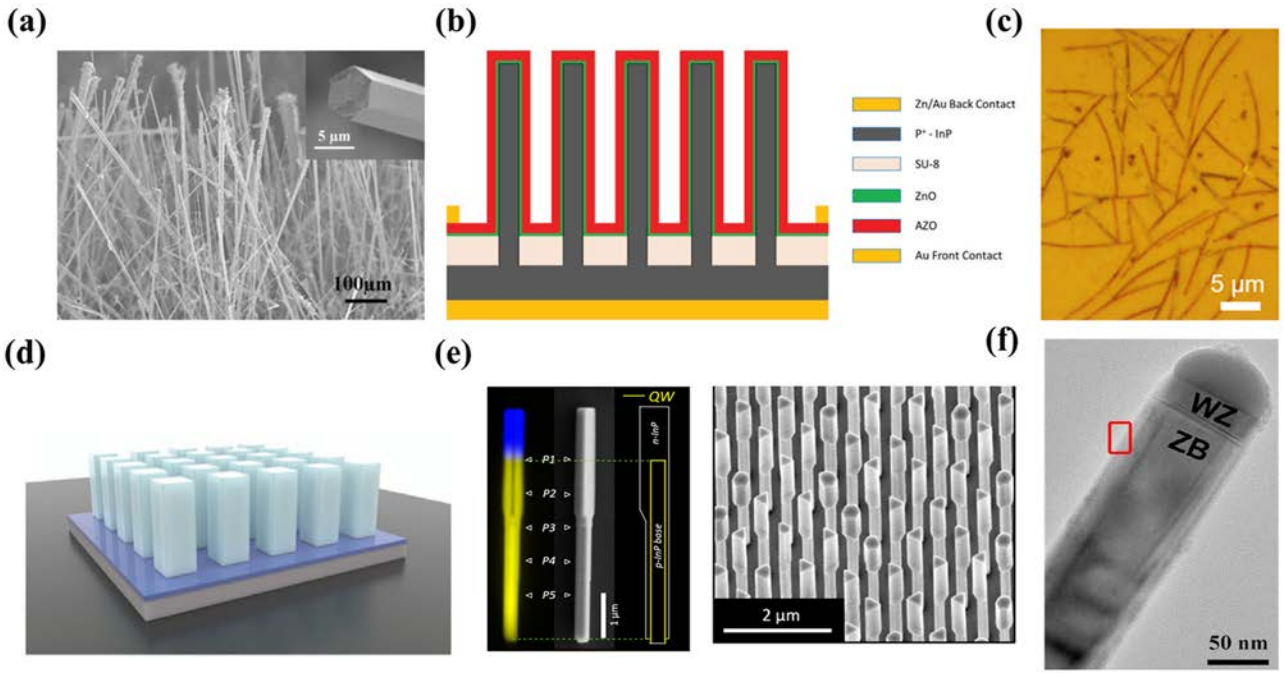

FIG. 3. (a) The SEM image of ZnO NWs; the inset SEM image is an enlarged view of NW.[62] The images demonstrate the length and diameter distribution of nanowires. Moreover, the hexagonal cross section is also shown here. Reproduced with permission from Hu *et al.*, Nano Energy **89**, 106282 (2021). Copyright 2021 Elsevier. (b) Schematic illustration of the device based on the InP NW p-n junction.[65] The device arrays consist of the Zn/Au back contact, the p-type NW core and the n-type ZnO/AZO shell (p-n junction), the Au front contact, and the SU-8 isolating layer. Reproduced with permission from Zhu *et al.*, Adv. Mater. **33**, 2105729 (2021). Copyright 2021 Wiley-VCH. (c) The microscope image of the MoS_2 nanobelts on the Si substrate. Reproduced with permission from Murthy *et al.*, ACS Appl. Mater. Interfaces **10**, 6799–6804 (2018).[81] Copyright 2018 American Chemical Society. (d) Fabrication of the Mo-based nanopillar (NP) arrays. Reproduced with permission from Maduro *et al.*, Adv. Funct. Mater. **32**, 2107880 (2022).[82] Copyright 2022 Wiley-VCH. (e) Panchromatic cathodoluminescence image of the InGaAs/InP quantum well NW (left), and its corresponding SEM image of the NWs array (right).[84] The blue and yellow regions are the panchromatic images measured with the Si charge-coupled device and the InGaAs detector, respectively, representing the InP and QW regions. Reproduced with permission from Yang *et al.*, Nano Lett. **19**, 3821–3829 (2019). Copyright 2019 American Chemical Society. (f) The TEM image of a $GaAs_{1-x}Sb_x$ NW with $x = 0.18$.[88] The main body of the nanowire consists of a ZB structure, except for the WZ structure at the tip region. Reproduced with permission from Li *et al.*, Nano Lett. **17**, 622–630 (2017). Copyright 2017 American Chemical Society.

could also be fabricated in 1D with the CVD method. As shown in Fig. 3(c), Murthy *et al.* fabricated 1D MoS_2 nanobelts on SiO_2/Si substrates using a one-step CVD process.[81] Maduro *et al.* fabricated a vertically aligned Mo-MoS_2 core/shell nanopillar (NP) array with a two-step CVD method.[82] Mo-based nanopillar arrays were used as scaffolds to synthesize the Mo/MoS_2 core/shell structure [Fig. 3(d)]. Under a sulfur-rich and ambient pressure atmosphere, the outer surface of the Mo nanopillar would be sulfurized to MoS_2 resulting in the core–shell structure with the reaction temperature of 650 °C. It is noted that MOCVD is a specific type of CVD process that uses metal-organic precursors, which are volatile compounds that contain both metal and organic components.[83] Therefore, the main difference between CVD and MOCVD is the selection of precursors. Yang *et al.* utilized the MOCVD to fabricate InGaAs/InP quantum well (QW)-NW. Trimethylindium (TMIn) and phosphine (PH_3) were used as precursors for InP. In addition, TMIn, trimethylgallium (TMGa), and arsine (AsH_3) were used as precursors for the InGaAs QW-NW [Fig. 3(e)].[84] Maliakkal *et al.* studied the catalyst composition during nanowire growth with *in situ* measurement.[85] The Au-seeded GaAs NWs were synthesized by MOCVD with TMGa and AsH_3 as precursors. Unlike CVD and MOCVD, MBE can precisely control the composition and thickness of the deposited materials at the atomic level. This characteristic allows MBE to fabricate complex, layered structures with specific electronic properties, such as multicomponent heterostructures, in which layers of different semiconductors are grown on top of each other.[86,87] Li *et al.* studied the growth of near full-composition range $GaAs_{1-x}Sb_x$ NWs by MBE method. The different component $GaAs_{1-x}Sb_x$ NWs were directly synthesized on Si(111) substrates by tuning the Sb and As fluxes [Fig. 3(f)].[88] Morral's group took full advantage of MBE to prepare the GaAs NWs on a patterned silicon substrate.[89] The substrate was degassed at 870 °C for 60 min in the growth chamber to form pinholes in the native oxide, followed by the Ga pre-deposition step for 40 min at 634 °C. Finally, the self-catalyzed growth of NWs would last 16 min at a beam equivalent pressure of 2×10^{-6} Torr.

Different from the many methods mentioned above, solution phase synthesis demonstrates the advantages of low production cost, scalability, and reduced temperature. More importantly, due to the low growth temperature, it is possible to be compatible with flexible substrates and suitable for synthesizing organic materials.[90,91] Solution-phase self-assembly is an effective approach to preparing 1D materials, especially for organic nanostructures with strong π–π stacking between organic molecules.[92] Qiu *et al.* blended poly(3-hexylthiophene) (P3HT) and amorphous polystyrene (PS) in dichloromethane (CH_2Cl_2) to self-assemble into P3HT nanofibers.[93] Ding's group fabricated ZnO NWs-based micro-structured gas sensors using a self-assembled approach. The substrates were first put in a mixing solution of $Zn(NO_3)_2$ and NaOH for pretreatment. Then, the pH value of the precursor solution, including $Zn(NO_3)_2$, was carefully adjusted at 9.3 with a proper volume of nitric acid solution. Finally, the pretreated substrate with ZnO seeds was immersed upside down in the growth solution and grown at 90 °C for 5 h.[94]

C. Two-dimensional materials

Two-dimensional materials represent a new class of nanostructured materials that offer promising features for use as emerging materials in developing extremely thin semiconductor devices in the future. The versatility of 2D materials, which includes conductors, semimetals, semiconductors with varying bandgaps, and insulators, allows for great flexibility in building van der Waals (vdW) stacks. Among the candidates for 2D materials, graphene, black phosphorus (BP), hexagonal boron nitride (h-BN), and TMDCs are particularly attractive due to their stable chemical, thermal, and complementary properties.[95]

2D semiconductors offer high photoresponsivity and a wide range of bandgap coverage, ranging from infrared (IR) to ultraviolet (UV). Moreover, the near-atomic thickness of 2D materials is characterized by covalent bonding and a surface free of dangling bonds, which provides an ideal platform for fabricating artificial visual systems and memristors.[11] Since the single graphene layer has been successfully exfoliated from bulk graphite, the other 2D materials, such as TMDCs and BN, can be adopted, like simple mechanical exfoliation to fabricate a few or even single-layer devices.[96] Huang's group took the characteristics of GO with a versatile decoration of polar oxygen-containing hydrophilic groups to construct a co-assembled perylene/graphene oxide hetero-bilayer on the solution surface [Fig. 4(a)]. The synaptic devices showed the broadband photoperception from 365 to 1550 nm and realized various neurological functions.[97] Guo *et al.* utilized the ferroelectric α-In_2Se_3/GaSe vdW heterojunction to implement the multiple functions of the biological visual neuromorphic system.[98] In order to overcome the shortcomings in response range of conventional artificial visual systems, Roy *et al.* fabricated the in-sensor artificial visual system where infrared-sensitive $PtTe_2$/Si was the gate electrode and UV-visible sensitive monolayer MoS_2 was the conduction channel. The channel conductance could be modulated by light ranging from UV-visible to infrared regimes. In addition, the necessary synaptic behaviors, including short-term plasticity (STP) and long-term plasticity (LTP), can be realized by multiple wavelengths of light [Fig. 4(b)].[99] In addition to TMDCs, 2D organic semiconductors are also widely used in artificial optoelectronic devices.[100] Hu's group utilized the solution process to prepare two-dimensional molecular crystals of 2,7-dioctyl[1]benzothieno[3,2-b][1]benzothiophene (C8-BTBT). The 2D organic film was transferred onto different pretreated substrates and the bottom-gate top-contact structure was constructed. The organic artificial visual memories exhibited multilevel nonvolatile memory functionality with long retention time due to surface trapping.[101]

It is believed that the preparation approaches of 2D materials mainly include exfoliation, epitaxial growth, CVD growth, hydrothermal growth, and self-assembly. Each preparation method has advantages, disadvantages, and the most suitable material system.[102] Mechanical exfoliation is the easiest method to obtain thin 2D materials. Due to the layered bulk single crystals with vdW contact, atomically thin flakes can be fabricated using scotch-tape exfoliation. The exfoliated thin flakes of 2D materials have clean surfaces and few defects because of the high crystallinity of bulk crystals. Therefore, mechanical exfoliation brings research convenience for constructing different heterojunctions with specific functional requirements.[103] However, the most significant limitation of mechanical exfoliation is that the size of thin flakes obtained by this method is usually tiny. It means the traditional mechanical exfoliation does not have the ability of large-area array preparation. In addition to this method, CVD is the most widely used method to synthesize 2D materials. Various materials can be synthesized via CVD, including TMDCs, h-BN, and graphene.[104] In addition, epitaxial growth is essential for preparing high-quality 2D materials during CVD. Introducing a substrate with

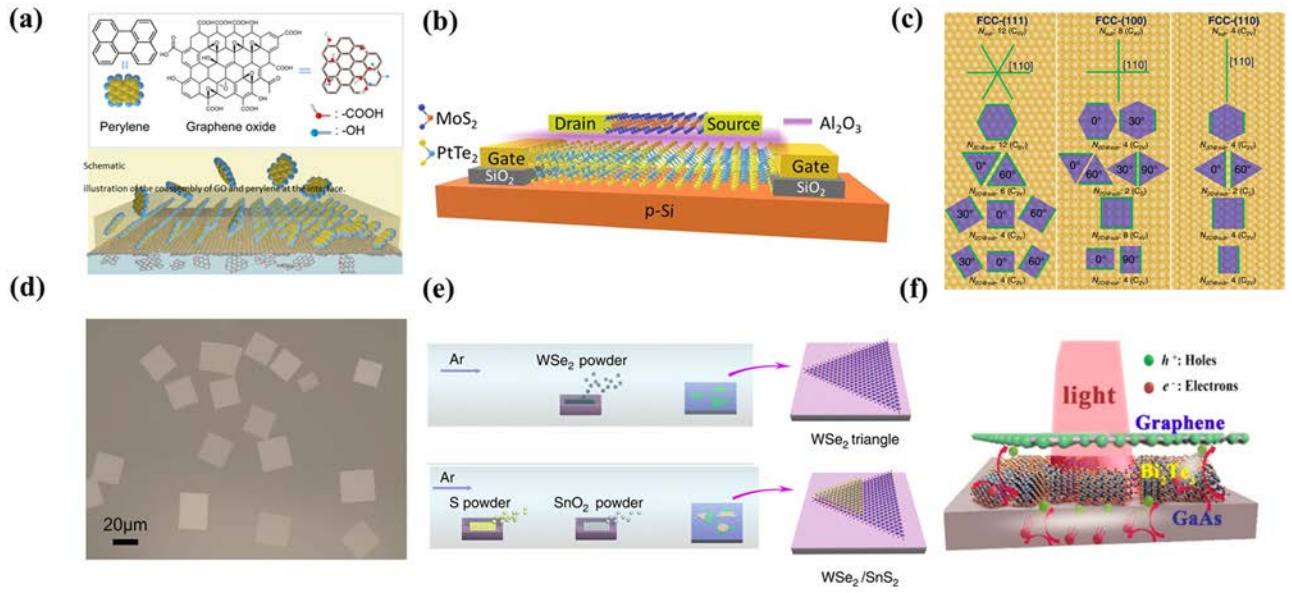

FIG. 4. (a) Schematic illustration of the co-assembly interface of two materials.[97] During the process, GO solution in methanol solvent is first dropped onto the water surface. Then, the perylene/toluene solution is dropped onto the dispersed GO sheets and started to assemble a crystalline layer at the gas–liquid interface. Reproduced with permission from Zhang *et al.*, Nat. Commun. **13**, 4996 (2022). Copyright 2022 Springer Nature. (b) Schematic diagram of the multiwavelength optoelectronic synapse.[99] In this structure, p-Si/$PtTe_2$ is used as the gate electrode and also sensitive to infrared light. The monolayer MoS_2 plays the role of the channel material and has the response to the UV−visible range. Reproduced with permission from Islam *et al.*, ACS Nano **16**, 10188–10198 (2022). Copyright 2022 American Chemical Society. (c) Alignment of single-crystalline 2D islands with various symmetries on low-index fcc and h-BN (0001) surfaces.[106] The crystallographic orientations of substrates, denoted by green lines, can be either ⟨110⟩ or ⟨11$\bar{2}$0⟩. 2D islands are represented by purple polygons. The symmetry groups of the 2D material, substrate, and the system of the 2D island on the substrate are provided. Reproduced with permission from Dong *et al.*, Nat. Commun. **11**, 5862 (2020). Copyright 2020 Springer Nature. (d) Optical image of the CVD-grown Bi_2O_2Se flakes on mica. Reproduced with permission from Wang *et al.*, Adv. Mater. **35**, 2210854 (2023).[108] Copyright 2023 Wiley-VCH. (e) Schematic illustrating the growth process of the WSe_2/SnS_2 epitaxy heterostructure.[110] The two-step growth method is applied here. The SnS_2 can be epitaxially grown on the WSe_2 by the two-step growth. Reproduced with permission from Yang *et al.*, Nat. Commun. **8**, 1906 (2017). Copyright 2017 Springer Nature. (f) Schematic illustration for rapid separation and migration of photogenerated carriers.[112] Under light illumination with a photon energy larger than the bandgap, both materials would have the photoresponse and generate the photogenerated electron–hole pairs. However, when the energy of incident light is weak, only Bi_2Te_3 can effectively create the electron–hole pairs, separated by the heterointerface of Bi_2Te_3/GaAs. The electrons would be injected into the GaAs substrate, while the holes in the Bi_2Te_3 layer would be collected by graphene, resulting in photocurrent generation. Reproduced with permission from Zhang *et al.*, ACS Nano **16**, 3, 4851–4860 (2022). Copyright 2022 American Chemical Society.

specific lattice parameters could realize substrate epitaxial growth with lattice matching between substrates and materials. In addition, van der Waals epitaxy is another type that utilizes weak intermolecular forces, specifically van der Waals interactions, to grow crystalline films on substrates. When the substrate and the material have a lattice mismatch, but the mismatch is minor enough, and the van der Waals interactions between the two materials are strong enough, the van der Waals epitaxy would occur [Fig. 4(c)].[105,106] Zhang *et al.* utilized the c-plane sapphire [(0001) α-Al_2O_3] as the substrate to epitaxially synthesize the large-area, single-crystal WSe_2 monolayer.[107] As demonstrated in Fig. 4(d), Wang *et al.* adopted mica as the substrate to grow the 2D bismuth oxychalcogenides (Bi_2O_2Se) layers.[108] The ferroelectric polarization of this 2D material exhibits tunability photoresponse and electronic characteristics. It is different to have strong interactions with the substrates. Shi *et al.* realized the MoS_2 nanoflakes van der Waals epitaxy growth on the surface of graphene. Due to atomically flat, free of dangling bonds of graphene and relatively large lattice mismatch between MoS_2 and graphene, van der Waals epitaxy could be archived to synthesize high-quality MoS_2 single-crystal flakes.[109] P-N junction as a fundamental and essential component for high-performance optoelectronics is extensively researched and prepared. To overcome the limitations of mechanical exfoliation and physical transfer, Pan's group demonstrated the van der Waals epitaxial growth of large-scale WSe_2/SnS_2 vertical bilayer p–n junctions on SiO_2/Si substrates directly, with the lateral sizes reaching up to millimeter scale [Fig. 4(e)].[110] In recent days, Duan's group also adopted van der Waals epitaxy to fabricate the vertically stacked tungsten diselenide (VSe_2)/WSe_2 heterostructures. During the process, two merged VSe_2 domains where a crack in the middle epitaxially grown on bilayer WSe_2 led to ultrashort channel lengths ranging from 6 to 100 nm without photolithography. The on-state current density of 1.72 mA μm^{-1} and on-state resistance of 0.50 kΩ μm were achieved.[111]

It is similar to other low-dimensional materials, and other methods are also applied to synthesizing 2D materials. The MBE process was used to prepare a large area and uniform bismuth telluride (Bi_2Te_3) layer on the GaAs(111)B wafer [Fig. 4(f)].[112] Moreover, the solution-phase synthesis also plays an important role in synthesizing 2D materials, including organic semiconductors, metal-organic framework (MOF), and perovskites.[113–116] The monolayer MOF film [Cu-THPP, THPP = 5,10,15,20-Tetrakis(4-hydroxyphenyl)-21H,23H-porphine] was prepared by self-assembly of Cu^{2+} ions and THPP ligands. The artificial synaptic device based on this 2D MOF film

showed synaptic plasticity under light stimuli.[114] Yan's group utilized a layer-by-layer growth method to obtain highly oriented wafer-scale 2D $Cu_3(HHTT)_2$ (HHTT: 2,3,7,8,12,13-hexahydroxytetraazanaphthotetraphene) thin films on different substrates with a layer-by-layer growth method. Owing to the broadband photo-responses from ultraviolet (UV) to mid-infrared (MIR), the optical synapse based on a $Cu_3(HHTT)_2$ thin film had a response to an extensive range of photostimulation.[117]

Overall, although mechanical exfoliation is the most widely used method for studying the special properties of individual materials or construct complex heterojunctions, it is not suitable for commercial production of 2D devices. The liquid-phase exfoliation (LPE) and MBE could fabricate large-area film, but the uniformity of the former is difficult to guarantee, and the latter requires a high vacuum environment and a specific substrate. Therefore, the CVD is still the most promising way to grow large-area, high-quality 2D film.

III. DEVICE STRUCTURE DESIGN

Until now, the exploration of transistor-based optoelectronic synapses to implement artificial intelligent systems on hardware has progressed consistently. This advancement has been achieved by introducing novel device designs and meticulous material choices.[118] Biological synapses exhibit multilevel connection strengths with analog synaptic weight states between adjacent synapses. Moreover, the synapses undergo the event-dependent switching behavior during biological information processing. This analog switching phenomenon of synaptic weight is known as synaptic plasticity, which is believed to be a critical factor in biological intelligent computing functions. Different structures and functional layers are designed and added into devices to realize the synaptic functions.

In general, the synaptic devices are designed based on the existing device structure, including two-terminal and three-terminal. Specifically, the two-terminal design is mainly a vertical structure, and the three-terminal design is based on the field-effect transistor with source/drain and gate electrodes, an insulating gate-dielectric layer, and a semiconducting channel layer. Although the working mechanism of each device depends upon the structure and active material, the functional materials with strong photoresponse are priority selected.[119]

A. Two-terminal structure

The two-terminal structure of optoelectronic artificial synapses and memristors based on low-dimensional nanomaterials would be categorized into lateral and vertical devices. Han *et al.* developed a neuromorphic device based on the ZnO/PbS hybrid heterostructure for vertical structure. The sandwich structure of the active layer (ZnO/PbS/ZnO) with top and bottom electrodes, as shown in Fig. 5(a) to construct the vertical two-terminal synaptic device. The neuromorphic weight can be modulated by both electrical and light pulses.[120] Mizuno *et al.* also fabricated optoelectronic synapses using the graphene/diamond heterojunction. The array based on the heterojunction was also realized due to the advantages of vertical two-terminal structure in the preparation process.[121] Hao's group adopted 2D bismuth

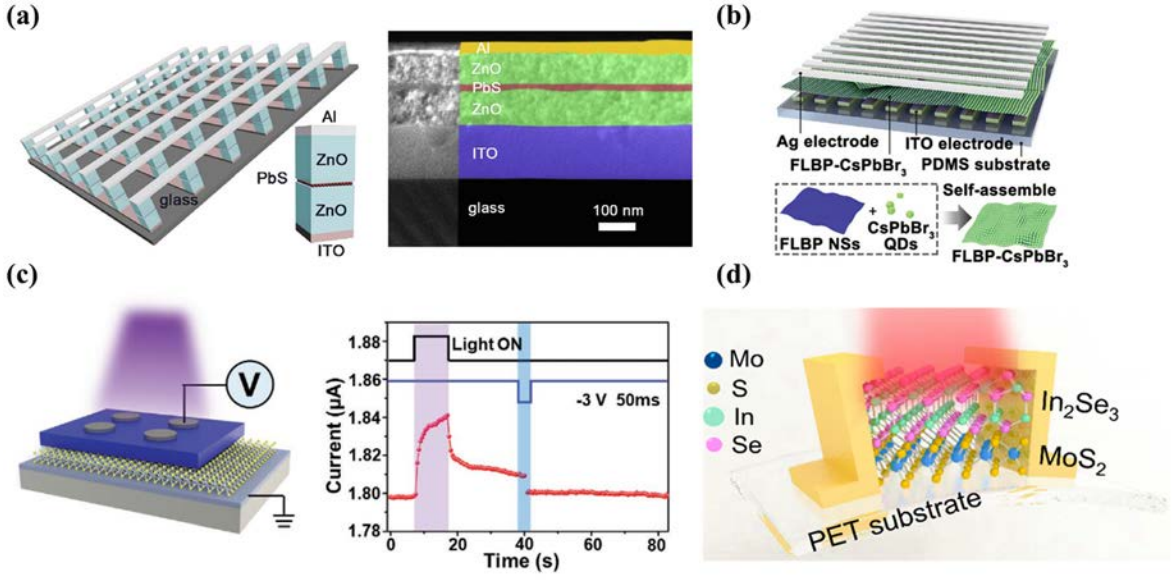

FIG. 5. (a) Illustration of the two-terminal device arrays (left), cross-sectional SEM image of the vertical device structure (right).[120] The device is fabricated on the glass substrate, with a 150-nm-thick ITO layer as the bottom bar electrode. A 30-nm-thick layer of Al is used as the top electrode. The PbS QDs and ZnO films are prepared using spin-coating at a low annealing temperature in ambient conditions. Reproduced with permission from Li *et al.*, Nano Energy **65**, 104000 (2019). Copyright 2019 Elsevier. (b) Schematic diagram of the structure of a two-terminal threshold switching memristor consisting of an Ag electrode, a few-layer black phosphorous NSs layer, $CsPbBr_3$ perovskite QDs, and an ITO electrode. The $CsPbBr_3$ QDs are densely self-assembled within the few layer black phosphorous (FLBP) NS. Reproduced with permission from Wang *et al.*, Nat. Commun. **12**, 5979 (2021).[125] Copyright 2021 Springer Nature. (c) Schematic illustration of the heterostructure-based optoelectronic synapse (left) and the light-potentiation process with a single light pulse (right).[129] The single light pulse would induce light potentiation, and a voltage pulse would realize the electrical erase. Reproduced with permission from Wang *et al.*, Adv. Funct. Mater. **31**, 2101201 (2021). Copyright 2021 Wiley-VCH. (d) Schematic of the In_2Se_3/MoS_2 synaptic device on the flexible polyethylene terephthalate (PET) substrate. Reproduced with permission from Hu *et al.*, ACS Appl. Mater. Interfaces **14**, 55839–55849 (2022).[132] Copyright 2022 American Chemical Society.

oxyiodide (BiOI) nanosheets (NSs) combined with graphene to fabricate a vertical two-terminal photonic synapse. The only Ag/BiOI/Pt device also demonstrated the potential in high-performance memristors.[122] Perovskite is one of the hottest materials in the photoelectric application field. Due to their superior electronic and optoelectronic properties, the perovskite materials, alone or in combination with other materials, are also ideal for optoelectronic artificial synapses and optoelectronic memristors.[123,124] The optoelectronic artificial synapses are designed to mimic the biological visual function, eventually surpassing it. At present, the vehicle's autopilot has made significant progress with the development of AI. To realize higher levels of autonomous driving, even driverless, the detection, and processing of visual signals becomes particularly important. The lobule giant movement detector (LGMD) is a type of neuron that is specialized for detecting movement in the visual field, particularly for collision avoidance [Fig. 5(b)]. Ag/few-layer black phosphorous nanosheets $CsPbBr_3$ perovskite quantum dots heterostructure/indium tin oxide (ITO) vertical structure was fabricated to realize artificial LGMD visual neuron. Due to the optoelectronic coupling and charge transfer of the heterojunction, the threshold switching performance can be controlled by the optical input.[125] Moreover, the bulk heterojunction can also be a switching medium in the vertical two-terminal structure. The mixed-dimensional formamidinium bismuth iodides with 2D $FABi_3I_{10}$ and 0D $FA_3Bi_2I_9$ (FA = formamidinium) were used as active layers to prepare vertical artificial synapses with low-energy consumption.[126] The perovskite and TMDCs have also been reported to be utilized in two-terminal structures.[127] The $MoSe_2/Bi_2Se_3$ hybrid nanosheets film was fabricated by the solution process and played the internal active layer of a vertical two-terminal artificial synapse. The near-infrared (NIR) irradiation acted as a modulatory terminal to change the synaptic plasticity of the device because of the NIR annihilation effect of conductive filaments (CFs).[128] Furthermore, Wang *et al.* achieved an artificial optoelectronic synapse based on $Al/TiN_xO_{2-x}/MoS_2/ITO$. Various neural functions have been successfully realized under the separate and coordinated regulation of light and electrical stimuli [Fig. 5(c)].[129] Kim *et al.* combined more materials, including ferroelectric materials and ion gates, to build more complex vertical structures. Introducing the InP QDs induced the photoresponse behavior of artificial visual receptors via the photogating effect.[130]

As mentioned above, the planar two-terminal structure is also widely used in addition to vertical devices. This structure is similar to photodetectors with two terminals, where source and drain electrodes are deposited on the active layer on the same plane. Pradhan *et al.* reported a photonic synapse using a graphene/perovskite quantum dots superstructure. Different from the traditional fabrication process of heterojunctions, the perovskite QDs were directly synthesized on a graphene lattice.[131] Furthermore, a planar two-terminal NIR synaptic device based on the In_2Se_3/MoS_2 vdW heterojunction was reported [Fig. 5(d)]. The devices not only showed the basic synaptic behaviors but also exhibited functions of image sensing and storage under NIR light.[132]

B. In-plane layout of the three-terminal structure

The three-terminal devices have an additional gate terminal compared with the two-terminal devices. By applying a voltage to the gate, the created electric field controls the flow of current between the source and the drain.[133] The main structure of the three-terminal device originated from the metal-oxide-semiconductor FET (MOSFET). The specific device structure can be distinguished according to the position of the gate. The in-plane layout of a three-terminal structure is one type of electrode design where the source, drain, and gate electrodes are on the same plane. In this structure, the choice and preparation of the dielectric layer is critical. The liquid ion electrolyte gate was introduced to the devices, where the electrolyte was dropped onto the gap between the channel and gate electrodes.[134] Jiang *et al.* used drop-coating poly(vinyl alcohol) (PVA) electrolytes to modulate the channel of MoS_2 [Fig. 6(a)].[135,136] Although the devices based on the liquid ion electrolyte gate can realize to simulate a series of neuromorphic behaviors, the flowing electrolytes are the most significant limitation to integrating devices into a circuit. Therefore, the solid ion electrolyte fabricated by immobilizing ionic liquids into polymers demonstrated potential in artificial synaptic devices. This electrolyte in solid-state ion electrolyte can form an electrolytic double layer (EDL), which contains a gating effect and has low-voltage operation characteristics. Sun *et al.* modulated the synaptic weight of the long alkyl chains-modified GO nanosheets/indium–gallium–zinc oxide (IGZO) conductive channel. An ion gel consisting of poly(vinylidene difluoride-co-hexafluoropropylene) [P(VDF-HFP)] and 1-ethyl-3-methylimidazolium bis(trifluoromethylsulfonyl)imide [(EMIM)(TFSI)] was utilized as the plane gate [Fig. 6(b)]. The EDL effect of ion gel combined with the charge-trapping effect of alkylated GO to realize various neurological functions under electrical and light stimuli.[137] Then, Cheng *et al.* also adopted the ion gate with the same composition to fabricate a neuromorphic-photoelectric device based on the $CsPbBr_3$ QDs/MoS_2 heterojunction [Fig. 6(c)].[138] However, limited by the preparation method, especially on the dielectric layer, there is still a challenge to realize large-scale integration. In order to meet the needs, the solid ion gate (lithium silicate) fabricated by radio frequency (RF) magnetron sputtering was introduced into in-plane three-terminal synaptic devices.[139]

C. Vertical layout of the three-terminal structure

This device structure is the same as the MOSFET, which can be divided into four types according to the position of each functional layer. The two most commonly used structures are top gate/top contact and bottom gate/top contact. Both designs have their advantages and focus. The top gate structure can design the dielectric layers more efficiently and diversely. Different materials and structures can be introduced to prepare dielectric layers to achieve special functions. The $TiN/Hf_{0.2}Zr_{0.8}O_2$ anti-ferroelectric film/TiN as a dielectric layer was integrated into one top gate device to realize the leaky integrate-and-fire (LIF) neuron function [Fig. 7(a)].[140] Lee *et al.* designed a stack gate dielectric of $Al_2O_3/HfO_2/Al_2O_3$ as the charge storage layer [Fig. 7(b)]. The top gate and top dielectric layer not only achieved the trapping of charges but also effectively protected the black phosphorus channel from the air atmosphere.[141] Therefore, the top gate has the advantages of diverse gate dielectric and protection of channel material. Moreover, the device must be fabricated on the growth substrate for some low-dimensional materials that are not easy to transfer. The top gate becomes a necessary choice. However, the top contact structure also has shortcomings, especially for the optoelectronic artificial synapses and optoelectronic memristors. The top electrode and dielectric layer would affect the light absorption efficiency of the channel material. In addition to that, more processing is done on the low-dimensional

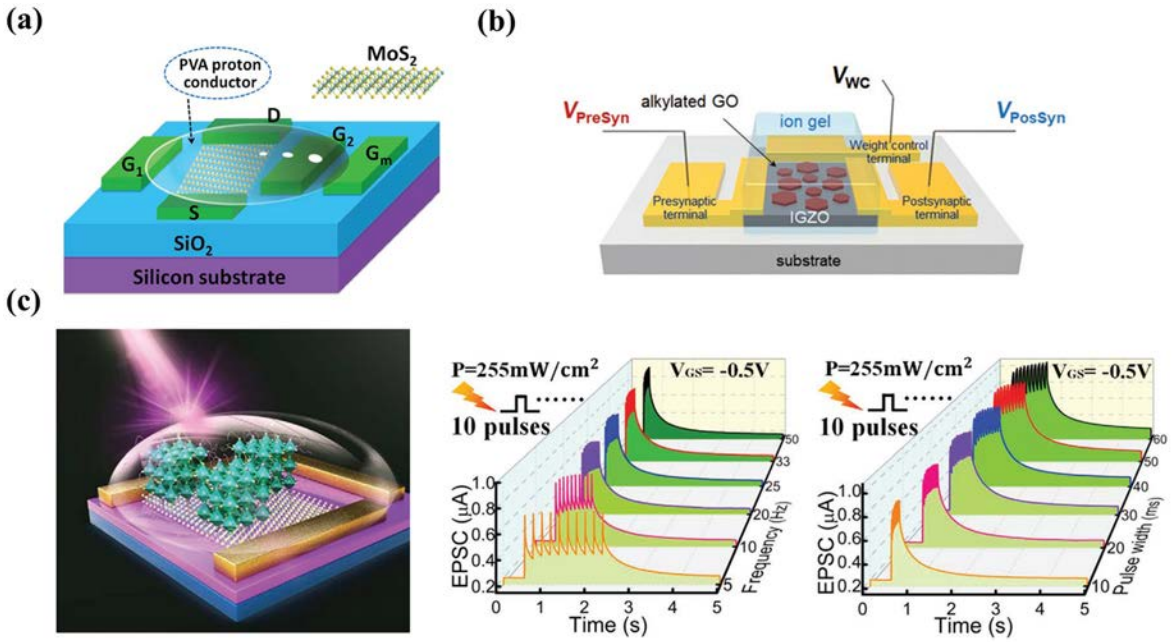

FIG. 6. (a) Schematic diagram of a multiple-gate MoS_2 neuromorphic transistor.[135] A coplanar lateral gate based on a PVA proton conductor is coupled with a 2D layered MoS_2 channel. Reproduced with permission from Jiang *et al.*, Small **13**, 1700933 (2017). Copyright 2017 Wiley-VCH. (b) Schematic illustration of the floating-gate synaptic device.[137] The ion gate is applied to modulate the performance of the heterojunction of the IGZO/alkylated GO. Reproduced with permission from Sun *et al.*, Adv. Funct. Mater. **28**, 1804397 (2018). Copyright 2018 Wiley-VCH. (c) 3D schematic structure of the device (left) and excitatory post-synaptic currents (EPSCs), short-term memory (STM), and long-term memory (LTM) triggered by the light spike (right).[138] Here, the ion gate is adopted to control the $CsPbBr_3$-QDs/2D-MoS_2 heterojunction channel. The light pulses with different frequencies and widths can induce a stronger current response and a longer relaxation time. Reproduced with permission from Chen *et al.*, Small **16**, 2005217 (2020). Copyright 2020 Wiley-VCH.

channel materials, which may introduce some defects and even damage the materials. On the contrary, the bottom gate structure can do more designs on the channel material.[142,143] At the same time, a larger photosensitive area would also be obtained. Pan's group reported an artificial photonic synapse based on the BP/CdS van der Waals heterojunction. The device was fabricated on the Si/SiO_2 substrate, and the CdS and BP were employed as the photosensitive layer and channel layer, respectively.[144] Wang *et al.* adopted Si/SiO_2 substrate to fabricate the synaptic device based on the $MoS_2/MoS_{2-x}O_\delta$ grain boundaries. Owing to the bottom gate/top contact structure, lateral $MoS_2/MoS_{2-x}O_\delta$ junctions for synaptic devices would be made using lithography-free direct-laser-writing technology on the SiO_2 dielectric.[145] Recently, more complex functional layer designs are gradually introduced into the device structure. A vertical heterojunction is reported based on a bottom gate/top contact three-terminal structure. Two graphene sheets as the upper and lower layers of the "sandwich" were connected to the source and drain electrodes, respectively. The PbS QDs serve as the NIR photoresponse layer, and the whole device was fabricated on the Si/SiO_2 [Fig. 7(c)]. Due to the tunable Fermi level in the graphene/PbS QDs heterojunction by the gate voltage (V_G), the potentiation/inhibition of photoresponse was realized under different gate voltages.[146] Liu *et al.* not only did the work in channel materials but also in the dielectric layer. The ZnO, mixed-dimensional 2D/3D $FaPbI_3$, and metal-oxide InO_x served as passivation, optical perception, and semiconductor layers, respectively. The metal-oxide $LiAlO_x$ electrolyte was utilized as the dielectric layer. Because of the complex design of the functional layers, the optoelectronic synaptic devices successfully mimicked neural responses to photoelectric stimuli.[147] In addition to traditional preparation methods, inkjet printing is a feasible way to fabricate the synaptic devices layer by layer. Recently, a fully printed optoelectronic synaptic transistor based on the InP/ZnSe core/shell QDs/SnO_2 heterojunction was reported [Fig. 7(d)]. The whole device was fabricated by inkjet-printing method, including the three electrodes, dielectric layer, and channel materials, which showed the potential in large-area integration.[148]

IV. WORKING MECHANISMS OF NEUROMORPHIC AND OPTOELECTRONIC STORAGE DEVICES

At present, numerous low-dimensional materials show various inherent benefits regarding their structural, electrical, and phase-controllable characteristics. One of the main advantages is the atomic-scale ultrathin structure. This property is beneficial for developing neuromorphic devices and memristors, which can benefit from excellent reliability and reversibility, fast switching, low-power consumption, and high-density device integration. Therefore, it is imperative and crucial to have a thorough understanding of the working mechanisms for device design and performance optimization. Currently, multiple prevailing mechanisms have been proposed, including the charge trapping/de-trapping process, the band structure, the floating gate, the ferroelectric polarization, the gas adsorption/desorption and oxygen vacancy, metal conducting filament, and phase change. In particular, the vdW contact offers the base for high-performance

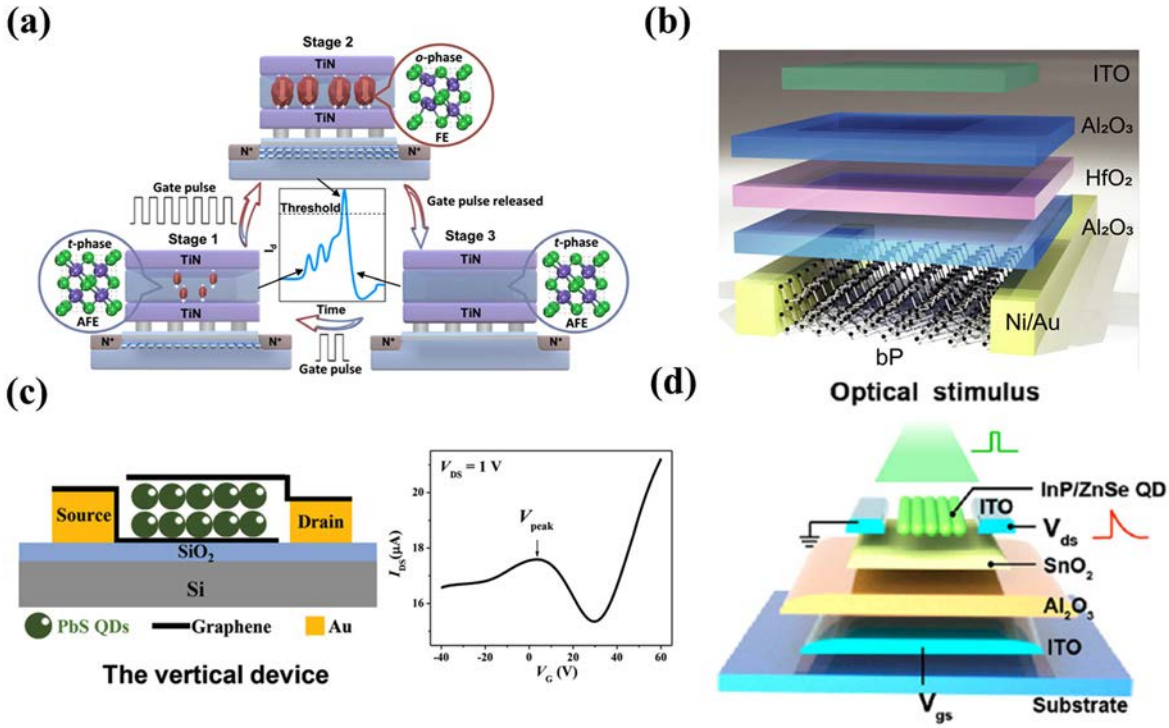

FIG. 7. (a) Integrate-and-fire dynamics of an AFeFET neuron with different working stages.[140] During stage 1, the electric field-induced ferroelectric domain nucleates, causing the accumulation of electrons in the channel. As the gate pulse is further applied in stage 2, the domains continue to grow and expand, leading to an increased accumulation of electrons in the AFeFET channel. In stage 3, when the gate pulse electric field is removed, the electric field-induced ferroelectric domains transform back into antiferroelectric domains. This results in the AFeFET channel switching off. Reproduced with permission from Cao *et al.*, Nat. Commun. **13**, 7018 (2022). Copyright 2022 Springer Nature. (b) Layer-by-layer structure of the device.[141] The main functional layers of the device consist of a few-layer BP flake as the channel, a stack of $Al_2O_3/HfO_2/Al_2O_3$ as the gate dielectric, and a charge storage layer. Reproduced with permission from Lee *et al.*, Nat. Commun. **13**, 1485 (2022). Copyright 2022 Springer Nature. (c) Cross-sectional view of the vertical device (left) and transfer characteristics of the vertical device (right). The device exhibits a typical ambipolar transfer curve of a FET with graphene as the conductive layer. Reproduced with permission from Zhang *et al.*, Adv. Mater. **34**, 2205679 (2022).[146] Copyright 2022 Wiley-VCH. (d) Schematic diagram of the biological synapse based on the QDs heterojunction.[148] All functional layers are fabricated by the printing process. Reproduced with permission from Liang *et al.*, ACS Nano **16**, 8651–8661 (2022). Copyright 2022 American Chemical Society.

neuromorphic and optoelectronic storage devices because of the clean interface without dangling bonds. The carriers can transfer between different interfaces more effectively, which is the key to fabricate ultrafast and ultra-low-power consumption devices.

A. Trap states

Charge trapping and de-trapping extensively occur when the device works because of the surface defect states, interface defect states, and bulk defects.[149] Furthermore, due to the stable and reversible physical operation, the charge trapping and de-trapping processes have been widely used in designing optoelectronic artificial synapses and memristors.[150–153] Combined with the advantages of low-dimensional materials, such as large surface-to-volume ratio, ultra-thin structure, clean interface without dangling bonds, and high carrier mobility, the synaptic weight of the channel could be effectively modulated.

In general, charge trapping and de-trapping mechanisms are mainly divided into several categories. The first type uses the insulating layer interface, where Al_2O_3 and SiO_2 are the most commonly used materials. Li *et al.* adopted the Al_2O_3 as the dielectric layer to trap the photogenerated holes in the MoS_2 layer when $V_G < 0$. The electrons would neutralize the trapped holes and realize the de-trapping process when $V_G > 0$.[154] Miao's group fabricated the WSe_2/h-BN/Al_2O_3 heterostructure device to realize the positive and negative photoconductivity with different V_G. When the negative voltage was applied to the gate, the trapped electrons would migrate upward in the BN/WSe_2 interface. Therefore, the left positively charged defects localized in the interface of h-BN and Al_2O_3 were not recombined during light illumination, which caused the back-gate electric field shielding and realized the negative photoconduction of the WSe_2 channel.[155] In addition to that, the SiO_2 is also served as the dielectric and trapping layer.[156,157] Lee *et al.* constructed artificial synapses based on indium selenide (InSe). The charge trapping and de-trapping processes would occur at the interface between InSe and SiO_2 with different gate voltages [Fig. 8(a)].[158] In addition to the inorganic oxide dielectric materials, the trapping and de-trapping processes can also be realized by other methods, such as functional layer design and the introduction of hydrophilic groups. For the following type of using trapping states, Hu *et al.* introduced hydroxyl groups into the MoS_2, which exhibited a strong capability of charge trapping.[159] Pan's group introduced Au nanoparticles on MoS_2 for optoelectronic artificial synapses. The photogenerated electrodes would be trapped near the doped Au atoms, which caused the

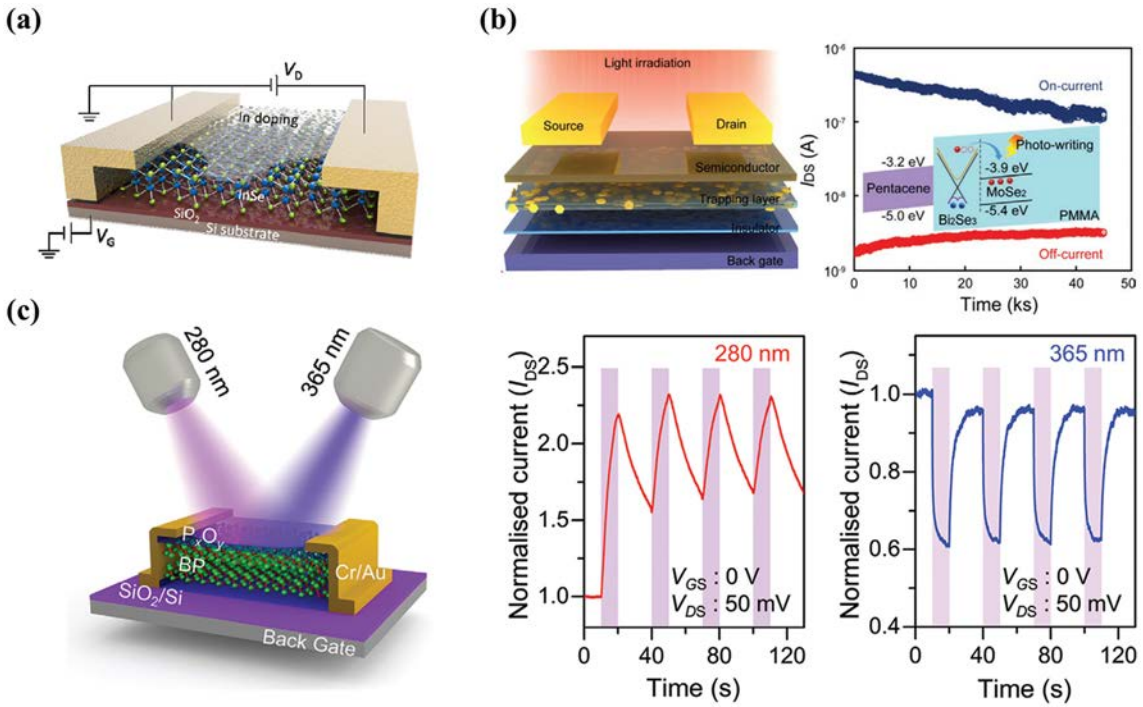

FIG. 8. (a) Schematic illustration of the in-doping device, consisting of Au/In electrodes as source and drain, InSe channel, and SiO_2 substrate. Reproduced with permission from Lee *et al.*, Nano Energy **77**, 105258 (2020).[158] Copyright 2020 Elsevier. (b) Device structure of the $MoSe_2/Bi_2Se_3$-based transistor fabricated on the SiO_2/Si substrate (left) and retention test (right). Inset shows a schematic diagram of the energy level in the optical programmed state. Reproduced with permission from Wang *et al.*, Adv. Electron. Mater. **6**, 1900765 (2020).[161] Copyright 2020 Wiley-VCH. (c) Schematic diagram of the device fabricated based on BP (left). Positive and negative photoconductivity of a BP device under 280 and 365 nm illumination pulses (right).[162] The normalized photocurrent is induced by the sequential 10 s light pulses. Reproduced with permission from Ahmed *et al.*, Adv. Mater. **33**, 2004207 (2021). Copyright 2021 Wiley-VCH.

photogate effect and made the optoelectronic synaptic behaviors achieved.[160] Moreover, a whole heterojunction structure of $MoSe_2/Bi_2Se_3$/poly(methyl methacrylate) (PMMA) was also adopted to serve as the trap layer [Fig. 8(b)]. In detail, Bi_2Se_3 as a topological insulator let the photogenerated electrons flow through and trap by the $MoSe_2$. The strong photogating effect effectively maintained the density of the holes in the P-type pentacene channel for synaptic response.[161] In addition to the well-designed functional layers mentioned above, the trap state can also be realized by using the changes in the material in the atmospheric environment, such as oxidation and gas adsorption. Black phosphorus (BP) is one of the typical 2D materials with strong in-plane optical and electronic anisotropy. However, its fragile air stability limits the development of devices based on BP. Every coin has two sides; the native phosphorus oxide (PO_x) layers formed on the BP surface could effectively trap the photogenerated carriers and realize the tunable photoconductivity, which can mimic the function of human visual systems [Fig. 8(c)].[162,163]

B. Band engineering

The different types of heterojunctions are widely studied in optoelectronic devices for optimizing the photoresponse performance. Based on the elaborated design of the interfacial band alignment, the photogenerated electron–hole pairs would be separated effectively and be trapped in selected materials, which can suppress the recombination of the carriers.[164,165] Therefore, the extended retention of carriers in the channel delays the decay of the photocurrent, which is the basement to achieve artificial optoelectronic synaptic characteristics. So far, PN junction, Schottky junction, quantum well, superlattice, and so on are reported to be used in optoelectronic synaptic devices and memristors.[166–170] Here, different synaptic devices can be classified according to structure. For the first type, planar heterojunction is adopted, and source/drain electrodes are deposited on the same materials. Xie *et al.* introduced porous metal-organic framework (MOF)/ReS_2 Type I heterojunction to realize polarization-sensitive visual adaptation emulation. The different V_G would affect the heterojunction's band structure, leading to different photocurrents [Fig. 9(a)].[171] Kuang *et al.* constructed the heterojunction based on perovskite QDs and poly(3,6-di(2-thien-5-yl)-2,5-di(2-octyldodecyl)-pyrrolo[3,4-c] pyrrole-1,4-dione) thieno[3,2-b]thiophene (PDPP-TT) organic film on the Si/SiO_2 substrate. The type-I heterojunction completed the carrier injection and trapping process.[28] Similarly, Liu's group fabricated poly(n-alkyl pyrrolepyrrole dithiophene) (PDPP-DTT) films as the semiconductor channels and covered with the PbS QDs film [Fig. 9(b)]. The QDs played as the absorbing layer of short-wave infrared layer and realized the separation and trapping of photogenerated carriers.[172] As mentioned above, the photoelectric performance of materials is an important consideration in material selection. The perovskites and organic photovoltaics field provide many optoelectronic materials with excellent properties. In addition to the QDs discussed above,

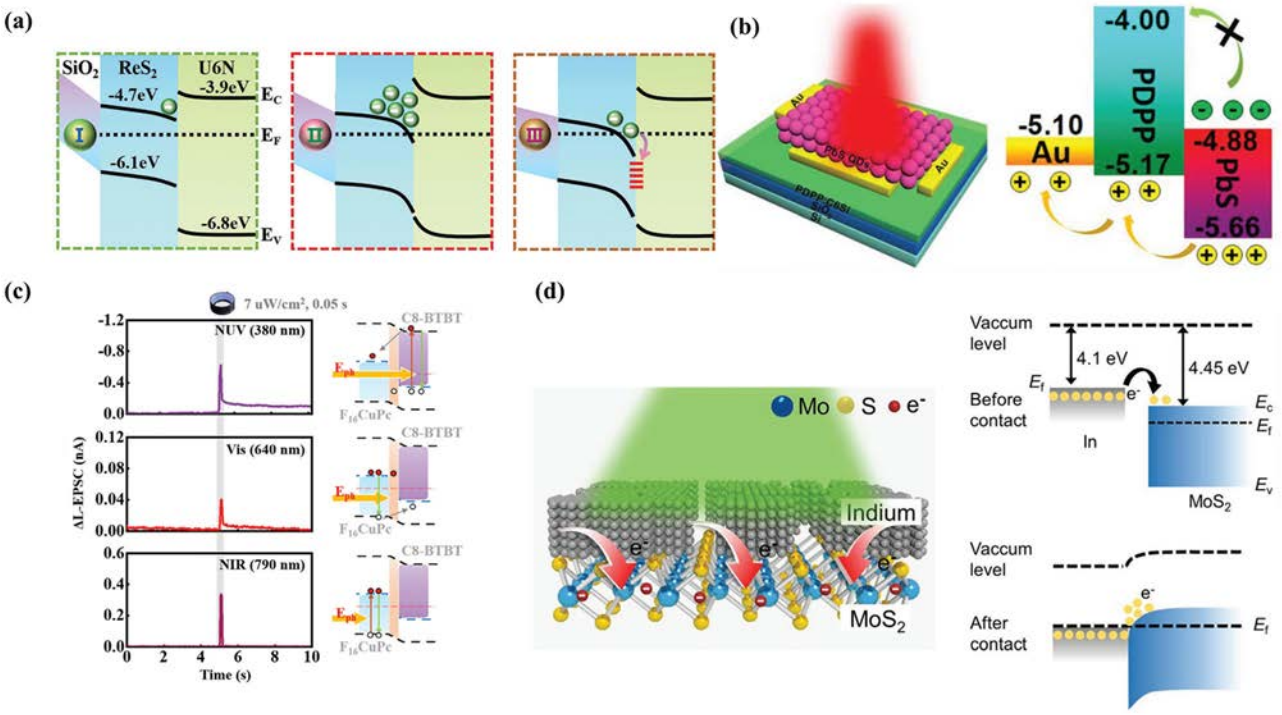

FIG. 9. (a) Schematic energy-band diagrams of the ReS_2/U_6N heterojunction, which consists of three different processes (original state, activated state, and adaptive process). Reproduced with permission from Xie *et al.*, Adv. Mater. **35**, 2212118 (2023).[171] Copyright 2023 Wiley-VCH. (b) Structure of the organic/QDs phototransistor (left). Schematic energy-band diagram of the synaptic transistor (right).[172] The photogenerated holes in PbS can be separated at the interface and transported into PDPP. Reproduced with permission from Huang *et al.*, Adv. Funct. Mater. **33**, 2208836 (2023). Copyright 2023 Wiley-VCH. (c) The EPSCs triggered by different wavelengths of light pulses of 380, 640, and 790 nm (left). Energy band diagrams under three types of illuminations are on the right. Reproduced with permission from Ni *et al.*, Adv. Sci. **9**, 2102036 (2022).[177] Copyright 2022 Wiley-VCH. (d) Schematic illustration of the surface charge doping synaptic device (left). Schematic diagram of energy band structure before and after the doping process (right).[181] The difference in Femi level causes the electrons in the In layer to flow into the MoS_2 when they are in contact with each other. Due to the electric field at the interface, the energy band would also bend in response. Reproduced with permission from Hu *et al.*, Adv. Mater. **33**, 2104960 (2021). Copyright 2021 Wiley-VCH.

the 2D perovskite/organic heterojunction (PEA_2SnI_4/Y_6) was also fabricated by the solution process. Due to the wide absorption range, the synaptic device had a large photoresponse from visible to near-infrared.[173] Wang *et al.* distributed the Si QDs on the MoS_2 channel layer and formed the type II heterojunction. In this structure, the photogenerated electrons in Si QDs would transfer to MoS_2 and reserve the photogenerated holes in Si QDs, leading to the strong photogating effect.[174] Beyond that, the bulk heterojunction is also an essential means to achieve energy band engineering. The organic P3HT mixed the perovskite QDs and Si NCs, respectively, to fabricate optoelectronic synapses.[175,176] Combined with the low-dimensional materials, the bulk heterojunction fully uses the advantages of high surface-to-volume ratio and efficiently separates and confines specific carriers. Xu's group mixed the PMMA/C8-BTBT/copper hexadecafluorophthalocyanine ($F_{16}CuPc$) as the dual-channel photoresponse layer to mimic the human visual behaviors [Fig. 9(c)].[177]

Then, the structure where the source/drain electrodes are deposited on different materials is also widely used.[178] Due to the P-N junction being the primary goal of building this structure, the source/drain electrodes would contact P-type or N-type materials, respectively. A double-layer design of two-layer C8-BTBT and $F_{16}CuPc$ was introduced to emulate human retina perception.[179] The source and drain electrodes were prepared on P-type and N-type materials, respectively. In this structure, the V_G is often adopted to control the heterojunction's energy band structure and affect carriers' transport path. Compared with low-dimensional organic semiconductor materials, the 2D TMDCs have the advantages of a more straightforward preparation process, stability, and compatibility with photolithography. Wang *et al.* prepared an optoelectronic synaptic device based on the $MoTe_2/\alpha$-In_2Se_3 P-N junction. Due to the ferroelectric characteristic of the α-In_2Se_3, the V_G would induce the nonvolatile rectification behavior and photovoltaic effect.[180] In addition to the traditional methods to realize band engineering, doping and flexoelectric are feasible ways to modulate the band structure of the channel materials. Hu *et al.* used indium (In) as the electron injection layer to cover the MoS_2 channel to fabricate an optical artificial synapse [Fig. 9(d)]. The surface charge doping induced by In layer would inject electrons into the MoS_2 because of the difference of Fermi level, which effectively increased the carrier concentration of channel and achieved the power consumption down to 68.9 aJ per spike.[181] Interestingly, the N-P homojunction was prepared by bipolar WSe_2. The asymmetrical stacking of WSe_2 at the drain and source terminals with multilayered graphene flakes made N-P homojunction and P^+-P homojunction under

specific gate voltages.[182] Moreover, Wang *et al.* introduced the flexo-photoelectronic effect into artificial synaptic devices. When channel materials were bent, the flexoelectric polarization would contribute to back-to-back built-in electric fields and trap the photogenerated carriers in the bend area, resulting in photoconductance relaxation. Several neuromorphic behaviors, like short/long-term memory (S/LTM) and excitatory post-synaptic current (EPSC), were mimicked by the InSe synaptic devices based on the flexo-photoelectronic effect.[183] Finally, not only for three-terminal devices, the band engineering also can be applied to two-terminal optoelectronic synaptic devices. The P-N junction-based $CuAlO_2$/ZnO core–shell nanorod structure was adopted to fabricate the device with the construction of ITO/$CuAlO_2$/ZnO/ITO.[184]

C. Floating gate

To date, the floating gate structure original from conventional flash memory is widely used in optoelectronic artificial synapses and optoelectronic memristors with the advantages of stable conductance switching and long-term retention characteristics.[185–187] In general, the floating gate structure can be fabricated by stacking different functional layers vertically, including the floating gate, blocking layer, ultra-thin tunnel layers, and semiconductor layer.[188] Among them, low-dimensional materials can play different roles in floating gate structures. The highly conductive graphene is famous as the floating gate, which can store charge carriers for device applications.[189] Han *et al.* utilized graphene to restrict the photogenerated carriers from perovskite QDs [Fig. 10(a)]. In the synaptic device, ultra-thin hexagonal boron nitride served as the tunnel layer to block the recombination of holes, and electrons.[27] Sun *et al.* fabricated the floating gate optoelectronic device based on a classical device structure with the multilayer graphene/h-BN/MoS_2 vertical heterostructure [Fig. 10(b)]. The device integrated the functions of nonvolatile memory and neuromorphic optoelectronic applications under the synergistic modulation of electrical and optical stimulation.[190] In recent years, owing to the various material compositions, including 2D metal carbide (carbonitride or nitrogen nitride), MXene, a new type of 2D material, has been proposed as a floating gate for artificial synaptic devices.[191] Zhao *et al.* introduced solution-processed oxidized MXenes as the floating gate to realize the modulation of synaptic weight based on electric and light pulses [Fig. 10(c)].[192] In addition to classical inorganic 2D materials, 2D imine polymer was introduced into the photonic synaptic devices that served as the floating gate. Due to the excellent absorption property, the 2D imine polymer could effectively trap the photogenerated carriers in the pentacene channel.[193]

There are lots of advantages for 2D materials in floating gate structures. However, it is also a considerable shortcoming that it cannot be prepared in a large area with a simple process. The QDs usually dispersed in solution could be fabricated in large-area with the solution process. Park *et al.* used carbon nitride (C_3N_4) nanodots to prepare a UV-responsive floating-gate layer [Fig. 10(d)].[194] Meng *et al.*

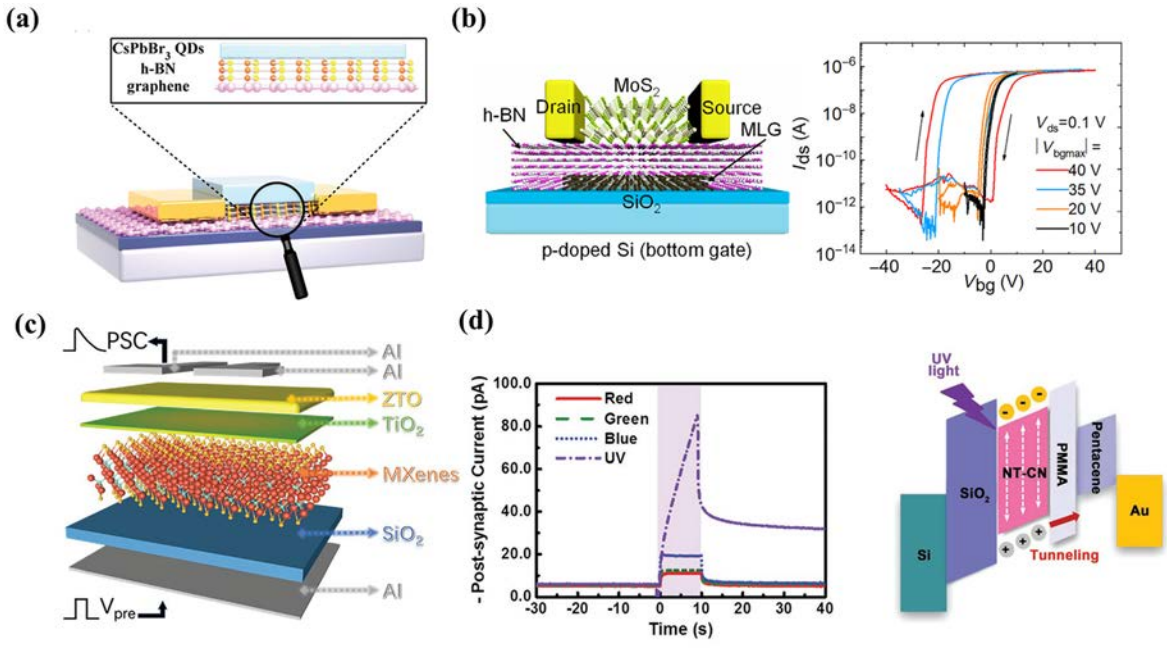

FIG. 10. (a) Schematic of the device structure based on the QDs/h-BN/Gr. Reproduced with permission from Han *et al.*, Adv. Funct. Mater. **32**, 2113053 (2022).[27] Copyright 2022 Wiley-VCH. (b) Schematic diagram of the optoelectronic synaptic floating-gate device (left). Transfer characteristic curves of the device with different sweeping ranges (right).[190] The memory window of the device would increase with the large V_G sweeping range because the larger V_G would induce more trapping carriers. Reproduced with permission from Sun *et al.*, InfoMat **4**, e12317 (2022). Copyright 2022 Wiley-VCH. (c) The structural diagram of the device.[192] In this structure, the MXenes serve as the floating gate to trap the carriers. Reproduced with permission from Zhao *et al.*, Adv. Funct. Mater. **31**, 2106000 (2021). Copyright 2021 Wiley-VCH. (d) EPSCs with different light irradiation (left). Operating principle of the heterojunction under UV illumination (right).[194] The UV light (with a shorter wavelength) would induce the tunneling effect between NT-CN and PMMA. The photogenerated holes would tunnel through the PMMA layer and cause a higher current in the pentacene channel. Reproduced with permission from Park *et al.*, Adv. Mater. **32**, 1906899 (2020). Copyright 2020 Wiley-VCH.

fabricated the Al_2O_3/BP QDs/Al_2O_3 for the optoelectronic in-memory computing device. With the help of the Al_2O_3 block layer, the device with BP QDs floating gate could realize multi-state storage.[195] Moreover, the perovskite QDs are also widely used as the floating gate. Wang *et al.* adopted $CsPbBr_3$ QDs to trap the carriers in organic semiconductor channels. The photonic synapses could realize the neuromorphic functions in the visible range due to the narrow exciton binding energy and broad range absorption properties.[196]

D. Ferroelectric polarization

Owing to the advantages of ferroelectric materials, including compatibility with different substrates, cost-effectiveness, fatigue-free remnant polarization, and controllable polarization intensity, the ferroelectric materials can control carriers' accumulation, depletion, and retention in the semiconducting channel by polarization switching.[197] The spontaneous electrical polarization capability and multiple domains of ferroelectric materials can provide nonvolatile analog memory functions. When the electronic bias is applied to the ferroelectric materials, a portion of the randomly oriented ferroelectric region begins to align in the direction of the external electric field. Moreover, this polarization does not disappear as quickly as the voltage is withdrawn. Hence, significant efforts have been made to explore artificial synaptic devices and memristors with ferroelectric materials. Overall, two ways exist to prepare optoelectronic artificial synapses and optoelectronic memristors based on ferroelectric materials. One is to use low-dimensional materials as channels and introduce ferroelectric materials as insulating layers. Another way is to utilize the ferroelectric low-dimensional materials directly as channels. Polymeric and inorganic ferroelectric materials such as $Pb(Zr,Ti)O_3$ (PZT), zirconium-doped hafnia (HZO), and poly(vinylidene fluoride) (PVDF) are widely used in synaptic devices. Alexe's group utilized PZT film to modulate part of the WS_2 channel with light and electric pulses.[198] Jiang *et al.* applied a similar strategy using different ferroelectric materials, P(VDF-TrFE). As shown in Fig. 11(a), part of the MoS_2 in the channel was placed on the P(VDF-TrFE) film, and the other part is only in contact with SiO_2 dielectric layer.[199] Moreover, the $BaTiO_3$-based ferroelectric film (BTO) was introduced to modulate the synaptic weight of a monolayer MoS_2 channel [Fig. 11(b)]. Due to the optical control of ferroelectric switching, the devices with the BTO film could realize light-tunable synaptic functions.[200]

For 2D ferroelectric materials, $CuInP_2S_6$ (CIPS) and α-phase In_2Se_3 are widely used in optoelectronic artificial synapses and optoelectronic memristors.[201,202] Liu *et al.* reported an optoelectronic synapse based on α-In_2Se_3, which can achieve controllable temporal dynamics under electrical and optical stimuli. The 2D ferroelectric materials could couple the ferroelectric and optoelectronic processes, and a multimode reservoir computing (RC) system was also established by the α-In_2Se_3 devices.[203] Moreover, due to the electro/photo-induced ferroelectric reversal, Cai *et al.* also utilized the ferroelectric semiconductor α-In_2Se_3 to construct a retina-like visual system [Figs. 11(c) and 11(d)].[204]

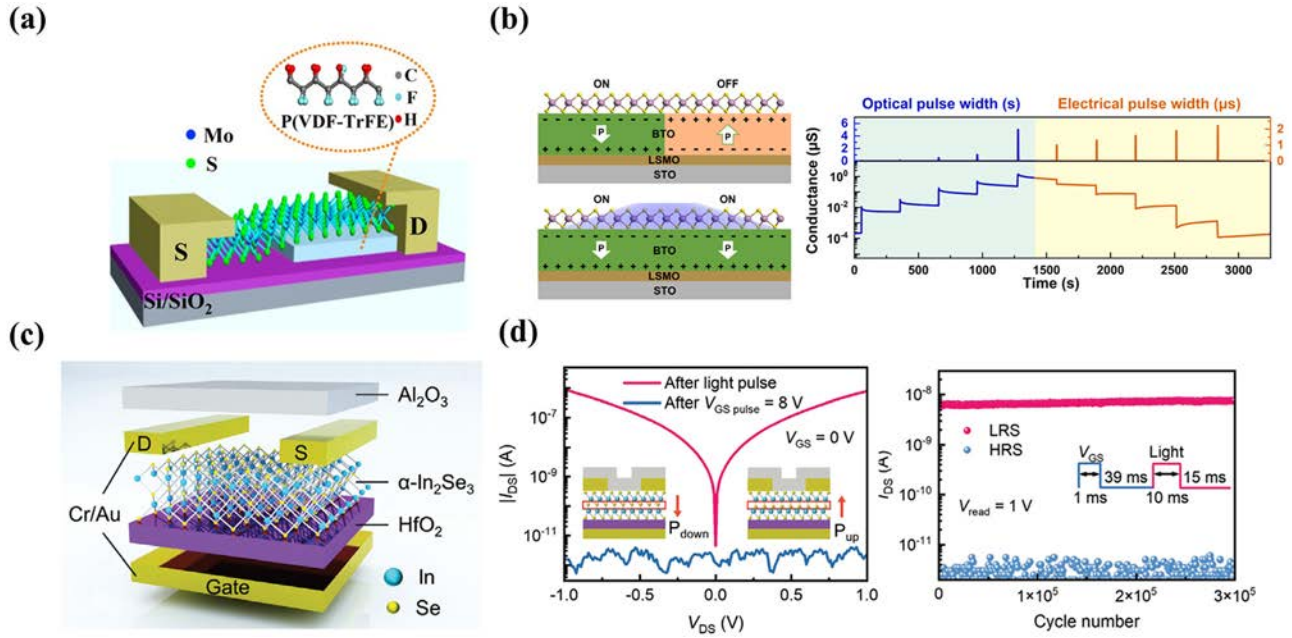

FIG. 11. (a) Schematic diagram of the device and the molecular of P(VDF-TrFE).[199] Parts of the MoS_2 channel are covered by the ferroelectric layer, which caused the asymmetric channel structure. Reproduced with permission from Jiang *et al.*, ACS Nano **16**, 11218–11226 (2022). Copyright 2022 American Chemical Society. (b) Schematic diagram of the photo-induced polarization switching process in the ferroelectric film (left). The nonvolatile multi-level storage functions induced by optical and electrical excitation (right). Reproduced with permission from Du *et al.*, Nano Energy **89**, 106439 (2021).[200] Copyright 2021 Elsevier. (c) Schematic of the device based on the ferroelectric 2D material and (d) the output characteristics of the device after a light pulse and a positive gate pulse (left). Its corresponding low resistance state (LRS) and high resistance state (HRS) (right).[204] Reproduced with permission from Cai *et al.*, Adv. Funct. Mater. **33**, 2212917 (2023). Copyright 2023 Wiley-VCH.

E. Gas adsorption/desorption and vacancy immigration

Due to the ultra-thin structure, the external environment can also have a particular impact on low-dimensional materials. Among them, gas adsorption and desorption are widely introduced to realize synaptic functions.[205] Ho's group utilized the $InGaO_3(ZnO)_3$ superlattice NWs to build the artificial visual system. The oxygen adsorption on the interface of the NWs would induce charge trapping. Then, the light pulse would desorb the oxygen on the NWs and increase the carrier concentration in the channel.[206] Tian *et al.* adopted the 2D oxygen-mediated platinum diselenide ($PtSe_2$) as the channel material to mimic the human visual system [Fig. 12(a)]. The artificial optoelectronic synapse exhibited a wavelength-dependent bipolar photoresponse induced by the photon-mediated physical adsorption and desorption of oxygen molecules.[207] Li and the co-workers adopted palladium diselenide ($PdSe_2$) as the channel layer to fabricate the artificial photosynapse. The absorption oxygen molecules on the $PdSe_2$ surface served as the electron acceptor and were stabilized by the Se vacancies. When the light irradiated on the channel, the desorption process of oxygen molecules was boosted, resulting in charge injection into the $PdSe_2$ and increasing electron concentration [Fig. 12(b)].[208] In addition to oxygen, water vapor in the air can significantly impact device performance. Zhang *et al.* utilized PVA/GO as the dielectric layer, which could retain many water molecules from the air [Fig. 12(c)]. When the stimulation was applied on the gate, the electric double layer would be formed in the PVA/GO dielectric layer and continuously impacted on rubrene single-crystalline nanoribbon channel.[209]

For vacancy immigration, there are several types of vacancies, including oxygen vacancies, intrinsic vacancies in low-dimensional materials, and other vacancies that could immigrate under external stimulation.[210] Miao *et al.* demonstrated the high thermally stable memristor with a vertical graphene/$MoS_{2-x}O_x$/graphene structure. More sulfur vacancies were generated in the $MoS_{2-x}O_x$ layer during the external stimulus, forming conductive channel regions. The "off" state was then attributed to the occupation of sulfur vacancies in the channel by oxygen ions, which was similar to the pristine $MoS_{2-x}O_x$ material.[211] Li *et al.* combined ZnO and PbS QDs to construct the vertical structure with ITO/ZnO/PbS/ZnO/Al. Owing to the absorption range of PbS QDs, 365 and 980 nm light stimuli could control the oxygen vacancies in ZnO and realize the excitatory and inhibitory characteristics for synaptic devices, respectively [Fig. 12(d)].[120]

F. Conductive filament

In resistive switching memory devices, conductive filaments play a crucial role in the switching behavior and information storage, which are widely used in two-terminal memristors.[212] In conventional resistive memristors, filaments are formed within the active material, which exhibits reversible resistance changes when subjected to electrical

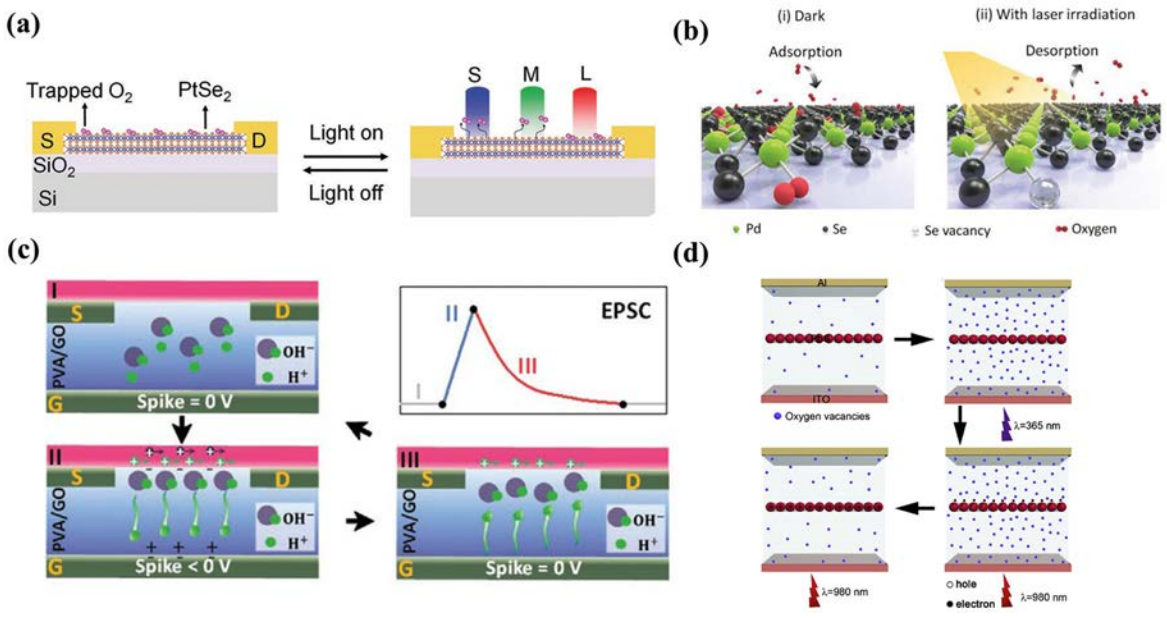

FIG. 12. (a) Bioinspired bilayer $PtSe_2$ device based on the oxygen adsorption/desorption process.[207] The shorter-wavelength optical pulses with higher photon energy (S and M) would cause oxygen desorption on the $PtSe_2$ surface, while the longer-wavelength light pulses would not. The process of oxygen adsorption causes a decrease in the photocurrent of the devices. Reproduced with permission from Tan *et al.*, Adv. Mater. **34**, 2206816 (2022). Copyright 2022 Wiley-VCH. (b) Schematics of the mechanisms of the n-doping process before and after laser irradiation.[208] The atmospheric oxygen molecules initially adsorbed on the $PdSe_2$ surface serve as the electron acceptor and are stabilized by the Se vacancies. Under laser irradiation, oxygen desorption is boosted, increasing the electron concentration. Reproduced with permission from Li *et al.*, Adv. Funct. Mater. **31**, 2007587 (2021). Copyright 2021 Wiley-VCH. (c) A schematic of forming EPSC is divided into three stages.[209] Stage one shows the device in the off state. Stage two demonstrates the negative spike attracting the H^+ toward the gate electrode and repelling the hydroxyls (OH^-) toward the interface. Stage three shows the slow process of recombination when the spike is removed. Reproduced with permission from Zhang *et al.*, Adv. Funct. Mater. **31**, 2007894 (2021). Copyright 2021, Wiley-VCH. (d) Resistive modulation mechanisms of the two-terminal device with the participation of light irradiation.[120] When UV light is applied, more carriers in ZnO are generated due to ionization and oxygen vacancies, increasing the channel conductivity. Reproduced with permission from Li *et al.*, Nano Energy **65**, 104000 (2019). Copyright 2019 Elsevier.

stimuli.[213,214] It is noted that, for optoelectronic memristors, light stimulation is added as a new channel to modulate the device's performance.[122,215] Han's group fabricated the artificial visual neuron with the structure of Ag/black phosphorous NSs-$CsPbBr_3$ QDs/ITO. The Ag conductive filament would be formed or ruptured under electronic pulses like a traditional two-dimensional memristor. By introducing the temporal heat summation effect, the light irradiance could increase the device temperature for modulating the growth and rupture of the Ag filament in the active layer [Figs. 13(a) and 13(b)].[125] Yu *et al.* demonstrated the artificial optoelectronic hybrid-integrated neuron (AOHN) based on the ITO/PVA-MXene-Ag NPs/Ag. The switching between the high resistance state (HRS) and the low resistance state (LRS) was attributed to the drift of Ag^+ ions and the formation of Ag conductive filament [Figs. 13(c) and 13(d)]. Moreover, to mimic the leaky integrate-and-fire (LIF) neurons, the firing time could be reduced obviously by the synergetic regulation of photoelectric pulses.[216]

V. OPTOELECTRONIC ARTIFICIAL SYNAPSES FOR THE VISUAL SENSOR SYSTEM

Nowadays, various low-dimensional materials with excellent photoelectric performance have been introduced into artificial visual synaptic devices. Actually, the integration of light into synaptic devices presents a novel approach for stimulating neural activities and synaptic functions, leading to the accelerated development of brilliant neuromorphic devices. The optoelectronic synaptic devices triggered by the photoelectric synergistic stimuli offer a novel approach that mimics biological synaptic processes and contributes to the advancement of highly intelligent neuromorphic devices.[217] In addition, the fundamental synaptic functionalities, such as EPSC, LTP/long-term depression (LTD), SRDP (short-term response potentiation), and STDP (spike-timing-dependent plasticity), establishing a connection between optoelectronic synaptic devices and neuromorphic applications is of great significance.

A. Images and pattern recognition

As one of the most essential means for organisms to obtain external information, vision has always been the object of pursuit of bionics.[218] For human beings, more than 80% of information is obtained through the eyes. Therefore, pattern and image recognition have become one of the most popular applications of artificial synaptic devices. The process of acquiring information through vision involves the process of various signal transmissions, and the retina plays a crucial role in converting light signals into electrical impulses that the brain can interpret. The retina contains two types of photoreceptor cells called rods and cones. These necessary photoreceptors are responsible for vision in dim light conditions (rods), color vision, and visual acuity in bright light conditions (cones). Based on this supported biological

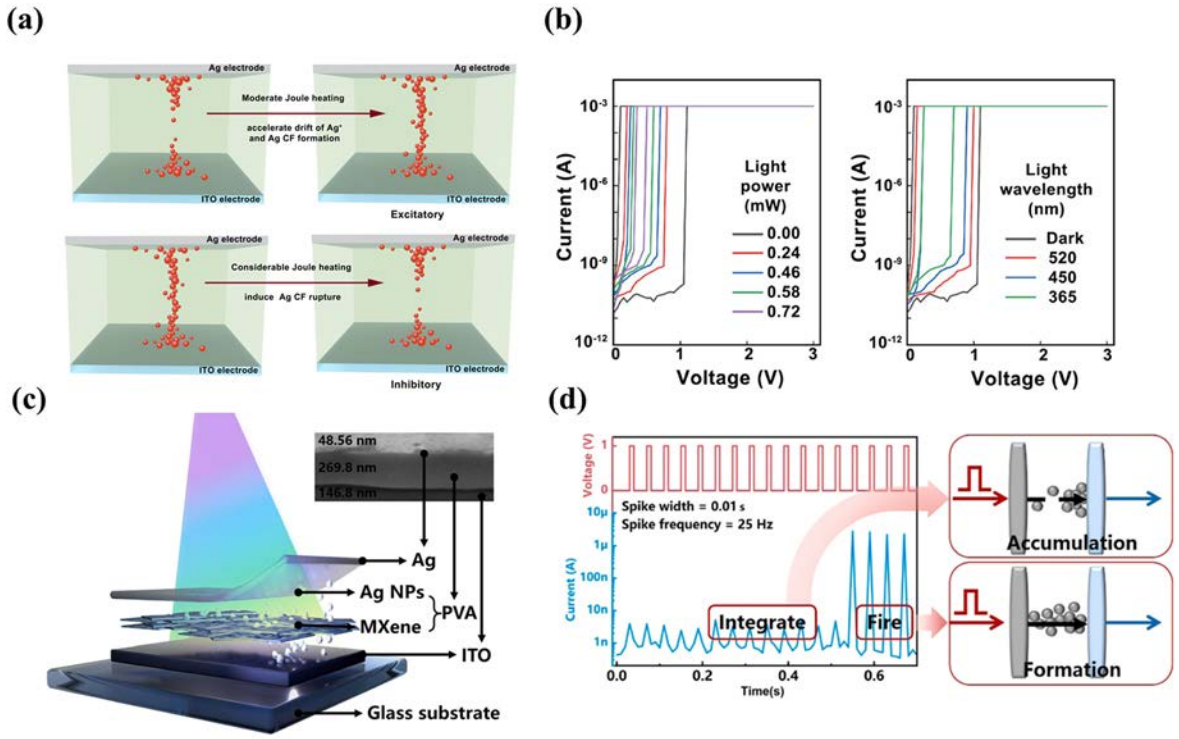

FIG. 13. (a) The metal drifted process to induce the formation of Ag CFs with the moderate Joule heating effect. Reproduced with permission from Wang *et al.*, Nat. Commun. **12**, 5979 (2021).[125] Copyright 2021 Springer Nature. (b) I–V characteristics of the device under positive sweeping with different light powers (left) and light wavelengths (right). Reproduced with permission from Wang *et al.*, Nat. Commun. **12**, 5979 (2021).[125] Copyright 2021 Springer Nature. (c) Schematic diagram of a device consisting of a MXene/Ag NPs resistive layer between Ag/ITO electrodes. Reproduced with permission from Yu *et al.*, Nano Energy **99**, 107418 (2022).[216] Copyright 2022 Elsevier. (d) Integrate and fire behaviors induced by a series of electrical spikes (1 V in amplitude, 10 ms in width, and 25 Hz in frequency) and corresponding ion diffusion mechanism. Reproduced with permission from Yu *et al.*, Nano Energy **99**, 107418 (2022).[216] Copyright 2022 Elsevier.

theory, Kim's group fabricated the curved neuromorphic image sensor array based on a heterostructure of MoS_2 and poly(1,3,5-trimethyl-1,3,5-trivinyl cyclotrisiloxane).[219] Zhu *et al.* prepared a flexible optoelectronic sensor array of 1024 pixels based on the combination of CNTs and $CsPbBr_3$ QDs [Fig. 14(a)]. The 32×32 sensor array could realize the neuromorphic reinforcement learning with 405 nm light process and achieve 95% accuracy on image recognition.[30] Moreover, Shao *et al.* adopted Zr^{4+}-doped $CsPbI_3$ perovskite nanocrystal to fabricate the perovskite/pentacene artificial visual synapse [Fig. 14(b)]. Due to the optically reconfigurable and wavelength selected ability, the functions of artificial synapse and nonvolatile memory were realized within a single device for the specific purpose.[220] Not only heterojunction structure but adding other functional layers to the device design can also enhance the recognition ability of artificial visual nerves. Yu *et al.* utilized the ferroelectric P(VDF-TrFE) layer to change the ability of artificial synapses to store ultraviolet band information. The channel materials based on the poly [2, 5-bis (alkyl) pyrrolo-[3, 4-c]pyrrole-1, 4(2H, 5H)-dione-alt-5, 50-di(thiophen-2-yl)-2, 20-(E)-2- (2-(thiophen-2-yl)vinyl)thiophene] (PDVT-10) and CdSe/ZnS QDs heterojunction can separate the photogenerated carriers efficiently. In addition, the core–shell structure of quantum dots can inhibit the transfer of photogenerated electrons into the PDVT-10 organic film and realize the nonvolatile characteristic [Fig. 14(c)].[221]

At present, bionics for biological vision not only stays at photoreceptors but also comes to the output end of the retina. Much work has also focused on the transmission process of bipolar cells transmitting visual information to other neurons in the retina. The two working states, named "on" and "off" states, of bipolar cells refer to the activity patterns in response to visual stimuli. Miao *et al.* applied gate voltage on the synaptic devices to realize the positive and negative photoconductivity.[155] Zhou's group used the characteristics of bipolar cells in motion detection and recognition. The positive gate voltage would cause the electrons of WSe_2 to tunnel into the metal gate through the h-BN, and the remaining holes would enhance the channel conductance. On the contrary, the negative gate voltage with optical stimuli would help stored holes absorb photon energy to leap the WSe_2/h-BN interface barrier, reducing channel current. Combining with interframe differencing computations, the synaptic devices achieved high-quality recognition of moving objects with different colors.[222] Due to the surface characteristics and ultra-thin atomic structure, the atmospheric environment also can affect the device's performance. Tan *et al.* utilized the 2D oxygen-mediated $PtSe_2$ as the channel material to mimic the human visual system. The photon-mediated physical adsorption induced the wavelength-dependent bipolar photoresponse and desorption of oxygen molecules on the surface of the 2D materials.[207] In addition to human vision, the visual system of insects is also an attractive research direction. Compared with the human visual system, insect vision demonstrates several advantages in broad spectrum sensitivity, high frame rate and fast visual processing, wider field of view (compound eyes), sensitivity motion detection, and polarized light perception. Chai *et al.* demonstrated bionic insect vision and investigated optoelectronic graded neurons for agile in-sensor motion perception. The shallow trapping centers in the MoS_2 channel layer could mimic the characteristics of graded neurons and realize a high information transmission rate and 99.2% recognition accuracy.[223] Hu's group demonstrated a vertical transistor based on MXene and organic single crystal, unlike the conventional three-terminal structure. The 2,6-diphenylanthracene (DPA) single crystal was grown by an out-of-plane sublimation process, and MXene served as the source electrode under the organic single crystal. The artificial synaptic devices achieved an ultra-low power consumption of 8.7 aJ per spike while mimicking various neural functions. In addition, with the help of gate

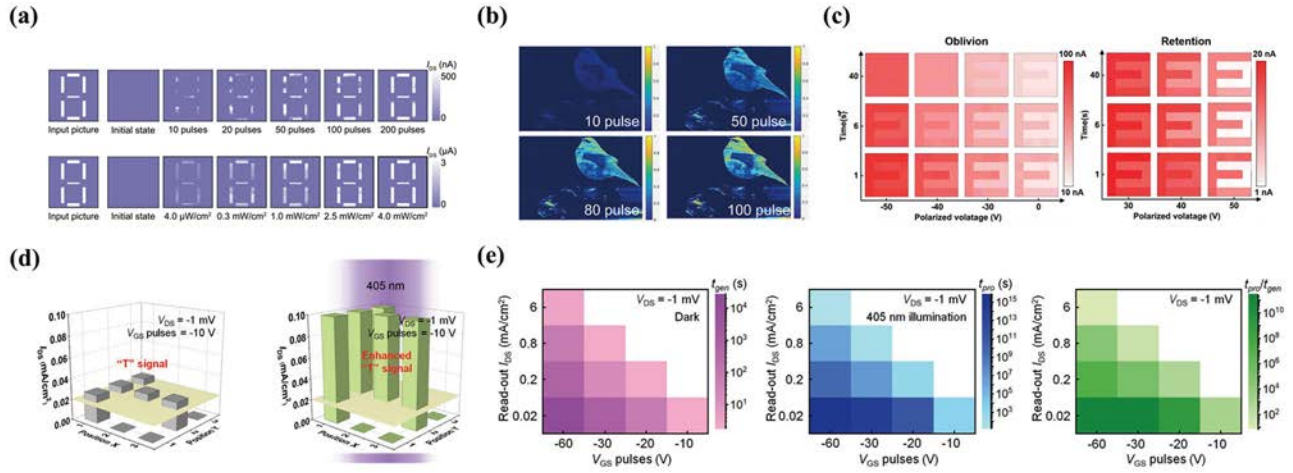

FIG. 14. (a) Change of the training weight with a number "8" pattern before and after training.[30] The top process shows the training process with different pulse numbers, and the bottom process demonstrates the process with different light powers. Reproduced with permission from Zhu *et al.*, Nat. Commun. **12**, 1798 (2021). Copyright 2021 Springer Nature. (b) Difference of the color with the increasing number of light pulses. Reproduced with permission from Shao *et al.*, Adv. Mater. **35**, 2208497 (2023).[220] Copyright 2023 Wiley-VCH. (c) Encoded images under different polarization states.[221] The left panel shows the encoded process under negative polarization (−30, −40, and −50 V) and without polarization (0 V), and the right panel shows the process under positive polarization (30, 40, and 50 V). Reproduced with permission from Yu *et al.*, Nat. Commun. **13**, 7019 (2022). Copyright 2022 Springer Nature. (d) Image recognition of the "T" signal with the 3×3 array. Reproduced with permission from Zhang *et al.*, Adv. Mater. **35**, 2208600 (2023).[224] Copyright 2023 Wiley-VCH. (e) The values of t_{gen} as a function of the amplitude of V_G pulses (left). The values of t_{pro} as a function of the amplitude of V_G pulses (middle) and the values of t_{pro}/t_{gen} as a function of the amplitude of V_G pulses (right). Reproduced with permission from Zhang *et al.*, Adv. Mater. **35**, 2208600 (2023).[224] Copyright 2023 Wiley-VCH.

voltage, the synaptic device can effectively memorize information from 405 nm wavelength [Figs. 14(d) and 14(e)].[224] The corresponding summary of the artificial synapses for use in images and pattern recognition is shown in Table I.

B. Logic operation

Nowadays, logical operations still play a crucial role in information processing, data analysis, and decision-making. The logic functions, which are fundamental to computation, could be effectively emulated in optoelectronic synapses. Due to the advantages of higher bandwidth, faster speed, better robustness, and lower crosstalk, optical signal as an ideal information transmission carrier is utilized in optoelectronic synaptic devices to perform neuromorphic logic operations. Hou *et al.* constructed the large-area two-terminal optical synapse based on the pyrenyl graphdiyne (Pyr-GDY)/graphene/PbS QDs heterostructure. Due to the strong photogating effect induced by Pyr-GDY and PbS QDs with different wavelength light, excitatory and inhibitory synaptic behaviors could be realized in synaptic devices. Specifically, the 450 nm light irradiation would induce more photogenerated electrons from Pyr-GDY to inject into the graphene and cause the positive photogating effect leading to a decreased conductance for the graphene channel. In contrast, PbS QDs served as the primary

TABLE I. Summary of optoelectronic synaptic devices for applications in images and pattern recognition.

Compound	Substrate	Working wavelength	Working mechanisms	Bipolar photoresponse	Power consumption	References
HfS_2	Si/SiO_2	405 nm	Trap states	No	…	225
MoS_2	Sapphire	Blue light	Trap states	No	…	226
poly(3,4-ethylenedioxythiophene) polystyrene sulfonate (PEDOT:PSS)/CuSCN/$CsPbBr_3$	ITO	365 nm	Band engineering/ trap states	No	…	227
PDVT-10/$Cs_2AgBiBr_6$	Si/SiO_2	303 nm	Floating gate	No	…	29
C8-BTBT/$PC_{61}BM$/InGaAs	Si/SiO_2	261/405/450 nm	Band engineering	Yes	…	61
ReS_2	Si/SiO_2	552/860 nm	Trap states	No	…	228
In_2Se_3/MoS_2	Quartz/PET	1060 nm	Band engineering	No	28 fJ	132
$CsPb(Br_{0.5}I_{0.5})_3/MoS_2$	Si/SiO_2	405/532/638 nm	Band engineering	Yes	…	229
$CsPbBr_3$/PDPP-TT	Si/SiO_2	365 nm	Band engineering	Yes	…	28
Graphene/MoS_2	Si/SiO_2	532 nm	Band engineering	No	…	230
PV3D3/MoS_2	Si_3N_4	532 nm	Band engineering	No	…	219
$PtTe_2/MoS_2$	Si/SiO_2	300/450 nm 1/2 μm	Band engineering/ Trap states	No	…	99
In/MoS_2	Quartz	550 nm	Band engineering	No	68.9 aJ	181
Ag NW/TiO_2	F-doped Tin Oxide (FTO)/glass	365 nm	Trap states	No	29 μJ	231
Graphene/Perovskite QDs	Si/SiO_2	440 nm	Band engineering/ Floating gate	No	36.75 pJ	131
PDVT-10/QDs/P(VDF-TrFE)	Si/SiO_2	365/520/650 nm	Band engineering/ ferroelectric polarization	No	…	221
WSe_2/h-BN/BP	Si/Al_2O_3	450/520/637 nm	Floating gate	Yes	…	222
WSe_2/h-BN/Al_2O_3	Metal/ Al_2O_3	450/650 nm	Trap states	Yes	…	155
BP/P_xO_y	Si/Al_2O_3	280/365 nm	Trap states	Yes	…	162
IGZO/Perovskite QDs	Glass	405/519/635 nm	Band engineering	No	0.5 pJ	32
$PtSe_2$	Si/SiO_2	450/532/650 nm	Gas adsorption/ desorption	Yes	0.29 fJ	209
MXene/DPA	Si/SiO_2	405 nm	Trap states	No	8.7 aJ	224
Zr-$CsPbI_3$/Pentacene	Si/SiO_2	405/520/650 nm	Band engineering/ floating gate	No	…	220
CNT/$CsPbBr_3$ QD	Rigid/ Al_2O_3/PEN	405/516 nm	Band engineering	No	…	30
WSe_2/Al_2O_3	/	473/532/655 nm	Floating gate	No	40 fJ	232
SnS	Si/SiO_2	455/638/725/811 nm	Trap states	No	…	233
ReS_2/h-BN/Gr	Si/SiO_2	450/532/650 nm	Floating gate	No	0.06 nJ	234
ReS_2/h-BN/Gr	Si/SiO_2	405/520/650 nm	Floating gate	No	…	235
PDVT-10/$CsPbBr_3$ QDs	Si/SiO_2	450 nm	Band engineering	No	…	236

light-absorbing material for 980-nm light irradiation; more photogenerated holes would transfer to the graphene channel under the light irradiation resulting in a higher photocurrent. Therefore, under the combination of negative/positive photoconductivity, the logic functions of AND/OR and NOR/NAND can be achieved [Fig. 15(a)].[237] Yang *et al.* used 2D materials to construct a vdW heterostructure based on the MoS_2/h-BN/Gr [Fig. 15(b)]. With the stimulation of gate voltage and light irradiation, the electrons could tunnel between the Gr floating gate and the MoS_2 channel across the thin h-BN barrier. Therefore, AND/OR/NAND/NOR logic functions could be realized by different combinations of program conditions (different combinations of V_G and light pulses).[238] In addition to the inorganic materials, organic semiconductor materials are also widely used in logic functional artificial synapses. Liu's group adopted PDPP-DTT to fabricate the organic–inorganic heterojunction with PbS QDs. Figure 15(c) demonstrates that optical synaptic devices can simulate the typical biological behavior under NIR and short-wave infrared (SIR) irradiation and realize the AND/OR logic function because of the different photoresponse in 850 and 1100 nm.[172] Different from the planar heterojunction, Zhang *et al.* utilized the bulk heterojunction to fabricate the flexible optoelectronic synaptic transistors. The $CsPbBr_3$ QDs and the organic semiconductor poly[2,5–(2-octyldodecyl)-3,6-diketopyrrolopyrrole-alt-5,5–(2,5 di(thien-2-yl)thieno [3,2-b]thiophene)] (DPP-DTT) could generate more trap centers because the high surface-to-volume ratio of the 0D QDs. During the photonic operation, photogenerated holes were easily transferred from $CsPbBr_3$ QDs to DPP-DTT, resulting in the photogate effect after removing the light. Similar to other works, under the systematic regulation of optical pulses and gate voltages, the logic functions of AND, OR, NOR, and NAND operations could be realized by the optoelectronic synaptic devices [Fig. 15(d)].[239] Table II shows the characteristics of synaptic devices based on logic operation usage.

C. Neuromorphic computing

Neuromorphic computing as a popular development direction in recent years that seeks to design and build computer systems inspired by the structure and function of the human brain.[248] Traditional computing architectures, such as the von Neumann architecture used in most computers today, are based on digital logic circuits that execute

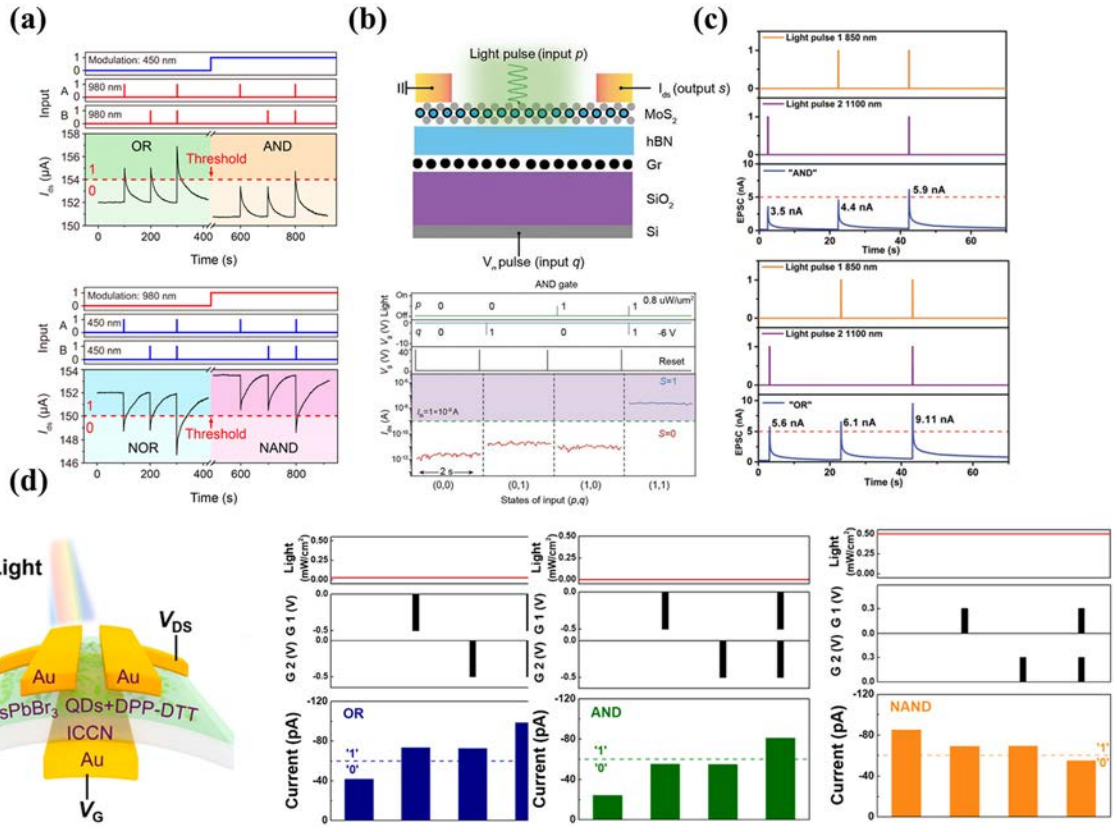

FIG. 15. (a) Two logic functions realized by using 980 nm light pulse inputs and 450 nm irradiation as modulatory input (up). Realization of "NOR" and "NAND" logic functions by using the opposite combination of light stimulation (down). Reproduced with permission from Hou *et al.*, ACS Nano **15**, 1497–1508 (2021).[237] Copyright 2021 American Chemical Society. (b) Schematic diagram of the logic device (up). Gr plays an important role as a trapping layer for storage. The "AND" function was realized by using light and voltage pulses as the logic inputs. Reproduced with permission from Yang *et al.*, Adv. Funct. Mater. **32**, 202207290 (2022).[238] Copyright 2022 Wiley-VCH. (c) The logic functions are realized based on EPSC responses with 850 and 1100 nm light. Reproduced with permission from Huang *et al.*, Adv. Funct. Mater. **33**, 2208836 (2023).[172] Copyright 2023 Wiley-VCH. (d) Schematic of the flexible synaptic devices array (left). The three logic operation with synchronous optoelectronic input characteristics for the synaptic devices (right). Reproduced with permission from Zhang *et al.*, Nano Energy **95**, 106987 (2022).[239] Copyright 2022 Elsevier.

TABLE II. Characteristics of the synaptic devices based on logic operation usage.

Compound	Function type	Working wavelength	Bipolar photoresponse	Stimulus type	References
MoS_2/hBN/Gr	AND/OR/NAND/NOR	532 nm	No	Voltage/light	238
Bi_2O_2Se/Gr	AND/OR	365/635 nm	Yes	Light	240
WSe_2/h-BN	NAND/NOR/XOR	405 nm	Yes	Voltage/light	241
Si NCs	AND/OR	1342 nm	Yes	Voltage/light	242
Gr/h-BN/WSe_2	AND/OR	532 nm	No	Voltage/light	243
PDVT-10/Perovskite QDs	AND/OR	400/500 nm	No	Light	244
GDY/Gr	NAND/NOR	365/532/633 nm	Yes	Light	245
MoS_2	AND/OR	466 nm	No	Voltage/light	246
PDPP:C_6Si/PbS QDs	AND/OR	850/1100 nm	No	Light	172
Pyr-GDY/Gr/PbS QDs	AND/OR/NAND/NOR/XOR	450/980 nm	Yes	Voltage/light	237
DPP-DTT/$CsPbBr_3$ QDs	AND/OR/NAND	450 nm	No	Voltage/light	239
Pt/$PtSe_2$	AND/OR	405/980 nm	Yes	Light	247
MoS_2/h-BN/Gr	AND/OR/NAND/NOR	532 nm	Yes	Voltage/light	238

instructions sequentially. In contrast, neuromorphic computing aims to develop computing systems that mimic the brain's massively parallel and energy-efficient nature.[249] Furthermore, inspired by the brain's ability to modify the strength of connections between neurons (synaptic plasticity), neuromorphic computing architectures can adapt and learn from input data, making them suitable for applications such as machine learning and artificial intelligence.[250,251] Moreover, these systems can leverage the principles of synaptic plasticity, allowing them to modify the strength of connections between artificial neurons in response to patterns and stimuli.[252] The widely used neural network architectures mainly include artificial neural networks (ANN) and recurrent neural networks (RNN). Among them, ANN is a broad term that encompasses various neural network architectures, including spiking neural network (SNN), binary neural network (BNN), and convolutional neural network (CNN). At the same time, reservoir computing (RC) is one of the most famous frameworks under the umbrella of RNN.

Optoelectronic artificial synapses have a more diverse input and greater information capacity than conventional synaptic devices based on electronic stimuli. The sensor-memory-computing integrated devices based on optoelectronic synapses can perform neuromorphic computing more efficiently. Yang's group utilized α-In_2Se_3 to fabricate the optoelectronic synaptic devices because of the ferroelectric property of this 2D material. Due to the multiple inputs (electricity and light), the mixed-input RC was realized to complete the complex recognition task. This work's electrical and optical stimuli stimulated tactile and visual information. When only part of the information was acquired, the effective identification of the entire image can still be completed with mixed-input reservoir computing.[203] Miao's group fabricated the optoelectronic synapse based on WSe_2/h-BN/Al_2O_3 vdW heterostructures with gate-tunable photoresponses. The RNN was constructed with two input neurons, ten hidden neurons, and two output neurons and then realized the certain predictive function [Fig. 16(a)].[253] CNN is a specialized type of ANN explicitly designed for processing grid-like data, such as images and videos. Lee *et al.* utilized the CNN to realize the high recognition accuracy with the Al_2O_3/HfO_2/Al_2O_3/BP device structure. The same as the typical CNN framework, the structure of three layers was constructed, including the input layer, which could receive a 28 × 28-pixel image, a convolution layer with two 3 × 3 kernels, and an average pooling layer followed by an 8 × 2 fully connected (FC) layer. After training offline with 12 000 images of the training set with 100 epochs, the image recognition rate of the neural network model can reach 99%.[141] Hu *et al.* also adopted the CNN framework into organic 2D heterojunction optoelectronic artificial synapses. The P-type dithieno[3,2-b:20,30-d]thiophene derivatives (DTT-8) and n-type 2,2′-((5*Z*,5′*Z*)-5,5′-(furan-2,5-diylidene)bis(4-octylthiophene-5,2(5*H*)-diylidene)) dimalononitrile (TFT-CN) were selected as the layer heterojunction. Under the different V_G, the negative and positive photoconductivities were realized. Then, after training by the CNN network, eight classical objects in road traffic with a correct rate of more than 90% was achieved [Fig. 16(b)].[254] Finally, as a general term encompassing a wide range of neural network architectures, ANN is also widely used in neuromorphic computing. However, because of the lack of corresponding special optimization, the traditional ANNs often struggle with high-dimensional data and fail to capture the spatial relationships in the data. Xu's group demonstrated stretchable and wearable optoelectronic devices with P3HT/poly(ethylene oxide) (PEO) NWs. The research group utilized the strain as a signal source through a stretchable substrate and enriched the device's perception of motion and behavior. A four-layer ANN and the backpropagation algorithm were used for training [shown in Fig. 16(c)]. Because the change of device weight was related to the strain caused by different gestures, the optoelectronic devices showed the 96.3% action recognition accuracy after 500 epochs of training.[255]

D. Associative learning

Associative learning, inspired by the memory processes in the brain, involves the ability to recall or retrieve memories by forming connections between the environment and biological reactions or experiences. In other words, associative learning refers to the process by which an individual learns to associate two or more stimuli or events. This process further indicates that once one event is reexperienced, the other event will be also recalled. Classical conditioning, known as Pavlovian conditioning, is also one of the most widely mimicked in the synaptic behavior and involves associating an initially

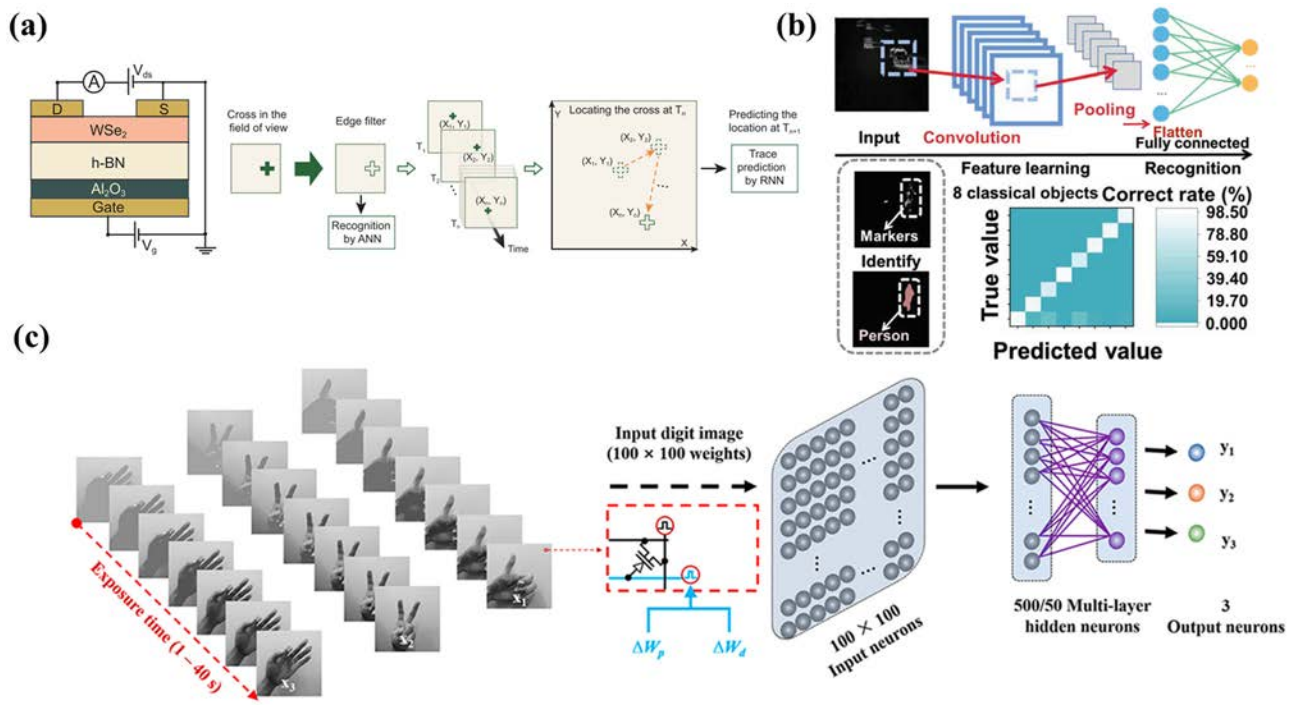

FIG. 16. (a) Schematic diagram of the device (left) and the flow chart of the object tracking based on the neuromorphic vision system. Reproduced with permission from Wang *et al.*, Natl. Sci. Rev. **8**, nwaa172 (2021).[253] Copyright 2021 Oxford University Press. (b) Recognition for the tagged objects with an already CNN. The network successfully identified eight classical objects with a more than 90% recognition rate. Reproduced with permission from Zhu *et al.*, Adv. Mater. **35**, 2301468 (2023).[254] Copyright 2023 Wiley-VCH. (c) Neuron network structure for pattern recognition.[255] Iteration of the multistage neural network that used nanowire-channel intrinsically stretchable neuromorphic transistors (NISNTs) with positive or negative weights, leading to the recognition of the meaning of the three types of gestures. Reproduced with permission from Liu *et al.*, ACS Nano **16**, 2282–2291 (2022). Copyright 2022 American Chemical Society.

neutral stimulus (conditioned stimulus, CS) with a biologically significant stimulus (unconditioned stimulus, US) to elicit a response. The associative learning has been well illustrated by Pavlov's dog experiment, where electrical and light pulses are severed as bell-ring (CS) and food-sight (US), respectively [Fig. 17(a)].[138] The only CS input cannot let the PSC beyond the threshold for salivation, and the only US input could induce a large change of PSC over the threshold, leading to the appearance of salivation. Then, after applying two different inputs simultaneously, only the CS input could also induce the salivation reaction [Fig. 17(b)].[256] As discussed above, the low-dimensional materials-based optoelectronic synaptic devices have the advantage of input diversification, which is suitable to realize associative learning by different input stimuli.[257,258] Chen *et al.* utilized the absorptive capacity in the solar-blind range of SnO_2 NW to take the 275 nm spikes as the US. Moreover, the electrical pulses at the gate emulate the bell-ring (CS) for a conditioned response. Consistent with Pavlovian conditioning, when the mixed 20 pulses were applied, a larger PSC was induced, and the retention time of information will also increase. Therefore, when only CS was applied again, the PSC exceeded the threshold and showed a salivation reaction.[259]

VI. THE APPLICATION OF OPTOELECTRONIC MEMRISTORS

Optoelectronic memristors exhibit both electrical and optical properties, which can change the resistance based on the history of applied voltages or irradiation and store information in a nonvolatile manner.[260] Compared with the classical memristors, owing to the advantages of combining electrical and optical functionalities, optoelectronic memristors based on low-dimensional materials have shown great potential in image recognition, neuromorphic computing, and information storage.[261–263] Optoelectronic memristors combine the advantages of memristors and optoelectronics, which can store information in different resistance states while also responding to optical signals. Therefore, optoelectronic memory is one of the most critical applications for optoelectronic memristors. Moon *et al.* fabricated single-layer Gr/WS_2/single-layer Gr optoelectronic memristors to realize the storage of multiple conductance states under UV irradiation. The UV spikes would induce point defects, including sulfur vacancies and interstitial atoms in the host lattice, acting as n-type dopants in the WS_2 layer. Then, with the help of voltage, conductive channels were gradually formed, and the storage of multi-conductivity states was effectively realized [Fig. 18(a)].[264] In addition to that, it is similar to artificial optoelectronic transistors; pattern and image recognition are also crucial applications for optoelectronic memristors. Han *et al.* reported a NIR-resistive random-access memory (RRAM) based on the $MoSe_2/Bi_2Se_3$ heterostructure. Under NIR illumination with wavelengths of 790 nm, the device's transition from nonvolatile to volatile memory behavior was observed. When NIR illumination was applied in the device, photogenerated electrons could be trapped in the hybrid $MoSe_2/Bi_2Se_3$ nanosheets while free holes accelerated the rupture of

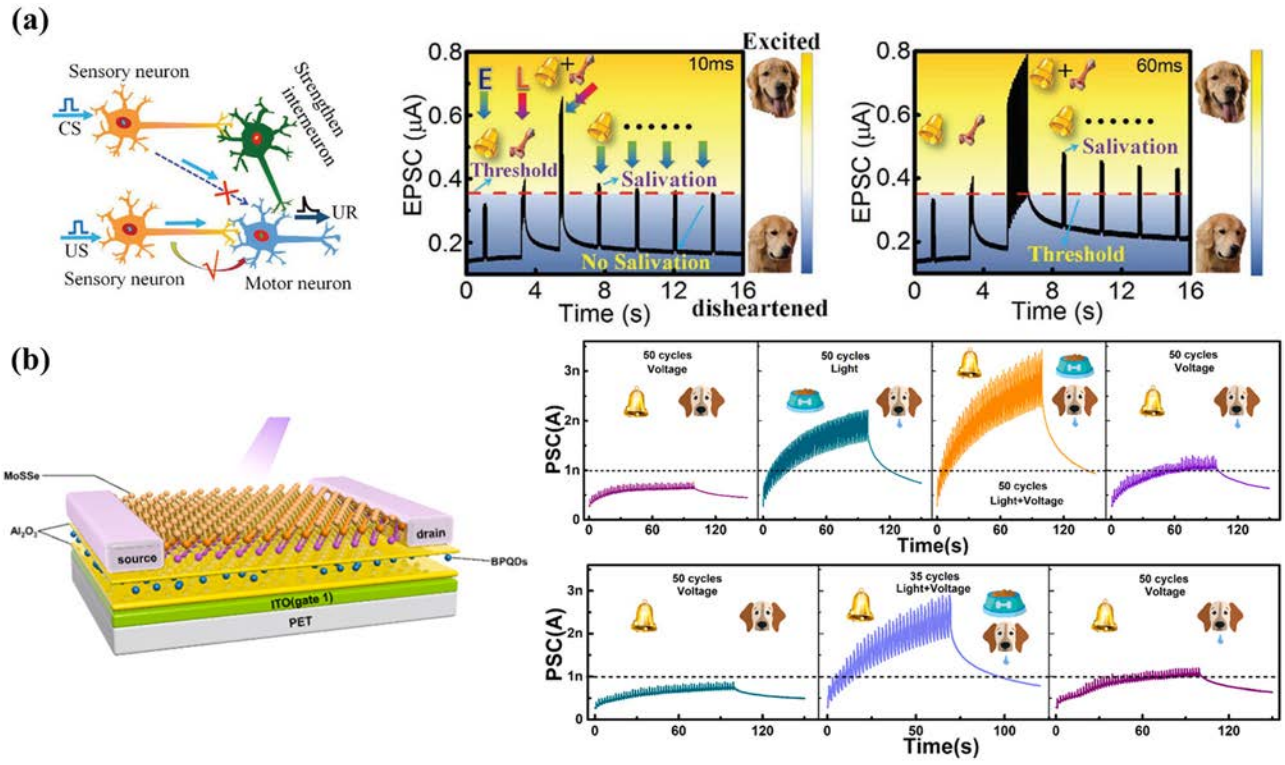

FIG. 17. (a) Schematic diagram of neurological principles for realizing associative learning (left). Pavlovian conditioning is mimicked by the devices (right).[138] 10 continuous electrical pulses are input as the bell stimuli, and 10 successive optical pulses are applied as the food stimuli. Moreover, increasing the pulse duration to 60 ms would produce a more efficient learning process. Reproduced with permission from Cheng *et al.*, Small **16**, 2005217 (2020). Copyright 2020 Wiley-VCH. (b) A schematic diagram of a synaptic device (left). QDs are used as the trapping layer, and Al_2O_3 is adopted as the tunneling layer and dielectric layer. The voltage pulses (CS) and light pulses (US) modulated the PSC to realize Pavlov associative learning. Reproduced with permission from Meng *et al.*, Nano Energy **83**, 105815 (2021).[256] Copyright 2021 Elsevier.

as-formed conductive Ag filaments. Furthermore, the optical assistance storage system with 12×12 array was fabricated. Through the current comparison of off-state (with NIR irradiation) and on-state (without NIR irradiation), the details of the figure can be identified and stored for over a week in the dark conditions.[128] A similar strategy for realizing the transition between nonvolatile resistive switching and volatile threshold switching modes was shown in the InP/ZnS quantum dot (QD) memristor. On the one hand, the UV (365 nm) irradiation would induce photogenerated holes in the core–shell InP/ZnS QDs and let them distribute in the outer shell. The formed Ag conductive filaments would undergo an oxidation reaction with the photogenerated holes on the surface to damage the conductive channel. Therefore, by comparing volatile and nonvolatile states, combined with the shadow mask pattern, the image's recognition and preservation can be realized [Fig. 18(b)].[265] Different from the "light-induced CF scission phenomenon," Shen *et al.* reported an $Ag/Ga_2O_3/MoS_2$/ITO heterojunction-based multi-modulated optoelectronic memristor with the optical excitation effect. Not only the voltage, the light irradiation would generate the photogenerated electron–hole pairs in two materials and separate at the interface of the heterojunction to form a conductive path [Fig. 18(c)].[266] The human vision is a powerful information acquisition, processing, and transmission system. However, limited by the size of the field of view, the range of light perception, and the upper limit of frequency recognition, human visual bionics still have problems in some applications. Therefore, starting from the essential functions of vision, biomimicry of insect vision can make up for the defects of unitary human vision biomimicry. Han's group demonstrated the biomimetic compound eye, which exhibited the wide field-of-view detection capability ($180^\circ \times 180^\circ$) and nonmonotonic collision avoidance response to the looming stimuli.[125] In this work, Ag/few-layer BP nanosheets and $CsPbBr_3$ QDs heterostructure/indium tin oxide (ITO) were fabricated. The 20×20 hemispherical flexible array showed the different photocurrent with the changing of the azimuthal angles of the light. Moreover, the light intensity was introduced to represent the distance or moving speed of the detected object. Therefore, this method identified detected objects efficiently and quickly, and optoelectronic memristors realized the movement-sensitive and wide-field visual system. Recently, Han *et al.* demonstrated the two-terminal optoelectronic synapse array based on the ZnO NWs/Al_2O_3/CdS heterojunction with tunable synaptic weights [Fig. 18(d)]. Due to the piezoelectric polarization property in ZnO NWs, the piezo-phototronic effect was used to modulate recognition.[267]

It is noted that the rapid development of artificial intelligence also inspires optoelectronic memristors. Neuromorphic computing and associative learning have also been extensively studied as application hotspots.[268,269] Liu *et al.* utilized the Au/TiS_3/ITO structure to realize

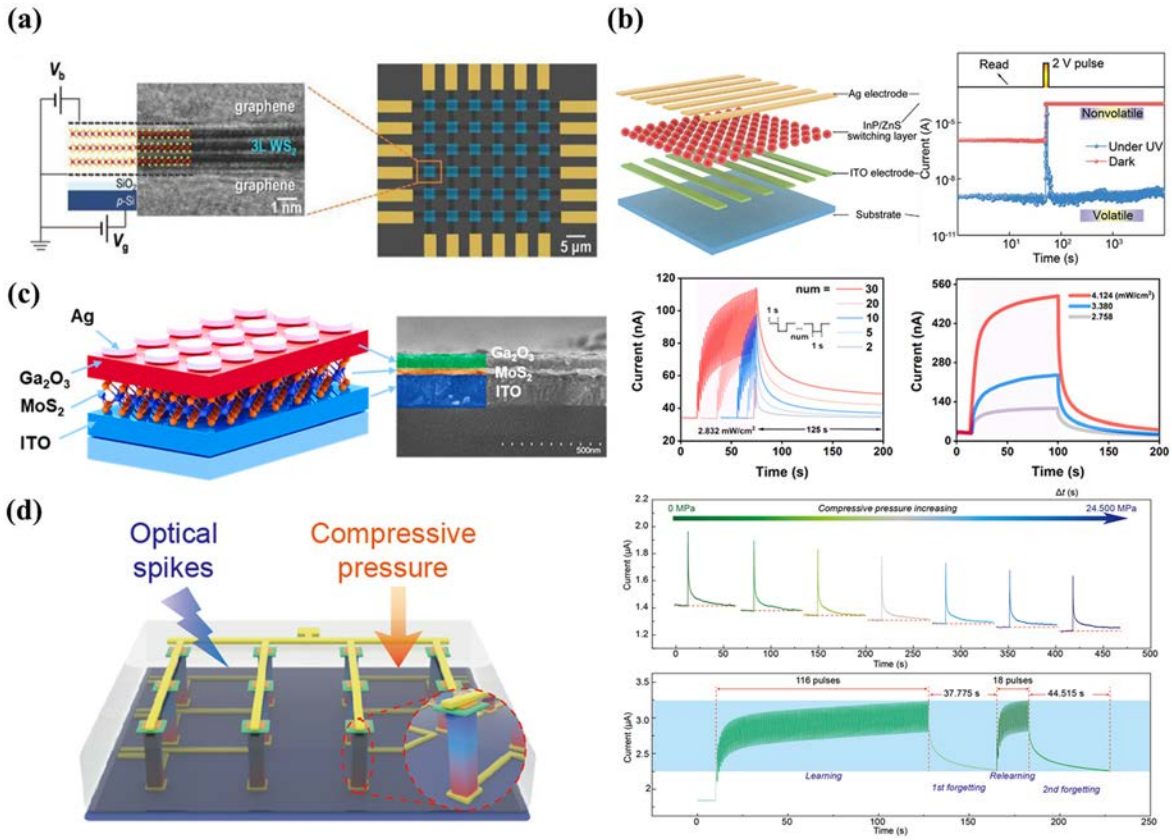

FIG. 18. (a) A cross-sectional TEM image of the vertical device structure (left) and a SEM image of the corresponding 6 × 6 crossbar array (right). Reproduced with permission from Moon *et al.*, Adv. Mater. **35**, 2203481 (2023).[264] Copyright 2023 Wiley-VCH. (b) Schematic of the vertical two-terminal architecture of the memristive device (left). The I–V curves under dark and UV illumination conditions by applying an electrical pulse (right). Reproduced with permission from Wang *et al.*, Adv. Funct. Mater. **30**, 1909114 (2020).[265] Copyright 2020 Wiley-VCH. (c) Schematic diagram of the device and the corresponding cross-sectional SEM image (left). The EPSCs of device under different number of light pulse and light intensity (right). Reproduced with permission from Li *et al.*, Nano Energy **111**, 108398 (2023).[266] Copyright 2023 Elsevier. (d) Schematic illustration of the device and the working mechanism (left). The EPSCs with a single UV pulse under various strain conditions and showed the learning function by piezo-phototronic effect under UV light stimuli (right). Reproduced with permission from Han *et al.*, Adv. Electron. Mater. **9**, 2201068 (2023).[267] Copyright 2023 Wiley-VCH.

the classical conditioning. The irradiation would induce photogenerated electrons in the TiS_3 channel and further suppress Al metal filaments' oxidization. Therefore, the high resistive state (HRS) current was larger than that observed without light irradiation, and this state will be more difficult to change. Utilizing this phenomenon, the 400 nm optical signal was applied as the food stimulus (US), and the electric signal served as the ring stimulus (CS). When two stimulations were applied together, the current would exceed the threshold and have saliva secretion. Then, only electronic pulses also could induce salivation, which successfully realize associative learning based on low-dimensional optoelectronic memristors.[215]

VII. OUTLOOK

In summary, the emergence of optoelectronic artificial synapses and optoelectronic memristors based on low-dimensional nanomaterials presents a groundbreaking avenue for neuromorphic computing and artificial visual systems. The Von Neumann architecture has been the backbone of modern computing systems for decades. However, as the demand for ultrahigh speed and efficient computing continues to rise, its limitations are becoming increasingly pronounced. To overcome the limitations of traditional architecture, neuromorphic computing, drawing inspiration from the human brain's architecture becomes the foundation for developing next-generation computing and memory devices. This review focuses on different dimensions of materials, working mechanisms of neuromorphic and optoelectronic storage devices, diverse device structure designs, and applications of optoelectronic artificial synapses in visual sensor systems. In the era of the explosive development of artificial intelligence algorithms, the hardware compatible with them is believed to achieve great success shortly.

Meanwhile, vision and optical signals, as essential ways of information acquisition and carriers, have important application prospects in AI and biomimetic fields. Compared with electronic signals, light signals can carry a vast amount of information simultaneously, transmitting large data streams at extremely high speeds. Moreover, less energy, low attenuation, and low interference during signal transmission and calculation processes are also advantages of using light signals. Therefore, low-dimensional materials with unique photoelectric properties are one of the best choices for optoelectronic artificial

synapses and memristors. Nevertheless, the development of this field has not been smooth sailing, and it still faces many problems, including large-scale integration, the complex design for functional layers, and device uniformity. Based on the current preparation methods, more and more high-quality, wafer-level large-area 2D materials are synthesized and grown. Template and contact printing methods also provide ideas for large-scale integration of 1D materials.

At present, own to the advantages in large-scale preparation, device integration, and commercial value, the manufacturability of the 2D devices and their reliability are receiving more attention. In general, a complete device preparation process includes (1) material selection, (2) material growth, (3) device preparation, and (4) performance characterization. In the selection of materials, the good air stability should be prioritized because some 2D materials are susceptible to environmental factors like moisture, oxygen, and temperature. At present, many 2D materials with special properties (magnetism, ferroelectricity, etc.) and excellent air stability have been successfully synthesized.[270,271] However, other 2D materials like black phosphorus, which has the excellent optoelectronic properties but poor air stability, also can be selected by introducing encapsulation materials or building air-stable heterojunctions. During the material growth process, although a number of different methods are used to prepare 2D materials, including CVD, mechanical exfoliation, LPE, MBE, and so on, CVD is still the most promising method because of the balance among material quality, large-scale integration, and economy. In order to promote commercialization and chipization, integration and editability are important features for materials synthesis. Under this circumstance, substrate engineering is the key to achieving uniform nucleation and high-quality film. Sapphire or SiO_2 substrates were commonly used in previous studies, but it is difficult to control the uniformity of large-area fabrication because of the poor catalytic activities. Meanwhile, the metal substrates can assist the nucleation of 2D materials but noncompatible with the subsequent chip fabrication. Therefore, a variety of methods, including introducing an atomic-level substrate passivation layer, optimizing the release process of the precursor, and a more stable large-area transfer method, were developed to solve the challenges. Up to now, many research groups have successfully used CVD to grow large-area, even wafer-scale, high-quality two-dimensional materials and applied into the optoelectronic artificial synapses and memristors.[223,272] For device fabrication, in order to pursue the excellent and special photoelectric properties, mechanical exfoliation as a simple fabrication method combined with the transfer process is widely used to construct various heterojunctions and special device structures. However, this method is definitely a waste of manpower in large-area integration. The LPE and MBE could fabricate large-area film, but the uniformity of the former is difficult to guarantee, and the latter requires a high vacuum environment and a specific substrate. Therefore, the CVD is still the most promising way to grow large-area high-quality 2D film. Following with photolithography process or top gate process, large-area arrays of high-performance devices can be fabricated with better consistency and standardization.

For the part of device performance, it is believed that stability and reliability are the priority factors we need to be concerned. Furthermore, (1) the robustness of the device is mainly divided into material stability and device structure stability. As mentioned above, the stability of the material depends on the type of material and the synthesis process. Appropriate growth processes can reduce the generation of impurities, lattice distortion, and dislocations, and produce higher-quality single-crystal materials. Moreover, for 2D materials, there are many materials with excellent air stability that are used in the preparation of optoelectronic artificial synapses and memristors. For the device structure, some passivation layers or encapsulation layers are introduced into the device to isolate the effect of air on the channel material, and in general, devices prepared on rigid substrates tend to have more stable performance due to smaller interfacial tension. After ensuring stable performance, optimizing the main performance of the devices could be considered. Optoelectronic memristors, which are devices that change the resistance based on the history of applied voltage and light, have shown promise in neuromorphic computing and brain-inspired computing applications due to their nonvolatile and tunable resistance properties. (2) The switching speed of optoelectronic memristors to match the ultrafast synaptic processes in the human brain is a challenging yet intriguing goal. Overall, to achieve faster switching speeds using 2D nanomaterials, several strategies can be applied. First, 2D materials with high carrier mobility and photoresponsivity should be selected, such as graphene or TMDs. Then, scaling down and reducing the contact resistance of the devices also can effectively improve the switching speed. The former can shorten the distance that charges need to travel and the later can reduce carrier scattering and improve transmission efficiency.[273] Among them, the clean and van der Waals contact interface between metal and 2D materials shows the great potential in improving device performance. The last but not least, introducing phase change materials is attractive to replace the filamentary mechanism because of the faster switching speed than ion migration.[274] The other performance of synaptic devices, especially those used in neuromorphic and memristor-based systems, is essential for assessing the ability for mimic the behavior of biological synapses. In general, high-quality single crystal 2D materials are the basis for obtaining high-performance devices. (3) Achieving the desired nonlinear and plastic behavior observed in biological synapses using 2D nanomaterials is a challenging but promising avenue for emulating synaptic plasticity in neuromorphic systems. Therefore, it is effective methods to obtain better nonlinearity and plasticity by selecting and synthesizing high-quality 2D materials, controlling the thickness of the 2D materials, building effective van der Waals contacts (metal–semiconductor, semiconductor–dielectric layer, and semiconductor–semiconductor), and modifying the 2D nanomaterials through chemical doping or functionalization to tailor the electronic properties. Neuromorphic systems aim to replicate the energy-efficient computation of biological brains. Synaptic devices are a fundamental component of these systems, and low-power consumption is critical to achieving energy efficiency similar to the brain's synaptic plasticity. (4) Synaptic devices are a fundamental component of these systems, and low-power consumption is critical to achieving energy efficiency similar to the brain's synaptic plasticity. In order to be comparable with the biological synapses (≈10 fJ per activity), the synaptic devices based on 2D materials could be optimized through improving on/off ratio and reducing operating voltage and off-state current. The most effective way is to reduce the thickness of 2D materials, use high-k insulation layers and improve material quality. (5) These are also the effective ways to improve the signal-to-noise ratio. It is noted that the impact of the thickness of 2D materials on optical and electrical properties needs to be balanced for optoelectronic artificial synapses and memristors. (6) More importantly, in order to realize the function of sense-

memory-computing integrated for breaking through the limitations of traditional computing architectures and taking into account the ability for large-scale integration, some low-dimensional materials, especially for 2D materials with special crystal structures, are gradually being paid attention to and applied. For example, 2D materials with light polarization, ferroelectric and magnetic performance, etc., could be adopted to fabricate the sense-memory-computing integrated optoelectronic artificial synapses and memristors. At the same time, because of the physical properties brought about by the crystal structure of the materials themselves, the materials can realize the perception, storage, and processing of information in more dimensions. Therefore, the complex functional layers design can also be simplified to the greatest extent, and the uniformity and stability of the devices can be guaranteed as much as possible.

Therefore, a future outlook highlights critical considerations and obstacles in achieving human-like dynamic perception with artificial visual systems and memristors. Combining the many properties of low-dimensional materials with evolving synthetic and assembly methods, it is believed that the further development of artificial intelligence in various practical fields will thrive.

ACKNOWLEDGMENTS

We acknowledge a fellowship award from the Research Grants Council of Hong Kong SAR, China (CityU RFS2021-1S04).

AUTHOR DECLARATIONS

Conflict of Interest

The authors have no conflicts to disclose.

Author Contributions

Pengshan Xie: Conceptualization (lead); Writing – original draft (lead); Writing – review & editing (supporting). **Dengji Li:** Conceptualization (supporting); Writing – original draft (supporting); Writing – review & editing (supporting). **SenPo Yip:** Conceptualization (supporting); Writing – original draft (supporting); Writing – review & editing (supporting). **Johnny C. Ho:** Funding acquisition (lead); Supervision (lead); Writing – original draft (supporting); Writing – review & editing (lead).

DATA AVAILABILITY

Data sharing is not applicable to this article as no new data were created or analyzed in this study.

REFERENCES

[1]W. Zhang, B. Gao, J. Tang, P. Yao, S. Yu, M.-F. Chang, H.-J. Yoo, H. Qian, and H. Wu, Nat. Electron. **3**, 371–382 (2020).
[2]T. Venkatesan and S. Williams, Appl. Phys. Rev. **9**, 010401 (2022).
[3]K. Roy, A. Jaiswal, and P. Panda, Nature **575**, 607–617 (2019).
[4]Y. Zhai, P. Xie, J. Hu, X. Chen, Z. Feng, Z. Lv, G. Ding, K. Zhou, Y. Zhou, and S.-T. Han, Appl. Phys. Rev. **10**, 011408 (2023).
[5]Q. Zhang, T. Jin, X. Ye, D. Geng, W. Chen, and W. Hu, Adv. Funct. Mater. **31**, 2106151 (2021).
[6]H. Bian, Y. Y. Goh, Y. Liu, H. Ling, L. Xie, and X. Liu, Adv. Mater. **33**, 2006469 (2021).
[7]S.-J. Liang, Y. Li, B. Cheng, and F. Miao, Small Struct. **3**, 2200064 (2022).
[8]Y. H. Jung, B. Park, J. U. Kim, and T.-i. Kim, Adv. Mater. **31**, 1803637 (2019).
[9]S. W. Cho, C. Jo, Y.-H. Kim, and S. K. Park, Nano-Micro Lett. **14**, 203 (2022).
[10]D. Das, Y. Cen, J. Wang, and X. Fong, Phys. Rev. Appl. **19**, 024063 (2023).
[11]K. C. Kwon, J. H. Baek, K. Hong, S. Y. Kim, and H. W. Jang, Nano-Micro Lett. **14**, 58 (2022).
[12]X. Guan, Z. Lei, X. Yu, C.-H. Lin, J.-K. Huang, C.-Y. Huang, L. Hu, F. Li, A. Vinu, J. Yi, and T. Wu, Small **18**, 2203311 (2022).
[13]F. Huang, F. Fang, Y. Zheng, Q. You, H. Li, S. Fang, X. Cong, K. Jiang, Y. Wang, C. Han, W. Chen, and Y. Shi, Nano Res. **16**, 1304–1312 (2023).
[14]X. Wang, Y. Zong, D. Liu, J. Yang, and Z. Wei, Adv. Funct. Mater. **33**, 2213894 (2023).
[15]P. Robin, T. Emmerich, A. Ismail, A. Niguès, Y. You, G. H. Nam, A. Keerthi, A. Siria, A. K. Geim, B. Radha, and L. Bocquet, Science **379**, 161–167 (2019).
[16]G. Lee, J.-H. Baek, F. Ren, S. J. Pearton, G.-H. Lee, and J. Kim, Small **17**, 2100640 (2021).
[17]Y. Sun, Y. Ding, and D. Xie, Adv. Funct. Mater. **31**, 2105625 (2021).
[18]C. Shen, X. Gao, C. Chen, S. Ren, J.-L. Xu, Y.-D. Xia, and S.-D. Wang, Nanotechnology **33**, 065205 (2022).
[19]X. Chen, B. Chen, B. Jiang, T. Gao, G. Shang, S.-T. Han, C.-C. Kuo, V. A. L. Roy, and Y. Zhou, Adv. Funct. Mater. **33**, 2208807 (2023).
[20]D. Dupont, M. D. Tessier, P. F. Smet, and Z. Hens, Adv. Mater. **29**, 1700686 (2017).
[21]C. Wang, S. Y. Ke, J. Yang, W. D. Hu, F. Qiu, R. F. Wang, and Y. Yang, Nanotechnology **26**, 105201 (2015).
[22]K. T. Early and D. J. Nesbitt, Nano Lett. **15**, 7781–7787 (2015).
[23]C. Cheng, Q. Liang, M. Yan, Z. Liu, Q. He, T. Wu, S. Luo, Y. Pan, C. Zhao, and Y. Liu, J. Hazard. Mater. **424**, 127721 (2022).
[24]J. Fang, Z. Zhou, M. Xiao, Z. Lou, Z. Wei, and G. Shen, InfoMat **2**, 291–317 (2020).
[25]S. S. Periyal, M. Jagadeeswararao, S. E. Ng, R. A. John, and N. Mathews, Adv. Mater. Technol. **5**, 2000514 (2020).
[26]D. Hao, J. Zhang, S. Dai, J. Zhang, and J. Huang, ACS Appl. Mater. Interfaces **12**, 39487–39495 (2020).
[27]C. Han, X. Han, J. Han, M. He, S. Peng, C. Zhang, X. Liu, J. Gou, and J. Wang, Adv. Funct. Mater. **32**, 2113053 (2022).
[28]J. Kuang, K. Liu, M. Liu, M. Shao, M. Zhu, G. Liu, W. Wen, J. Chen, M. Qin, Z. Pan, Z. Zhao, Y. Liu, and Y. Guo, Adv. Funct. Mater. **33**, 2209502 (2023).
[29]X. Wu, E. Li, Y. Liu, W. Lin, R. Yu, G. Chen, Y. Hu, H. Chen, and T. Guo, Nano Energy **85**, 106000 (2021).
[30]Q.-B. Zhu, B. Li, D.-D. Yang, C. Liu, S. Feng, M.-L. Chen, Y. Sun, Y.-N. Tian, X. Su, X.-M. Wang, S. Qiu, Q.-W. Li, X.-M. Li, H.-B. Zeng, H.-M. Cheng, and D.-M. Sun, Nat. Commun. **12**, 1798 (2021).
[31]Y. Sun, Y. Ding, D. Xie, J. Xu, M. Sun, P. Yang, and Y. Zhang, Adv. Opt. Mater. **9**, 2002232 (2021).
[32]C. Jo, J. Kim, J. Y. Kwak, S. M. Kwon, J. B. Park, J. Kim, G.-S. Park, M.-G. Kim, Y.-H. Kim, and S. K. Park, Adv. Mater. **34**, 2108979 (2022).
[33]Y. Li, J. Wang, Q. Yang, and G. Shen, Adv. Sci. **9**, 2202123 (2022).
[34]K. Zhao, L. Zhang, R. Xia, Y. Dong, W. Xu, C. Niu, L. He, M. Yan, L. Qu, and L. Mai, Small **12**, 588–594 (2016).
[35]W. Meng, X. Zhou, Z. Qiu, C. Liu, J. Chen, W. Yue, M. Wang, and H. Bi, Carbon **96**, 532–540 (2016).
[36]M. Chen, Y. Zou, L. Wu, Q. Pan, D. Yang, H. Hu, Y. Tan, Q. Zhong, Y. Xu, H. Liu, B. Sun, and Q. Zhang, Adv. Funct. Mater. **27**, 1701121 (2017).
[37]Y. Gao, O. Roslyak, E. Dervishi, N. S. Karan, Y. Ghosh, C. J. Sheehan, F. Wang, G. Gupta, A. Mohite, A. M. Dattelbaum, S. K. Doorn, J. A. Hollingsworth, A. Piryatinski, and H. Htoon, Adv. Opt. Mater. **3**, 39–43 (2015).
[38]T. Chtouki, M. El Mrabet, A. Tarbi, I. Goncharova, and H. Erguig, Opt. Mater. **118**, 111294 (2021).
[39]S.-H. Hwang, S.-Y. Kang, S. Yang, J. Lee, and T.-L. Choi, J. Am. Chem. Soc. **144**, 5921–5929 (2022).
[40]Z. Wang, R. Luo, I. Johnson, H. Kashani, and M. Chen, ACS Nano **14**, 899–906 (2020).
[41]D. Liu, X. Chen, Y. Hu, T. Sun, Z. Song, Y. Zheng, Y. Cao, Z. Cai, M. Cao, L. Peng, Y. Huang, L. Du, W. Yang, G. Chen, D. Wei, A. T. S. Wee, and D. Wei, Nat. Commun. **9**, 193 (2018).
[42]J. Etzkorn, H. A. Therese, F. Rocker, N. Zink, U. Kolb, and W. Tremel, Adv. Mater. **17**, 2372–2375 (2005).

[43]J. Chen, W. Du, J. Shi, M. Li, Y. Wang, Q. Zhang, and X. Liu, InfoMat **2**, 170–183 (2020).
[44]X. Li, Y. Wu, S. Zhang, B. Cai, Y. Gu, J. Song, and H. Zeng, Adv. Funct. Mater. **26**, 2435–2445 (2016).
[45]Q. Pan, H. Hu, Y. Zou, M. Chen, L. Wu, D. Yang, X. Yuan, J. Fan, B. Sun, and Q. Zhang, J. Mater. Chem. C **5**, 10947–10954 (2017).
[46]Y. Tong, E. Bladt, M. F. Aygüler, A. Manzi, K. Z. Milowska, V. A. Hintermayr, P. Docampo, S. Bals, A. S. Urban, L. Polavarapu, and J. Feldmann, Angew. Chem., Int. Ed. **55**, 13887–13892 (2016).
[47]L. Wu, H. Hu, Y. Xu, S. Jiang, M. Chen, Q. Zhong, D. Yang, Q. Liu, Y. Zhao, B. Sun, Q. Zhang, and Y. Yin, Nano Lett. **17**, 5799–5804 (2017).
[48]J. Pei, X. Wu, W.-J. Liu, D. W. Zhang, and S.-J. Ding, ACS Nano **16**, 2442–2451 (2022).
[49]R. Kumar, N. Goel, D. K. Jarwal, Y. Hu, J. Zhang, and M. Kumar, J. Mater. Chem. C **11**, 774–801 (2023).
[50]Q. Ou, B. Yang, J. Zhang, D. Liu, T. Chen, X. Wang, D. Hao, Y. Lu, and J. Huang, Small **17**, 2007241 (2021).
[51]Y. Zhang, J. Wu, M. Aagesen, and H. Liu, J. Phys. D: Appl. Phys. **48**, 463001 (2015).
[52]Y. Ni, S. Zhang, L. Sun, L. Liu, H. Wei, Z. Xu, W. Xu, and W. Xu, Appl. Mater. Today **25**, 101223 (2021).
[53]D. Zheng, H. Fang, M. Long, F. Wu, P. Wang, F. Gong, X. Wu, J. C. Ho, L. Liao, and W. Hu, ACS Nano **12**, 7239–7245 (2018).
[54]J. Michel, J. Liu, and L. C. Kimerling, Nat. Photonics **4**, 527–534 (2010).
[55]F. Li, Y. Meng, R. Dong, S. Yip, C. Lan, X. Kang, F. Wang, K. S. Chan, and J. C. Ho, ACS Nano **13**, 12042–12051 (2019).
[56]M. Peng, R. Xie, Z. Wang, P. Wang, F. Wang, H. Ge, Y. Wang, F. Zhong, P. Wu, J. Ye, Q. Li, L. Zhang, X. Ge, Y. Ye, Y. Lei, W. Jiang, Z. Hu, F. Wu, X. Zhou, J. Miao, J. Wang, H. Yan, C. Shan, J. Dai, C. Chen, X. Chen, W. Lu, and W. Hu, Sci. Adv. **7**, eabf7358 (2021).
[57]F. Sun, Q. Lu, L. Liu, L. Li, Y. Wang, M. Hao, Z. Cao, Z. Wang, S. Wang, T. Li, and T. Zhang, Adv. Mater. Technol. **5**, 1900888 (2020).
[58]D. Li, C. Lan, A. Manikandan, S. Yip, Z. Zhou, X. Liang, L. Shu, Y.-L. Chueh, N. Han, and J. C. Ho, Nat. Commun. **10**, 1664 (2019).
[59]J. Hao, Y.-H. Kim, S. N. Habisreutinger, S. P. Harvey, E. M. Miller, S. M. Foradori, M. S. Arnold, Z. Song, Y. Yan, J. M. Luther, and J. L. Blackburn, Sci. Adv. **7**, eabf1959 (2021).
[60]L. Shao, M. Li, P. Wu, F. Wang, S. Chen, W. Hu, H. Wang, Z. Cui, and J. Zhao, J. Mater. Chem. C **8**, 6914–6922 (2020).
[61]P. Xie, X. Chen, Z. Zeng, W. Wang, Y. Meng, Z. Lai, Q. Quan, D. Li, W. Wang, X. Bu, S.-W. Tsang, S. Yip, J. Sun, and J. C. Ho, Adv. Funct. Mater. **33**, 2209091 (2023).
[62]G. Hu, H. An, J. Xi, J. Lu, Q. Hua, and Z. Peng, Nano Energy **89**, 106282 (2021).
[63]Z.-x. Yang, N. Han, M. Fang, H. Lin, H.-Y. Cheung, S. Yip, E.-J. Wang, T. Hung, C.-Y. Wong, and J. C. Ho, Nat. Commun. **5**, 5249 (2014).
[64]Y.-Z. Long, M. Yu, B. Sun, C.-Z. Gu, and Z. Fan, Chem. Soc. Rev. **41**, 4560–4580 (2012).
[65]Y. Zhu, V. Raj, Z. Li, H. H. Tan, C. Jagadish, and L. Fu, Adv. Mater. **33**, 2105729 (2021).
[66]E. Sutter, J. S. French, S. Sutter, J. C. Idrobo, and P. Sutter, ACS Nano **14**, 6117–6126 (2020).
[67]I. Udom, M. K. Ram, E. K. Stefanakos, A. F. Hepp, and D. Y. Goswami, Mater. Sci. Semicond. Process. **16**, 2070–2083 (2013).
[68]Y.-Z. Chen, T.-H. Liu, C.-Y. Chen, C.-H. Liu, S.-Y. Chen, W.-W. Wu, Z. L. Wang, J.-H. He, Y.-H. Chu, and Y.-L. Chueh, ACS Nano **6**, 2826–2832 (2012).
[69]R. Calarco, R. J. Meijers, R. K. Debnath, T. Stoica, E. Sutter, and H. Lüth, Nano Lett. **7**, 2248–2251 (2007).
[70]X. Tang, S. Zhou, and X. Yuan, Mater. Lett. **93**, 25–27 (2013).
[71]M. Longo, R. Fallica, C. Wiemer, O. Salicio, M. Fanciulli, E. Rotunno, and L. Lazzarini, Nano Lett. **12**, 1509–1515 (2012).
[72]F. Xu, B. Xue, F. Wang, and A. Dong, Chem. Mater. **27**, 1140–1146 (2015).
[73]L. Gu, S. Poddar, Y. Lin, Z. Long, D. Zhang, Q. Zhang, L. Shu, X. Qiu, M. Kam, A. Javey, and Z. Fan, Nature **581**, 278–282 (2020).
[74]J. Luo, Z. Zheng, S. Yan, M. Morgan, X. Zu, X. Xiang, and W. Zhou, ACS Photonics **7**, 1461–1467 (2020).
[75]Y. Meng, Y. Zhang, Z. Lai, W. Wang, W. Wang, Y. Li, D. Li, P. Xie, D. Yin, D. Chen, C. Liu, S. Yip, and J. C. Ho, Nano Lett. **23**, 812–819 (2023).
[76]Y. Meng, C. Lan, F. Li, S. Yip, R. Wei, X. Kang, X. Bu, R. Dong, H. Zhang, and J. C. Ho, ACS Nano **13**, 6060–6070 (2019).
[77]D. Li, S. Yip, F. Li, H. Zhang, Y. Meng, X. Bu, X. Kang, C. Lan, C. Liu, and J. C. Ho, Adv. Opt. Mater. **8**, 2001201 (2020).
[78]Z.-x. Yang, L. Liu, S. Yip, D. Li, L. Shen, Z. Zhou, N. Han, T. F. Hung, E. Y.-B. Pun, X. Wu, A. Song, and J. C. Ho, ACS Nano **11**, 4237–4246 (2017).
[79]J. J. Hou, N. Han, F. Wang, F. Xiu, S. Yip, A. T. Hui, T. Hung, and J. C. Ho, ACS Nano **6**, 3624–3630 (2012).
[80]S. Ahmad, Y. Liao, A. Hussain, Q. Zhang, E.-X. Ding, H. Jiang, and E. I. Kauppinen, Carbon **149**, 318–327 (2019).
[81]A. A. Murthy, Y. Li, E. Palacios, Q. Li, S. Hao, J. G. DiStefano, C. Wolverton, K. Aydin, X. Chen, and V. P. Dravid, ACS Appl. Mater. Interfaces **10**, 6799–6804 (2018).
[82]L. Maduro, M. Noordam, M. Bolhuis, L. Kuipers, and S. Conesa-Boj, Adv. Funct. Mater. **32**, 2107880 (2022).
[83]D. Ren, K. M. Azizur-Rahman, Z. Rong, B.-C. Juang, S. Somasundaram, M. Shahili, A. C. Farrell, B. S. Williams, and D. L. Huffaker, Nano. Lett. **19**, 2793–2802 (2019).
[84]I. Yang, Z. Li, J. Wong-Leung, Y. Zhu, Z. Li, N. Gagrani, L. Li, M. N. Lockrey, H. Nguyen, Y. Lu, H. H. Tan, C. Jagadish, and L. Fu, Nano Lett. **19**, 3821–3829 (2019).
[85]C. B. Maliakkal, D. Jacobsson, M. Tornberg, A. R. Persson, J. Johansson, R. Wallenberg, and K. A. Dick, Nat. Commun. **10**, 4577 (2019).
[86]P. Schroth, M. Al Humaidi, L. Feigl, J. Jakob, A. Al Hassan, A. Davtyan, H. Küpers, A. Tahraoui, L. Geelhaar, U. Pietsch, and T. Baumbach, Nano Lett. **19**, 4263–4271 (2019).
[87]Y. Yang, X. Wang, C. Wang, Y. Song, M. Zhang, Z. Xue, S. Wang, Z. Zhu, G. Liu, P. Li, L. Dong, Y. Mei, P. K. Chu, W. Hu, J. Wang, and Z. Di, Nano Lett. **20**, 3872–3879 (2020).
[88]L. Li, D. Pan, Y. Xue, X. Wang, M. Lin, D. Su, Q. Zhang, X. Yu, H. So, D. Wei, B. Sun, P. Tan, A. Pan, and J. Zhao, Nano Lett. **17**, 622–630 (2017).
[89]V. G. Dubrovskii, W. Kim, V. Piazza, L. Güniat, and A. Fontcuberta i Morral, Nano Lett. **21**(7), 3139–3145 (2021).
[90]V. V. Zalamai, V. V. Ursaki, E. V. Rusu, P. Arabadji, I. M. Tiginyanu, and L. Sirbu, Appl. Phys. Lett. **84**, 5168–5170 (2004).
[91]S.-Y. Min, T.-S. Kim, Y. Lee, H. Cho, W. Xu, and T.-W. Lee, Small **11**, 45–62 (2015).
[92]J. H. Oh, H. W. Lee, S. Mannsfeld, R. M. Stoltenberg, E. Jung, Y. W. Jin, J. M. Kim, J.-B. Yoo, and Z. Bao, Proc. Natl. Acad. Sci. U. S. A. **106**, 6065–6070 (2009).
[93]L. Qiu, W. H. Lee, X. Wang, J. S. Kim, J. A. Lim, D. Kwak, S. Lee, and K. Cho, Adv. Mater. **21**, 1349–1353 (2009).
[94]Y. Shi, M. Wang, C. Hong, Z. Yang, J. Deng, X. Song, L. Wang, J. Shao, H. Liu, and Y. Ding, Sens. Actuators B: Chem. **177**, 1027–1034 (2013).
[95]M. M. Islam, D. Dev, A. Krishnaprasad, L. Tetard, and T. Roy, Sci. Rep. **10**, 21870 (2020).
[96]S. Wang, C. Chen, Z. Yu, Y. He, X. Chen, Q. Wan, Y. Shi, D. W. Zhang, H. Zhou, X. Wang, and P. Zhou, Adv. Mater. **31**, 1806227 (2019).
[97]H.-S. Zhang, X.-M. Dong, Z.-C. Zhang, Z.-P. Zhang, C.-Y. Ban, Z. Zhou, C. Song, S.-Q. Yan, Q. Xin, J.-Q. Liu, Y.-X. Li, and W. Huang, Nat. Commun. **13**, 4996 (2022).
[98]F. Guo, M. Song, M.-C. Wong, R. Ding, W. F. Io, S.-Y. Pang, W. Jie, and J. Hao, Adv. Funct. Mater. **32**, 2108014 (2022).
[99]M. M. Islam, A. Krishnaprasad, D. Dev, R. Martinez-Martinez, V. Okonkwo, B. Wu, S. S. Han, T.-S. Bae, H.-S. Chung, J. Touma, Y. Jung, and T. Roy, ACS Nano **16**, 10188–10198 (2022).
[100]Q. Zhang, X. Ye, Y. Zheng, Y. Wang, L. Li, Z. Gao, J. Wu, H. Dong, D. Geng, and W. Hu, J. Mater. Chem. C **10**, 2681–2689 (2022).
[101]L. Zhang, X. Tian, J. Yao, X. Song, S. Yang, S. Guo, Y. Wang, B. Li, X. Ren, Y. Sun, F. Yang, R. Li, and W. Hu, J. Mater. Chem. C **9**, 8834–8841 (2021).
[102]Y. Wu, D. Li, C.-L. Wu, H. Y. Hwang, and Y. Cui, Nat. Rev. Mater. **8**, 41–53 (2023).
[103]Y. Meng, J. Feng, S. Han, Z. Xu, W. Mao, T. Zhang, J. S. Kim, I. Roh, Y. Zhao, D.-H. Kim, Y. Yang, J.-W. Lee, L. Yang, C.-W. Qiu, and S.-H. Bae, Nat. Rev. Mater. **8**, 498–517 (2023).

[104]J.-y. Kim, X. Ju, K.-W. Ang, and D. Chi, ACS Nano **17**, 1831–1844 (2023).
[105]Z. Zhang, X. Yang, K. Liu, and R. Wang, Adv. Sci. **9**, 2105201 (2022).
[106]J. Dong, L. Zhang, X. Dai, and F. Ding, Nat. Commun. **11**, 5862 (2020).
[107]X. Zhang, T. H. Choudhury, M. Chubarov, Y. Xiang, B. Jariwala, F. Zhang, N. Alem, G.-C. Wang, J. A. Robinson, and J. M. Redwing, Nano Lett. **18**, 1049–1056 (2018).
[108]W. Wang, Y. Meng, Y. Zhang, Z. Zhang, W. Wang, Z. Lai, P. Xie, D. Li, D. Chen, Q. Quan, D. Yin, C. Liu, Z. Yang, S. Yip, and J. C. Ho, Adv. Mater. **35**, 2210854 (2023).
[109]Y. Shi, W. Zhou, A.-Y. Lu, W. Fang, Y.-H. Lee, A. L. Hsu, S. M. Kim, K. K. Kim, H. Y. Yang, L.-J. Li, J.-C. Idrobo, and J. Kong, Nano Lett. **12**, 2784–2791 (2012).
[110]T. Yang, B. Zheng, Z. Wang, T. Xu, C. Pan, J. Zou, X. Zhang, Z. Qi, H. Liu, Y. Feng, W. Hu, F. Miao, L. Sun, X. Duan, and A. Pan, Nat. Commun. **8**, 1906 (2017).
[111]R. Wu, Q. Tao, J. Li, W. Li, Y. Chen, Z. Lu, Z. Shu, B. Zhao, H. Ma, Z. Zhang, X. Yang, B. Li, H. Duan, L. Liao, Y. Liu, X. Duan, and X. Duan, Nat. Electron. **5**, 497–504 (2022).
[112]X. Zhang, X. Liu, C. Zhang, S. Peng, H. Zhou, L. He, J. Gou, X. Wang, and J. Wang, ACS Nano **16**(3), 4851–4860 (2022).
[113]H. Wang, S. Jiang, Z. Hao, X. Xu, M. Pei, J. Guo, Q. Wang, Y. Li, J. Chen, J. Xu, X. Wang, J. Wang, Y. Shi, and Y. Li, J. Phys. Chem. Lett. **13**, 2338–2347 (2022).
[114]Y. Liu, Y. Wei, M. Liu, Y. Bai, G. Liu, X. Wang, S. Shang, W. Gao, C. Du, J. Chen, and Y. Liu, Angew. Chem., Int. Ed. Engl. **60**, 17440–17445 (2021).
[115]Y. Chen, Y. Sun, J. Peng, J. Tang, K. Zheng, and Z. Liang, Adv. Mater. **30**, 1703487 (2018).
[116]Y. Sun, L. Qian, D. Xie, Y. Lin, M. Sun, W. Li, L. Ding, T. Ren, and T. Palacios, Adv. Funct. Mater. **29**, 1902538 (2019).
[117]C.-K. Liu, V. Piradi, J. Song, Z. Wang, L.-W. Wong, E.-H.-L. Tan, J. Zhao, X. Zhu, and F. Yan, Adv. Mater. **34**, 2204140 (2022).
[118]S. W. Cho, S. M. Kwon, Y.-H. Kim, and S. K. Park, Adv. Intell. Syst. **3**, 2000162 (2021).
[119]Q. Zhang, H. Yu, M. Barbiero, B. Wang, and M. Gu, Light: Sci. Appl. **8**, 42 (2019).
[120]H. Li, X. Jiang, W. Ye, H. Zhang, L. Zhou, F. Zhang, D. She, Y. Zhou, and S.-T. Han, Nano Energy **65**, 104000 (2019).
[121]Y. Mizuno, Y. Ito, and K. Ueda, Carbon **182**, 669–676 (2021).
[122]P. Lei, H. Duan, L. Qin, X. Wei, R. Tao, Z. Wang, F. Guo, M. Song, W. Jie, and J. Hao, Adv. Funct. Mater. **32**, 2201276 (2022).
[123]Q. Liu, S. Gao, L. Xu, W. Yue, C. Zhang, H. Kan, Y. Li, and G. Shen, Chem. Soc. Rev. **51**, 3341–3379 (2022).
[124]Y. Ren, X. Bu, M. Wang, Y. Gong, J. Wang, Y. Yang, G. Li, M. Zhang, Y. Zhou, and S.-T. Han, Nat. Commun. **13**, 5585 (2022).
[125]Y. Wang, Y. Gong, S. Huang, X. Xing, Z. Lv, J. Wang, J.-Q. Yang, G. Zhang, Y. Zhou, and S.-T. Han, Nat. Commun. **12**, 5979 (2021).
[126]J.-M. Yang, J.-H. Lee, Y.-K. Jung, S.-Y. Kim, J.-H. Kim, S.-G. Kim, J.-H. Kim, S. Seo, D.-A. Park, J.-W. Lee, A. Walsh, J.-H. Park, and N.-G. Park, Adv. Sci. **9**, 2200168 (2022).
[127]X. Feng, Y. Li, L. Wang, S. Chen, Z. G. Yu, W. C. Tan, N. Macadam, G. Hu, L. Huang, L. Chen, X. Gong, D. Chi, T. Hasan, A. V. Y. Thean, Y.-W. Zhang, and K.-W. Ang, Adv. Electron. Mater. **5**, 1900740 (2019).
[128]Y. Wang, J. Yang, Z. Wang, J. Chen, Q. Yang, Z. Lv, Y. Zhou, Y. Zhai, Z. Li, and S.-T. Han, Small **15**, 1805431 (2019).
[129]W. Wang, S. Gao, Y. Li, W. Yue, H. Kan, C. Zhang, Z. Lou, L. Wang, and G. Shen, Adv. Funct. Mater. **31**, 2101201 (2021).
[130]S. Kim, D. G. Roe, Y. Y. Choi, H. Woo, J. Park, J. I. Lee, Y. Choi, S. B. Jo, M. S. Kang, Y. J. Song, S. Jeong, and J. H. Cho, Sci. Adv. **7**, eabe3996 (2021).
[131]B. Pradhan, S. Das, J. Li, F. Chowdhury, J. Cherusseri, D. Pandey, D. Dev, A. Krishnaprasad, E. Barrios, A. Towers, A. Gesquiere, L. Tetard, T. Roy, and J. Thomas, Sci. Adv. **6**, eaay5225 (2020).
[132]Y. Hu, H. Yang, J. Huang, X. Zhang, B. Tan, H. Shang, S. Zhang, W. Feng, J. Zhu, J. Zhang, Y. Shuai, D. Jia, Y. Zhou, and P. Hu, ACS Appl. Mater. Interfaces **14**, 55839–55849 (2022).
[133]H. Han, H. Yu, H. Wei, J. Gong, and W. Xu, Small **15**, 1900695 (2019).
[134]T. Berzina, A. Smerieri, M. Bernabò, A. Pucci, G. Ruggeri, V. Erokhin, and M. P. Fontana, J. Appl. Phys. **105**, 124515 (2009).
[135]J. Jiang, J. Guo, X. Wan, Y. Yang, H. Xie, D. Niu, J. Yang, J. He, Y. Gao, and Q. Wan, Small **13**, 1700933 (2017).
[136]D. Xie, W. Hu, and J. Jiang, Org. Electron. **63**, 120–128 (2018).
[137]J. Sun, S. Oh, Y. Choi, S. Seo, M. J. Oh, M. Lee, W. B. Lee, P. J. Yoo, J. H. Cho, and J.-H. Park, Adv. Funct. Mater. **28**, 1804397 (2018).
[138]Y. Cheng, H. Li, B. Liu, L. Jiang, M. Liu, H. Huang, J. Yang, J. He, and J. Jiang, Small **16**, 2005217 (2020).
[139]B. Park, Y. Hwang, O. Kwon, S. Hwang, J. A. Lee, D.-H. Choi, S.-K. Lee, A. R. Kim, B. Cho, J.-D. Kwon, J. I. Lee, and Y. Kim, ACS Appl. Mater. Interfaces **14**, 53038–53047 (2022).
[140]R. Cao, X. Zhang, S. Liu, J. Lu, Y. Wang, H. Jiang, Y. Yang, Y. Sun, W. Wei, J. Wang, H. Xu, Q. Li, and Q. Liu, Nat. Commun. **13**, 7018 (2022).
[141]S. Lee, R. Peng, C. Wu, and M. Li, Nat. Commun. **13**, 1485 (2022).
[142]C. Gao, H. Yang, E. Li, Y. Yan, L. He, H. Chen, Z. Lin, and T. Guo, ACS Photonics **8**, 3094–3103 (2021).
[143]J. Zhang, D. Liu, Q. Ou, Y. Lu, and J. Huang, ACS Appl. Mater. Interfaces **14**, 11699–11707 (2022).
[144]C. Zhu, H. Liu, W. Wang, L. Xiang, J. Jiang, Q. Shuai, X. Yang, T. Zhang, B. Zheng, H. Wang, D. Li, and A. Pan, Light: Sci. Appl. **11**, 337 (2022).
[145]X. Wang, B. Wang, Q. Zhang, Y. Sun, E. Wang, H. Luo, Y. Wu, L. Gu, H. Li, and K. Liu, Adv. Mater. **33**, 2102435 (2021).
[146]M. Zhang, Z. Chi, G. Wang, Z. Fan, H. Wu, P. Yang, J. Yang, P. Yan, and Z. Sun, Adv. Mater. **34**, 2205679 (2022).
[147]Q. Liu, L. Yin, C. Zhao, J. Wang, Z. Wu, H. Lei, Y. Liu, B. Tian, Z. Zhang, Z. Zhao, R. Liu, C. Ding, Y. Han, C.-Q. Ma, P. Song, I. Z. Mitrovic, E. G. Lim, and Z. Wen, Nano Energy **102**, 107686 (2022).
[148]K. Liang, R. Wang, B. Huo, H. Ren, D. Li, Y. Wang, Y. Tang, Y. Chen, C. Song, F. Li, B. Ji, H. Wang, and B. Zhu, ACS Nano **16**, 8651–8661 (2022).
[149]S.-G. Kim, S.-H. Kim, J. Park, G.-S. Kim, J.-H. Park, K. C. Saraswat, J. Kim, and H.-Y. Yu, ACS Nano **13**, 10294–10300 (2019).
[150]Q. Wang, R. Jiang, Z. Gao, M. Deng, J. Chen, L. Zhu, L. Shang, Y. Li, D. Fuchs, J. Zhang, and Z. Hu, Appl. Surf. Sci. **613**, 156148 (2023).
[151]L. Fang, S. Dai, Y. Zhao, D. Liu, and J. Huang, Adv. Electron. Mater. **6**, 1901217 (2020).
[152]M. Li, Z. Xiong, S. Shao, L. Shao, S.-T. Han, H. Wang, and J. Zhao, Carbon **176**, 592–601 (2021).
[153]S. Oh, J.-J. Lee, S. Seo, G. Yoo, and J.-H. Park, npj 2D Mater. Appl. **5**, 95 (2021).
[154]N. Li, C. He, Q. Wang, J. Tang, Q. Zhang, C. Shen, J. Tang, H. Huang, S. Wang, J. Li, B. Huang, Z. Wei, Y. Guo, J. Yuan, W. Yang, R. Yang, D. Shi, and G. Zhang, Nano Res. **15**, 5418–5424 (2022).
[155]C.-Y. Wang, S.-J. Liang, S. Wang, P. Wang, Z. a. Li, Z. Wang, A. Gao, C. Pan, C. Liu, J. Liu, H. Yang, X. Liu, W. Song, C. Wang, B. Cheng, X. Wang, K. Chen, Z. Wang, K. Watanabe, T. Taniguchi, J. J. Yang, and F. Miao, Sci. Adv. **6**, eaba6173 (2020).
[156]H.-K. He, R. Yang, W. Zhou, H.-M. Huang, J. Xiong, L. Gan, T.-Y. Zhai, and X. Guo, Small **14**, 1800079 (2018).
[157]Y. Wang, F. Wang, S. Li, J. Yang, T. Yan, Y. Cai, Z. Wu, X. Zhan, J. He, and Z. Wang, Small **18**, 2204021 (2022).
[158]K.-C. Lee, M. Li, Y.-H. Chang, S.-H. Yang, C.-Y. Lin, Y.-M. Chang, F.-S. Yang, K. Watanabe, T. Taniguchi, C.-H. Ho, C.-H. Lien, S.-P. Lin, P.-W. Chiu, and Y.-F. Lin, Nano Energy **77**, 105258 (2020).
[159]Y. Hu, M. Dai, W. Feng, X. Zhang, S. Zhang, B. Tan, H. Shang, Y. Q. Fu, and P. Hu, Mater. Horiz. **7**, 3316–3324 (2020).
[160]Z. Luo, Y. Xie, Z. Li, Y. Wang, L. Li, Z. Luo, C. Zhu, X. Yang, M. Huang, J. Huang, D. Liang, X. Zhu, D. Li, and A. Pan, Nano Res. **15**, 3539–3547 (2022).
[161]Y. Wang, J. Yang, W. Ye, D. She, J. Chen, Z. Lv, V. A. L. Roy, H. Li, K. Zhou, Q. Yang, Y. Zhou, and S.-T. Han, Adv. Electron. Mater. **6**, 1900765 (2020).
[162]T. Ahmed, M. Tahir, M. X. Low, Y. Ren, S. A. Tawfik, E. L. H. Mayes, S. Kuriakose, S. Nawaz, M. J. S. Spencer, H. Chen, M. Bhaskaran, S. Sriram, and S. Walia, Adv. Mater. **33**, 2004207 (2021).
[163]T. Ahmed, S. Kuriakose, E. L. H. Mayes, R. Ramanathan, V. Bansal, M. Bhaskaran, S. Sriram, and S. Walia, Small **15**, 1900966 (2019).
[164]J. Liu, Z. Yang, Z. Gong, Z. Shen, Y. Ye, B. Yang, Y. Qiu, B. Ye, L. Xu, T. Guo, and S. Xu, ACS Appl. Mater. Interfaces **13**, 13362–13371 (2021).
[165]D. Hao, J. Zhang, L. Li, B. Yang, P. Guo, S. Zhang, and J. Huang, Nano Res. **15**, 5435–5442 (2022).

[166]Q. Shi, D. Liu, D. Hao, J. Zhang, L. Tian, L. Xiong, and J. Huang, Nano Energy **87**, 106197 (2021).
[167]L. Yin, W. Huang, R. Xiao, W. Peng, Y. Zhu, Y. Zhang, X. Pi, and D. Yang, Nano Lett. **20**, 3378–3387 (2020).
[168]Z. Xin, Y. Tan, T. Chen, E. Iranmanesh, L. Li, K.-C. Chang, S. Zhang, C. Liu, and H. Zhou, Nanoscale Adv. **3**, 5046–5052 (2021).
[169]J.-Y. Mao, L. Hu, S.-R. Zhang, Y. Ren, J.-Q. Yang, L. Zhou, Y.-J. Zeng, Y. Zhou, and S.-T. Han, J. Mater. Chem. C **7**, 48–59 (2019).
[170]S. Zhang, K. Guo, L. Sun, Y. Ni, L. Liu, W. Xu, L. Yang, and W. Xu, Adv. Mater. **33**, 2007350 (2021).
[171]D. Xie, G. Gao, B. Tian, Z. Shu, H. Duan, W.-W. Zhao, J. He, and J. Jiang, Adv. Mater. **35**, 2212118 (2023).
[172]X. Huang, Y. Liu, G. Liu, K. Liu, X. Wei, M. Zhu, W. Wen, Z. Zhao, Y. Guo, and Y. Liu, Adv. Funct. Mater. **33**, 2208836 (2023).
[173]X. Huang, Q. L. W. Shi, K. Liu, Y. Zhang, Y. Liu, X. Wei, Z. Zhao, Y. Guo, and Y. Liu, Small **17**, 2102820 (2021).
[174]Y. Wang, K. Wang, X. Hu, Y. Wang, W. Gao, Y. Zhang, Z. Liu, Y. Zheng, K. Xu, D. Yang, and X. Pi, ACS Nano **17**, 3696–3704 (2023).
[175]J.-Y. Chen, D.-L. Yang, F.-C. Jhuang, Y.-H. Fang, J.-S. Benas, F.-C. Liang, and C.-C. Kuo, Adv. Funct. Mater. **31**, 2105911 (2021).
[176]Y. Wang, Y. Zhu, Y. Li, Y. Zhang, D. Yang, and X. Pi, Adv. Funct. Mater. **32**, 2107973 (2022).
[177]Y. Ni, J. Feng, J. Liu, H. Yu, H. Wei, Y. Du, L. Liu, L. Sun, J. Zhou, and W. Xu, Adv. Sci. **9**, 2102036 (2022).
[178]Y. Sun, R. Hu, C. An, X. Ma, J. Zhang, and J. Liu, Nanotechnology **32**, 475206 (2021).
[179]Z. Hao, H. Wang, S. Jiang, J. Qian, X. Xu, Y. Li, M. Pei, B. Zhang, J. Guo, H. Zhao, J. Chen, Y. Tong, J. Wang, X. Wang, Y. Shi, and Y. Li, Adv. Sci. **9**, 2103494 (2022).
[180]Y. Wang, F. Wang, Z. Wang, J. Wang, J. Yang, Y. Yao, N. Li, M. G. Sendeku, X. Zhan, C. Shan, and J. He, Nano Res. **14**, 4328–4335 (2021).
[181]Y. Hu, M. Dai, W. Feng, X. Zhang, F. Gao, S. Zhang, B. Tan, J. Zhang, Y. Shuai, Y. Fu, and P. Hu, Adv. Mater. **33**, 2104960 (2021).
[182]Y. Zhang, L. Wang, Y. Lei, B. Wang, Y. Lu, Y. Yao, N. Zhang, D. Lin, Z. Jiang, H. Guo, J. Zhang, and H. Hu, ACS Nano **16**, 20937–20945 (2022).
[183]X. Wang, X. Zhou, A. Cui, M. Deng, X. Xu, L. Xu, Y. Ye, K. Jiang, L. Shang, L. Zhu, J. Zhang, Y. Li, Z. Hu, and J. Chu, Mater. Horiz. **8**, 1985–1997 (2021).
[184]C. Li, N. Ilyas, J. Wang, Y. Li, H. Luo, D. Li, D. Gu, F. Liu, Y. Jiang, and W. Li, Appl. Surf. Sci. **611**, 155682 (2023).
[185]H. Lian, Q. Liao, B. Yang, Y. Zhai, S.-T. Han, and Y. Zhou, J. Mater. Chem. C **9**, 640–648 (2021).
[186]L. Li, X.-L. Wang, J. Pei, W.-J. Liu, X. Wu, D. W. Zhang, and S.-J. Ding, Sci. China Mater. **64**, 1219–1229 (2021).
[187]D. Xie, L. Wei, Z. Wei, J. He, and J. Jiang, J. Mater. Chem. C **10**, 5249–5256 (2022).
[188]X. Zhang, E. Li, R. Yu, L. He, W. Yu, H. Chen, and T. Guo, Sci. China Mater. **65**, 1383–1390 (2022).
[189]B. Mukherjee, A. Zulkefli, K. Watanabe, T. Taniguchi, Y. Wakayama, and S. Nakaharai, Adv. Funct. Mater. **30**, 2001688 (2020).
[190]Y. Sun, M. Li, Y. Ding, H. Wang, H. Wang, Z. Chen, and D. Xie, InfoMat **4**, e12317 (2022).
[191]Y. X. Cao, C. Zhao, Z. J. Liu, X. P. Chen, I. Z. Mitrovic, Y. N. Liu, L. Yang, H. van Zalinge, and C. Z. Zhao, Solid-State Electron. **192**, 108257 (2022).
[192]T. Zhao, C. Zhao, W. Xu, Y. Liu, H. Gao, I. Z. Mitrovic, E. G. Lim, L. Yang, and C. Z. Zhao, Adv. Funct. Mater. **31**, 2106000 (2021).
[193]J. Zhang, Q. Shi, R. Wang, X. Zhang, L. Li, J. Zhang, L. Tian, L. Xiong, and J. Huang, InfoMat **3**, 904–916 (2021).
[194]H.-L. Park, H. Kim, D. Lim, H. Zhou, Y.-H. Kim, Y. Lee, S. Park, and T.-W. Lee, Adv. Mater. **32**, 1906899 (2020).
[195]J. Meng, T. Wang, Z. He, Q. Li, H. Zhu, L. Ji, L. Chen, Q. Sun, and D. W. Zhang, Nano Res. **15**, 2472–2478 (2022).
[196]Y. Wang, Z. Lv, J. Chen, Z. Wang, Y. Zhou, L. Zhou, X. Chen, and S.-T. Han, Adv. Mater. **30**, 1802883 (2018).
[197]H. Jiao, X. Wang, S. Wu, Y. Chen, J. Chu, and J. Wang, Appl. Phys. Rev. **10**, 011310 (2023).
[198]Z.-D. Luo, X. Xia, M.-M. Yang, N. R. Wilson, A. Gruverman, and M. Alexe, ACS Nano **14**, 746–754 (2020).
[199]Y. Jiang, L. Zhang, R. Wang, H. Li, L. Li, S. Zhang, X. Li, J. Su, X. Song, and C. Xia, ACS Nano **16**, 11218–11226 (2022).
[200]J. Du, D. Xie, Q. Zhang, H. Zhong, F. Meng, X. Fu, Q. Sun, H. Ni, T. Li, E.-j. Guo, H. Guo, M. He, C. Wang, L. Gu, X. Xu, G. Zhang, G. Yang, K. Jin, and C. Ge, Nano Energy **89**, 106439 (2021).
[201]P. Singh, S. Baek, H. H. Yoo, J. Niu, J.-H. Park, and S. Lee, ACS Nano **16**, 5418–5426 (2022).
[202]X. Li, S. Li, B. Tang, J. Liao, and Q. Chen, Adv. Electron. Mater. **8**, 2200343 (2022).
[203]K. Liu, T. Zhang, B. Dang, L. Bao, L. Xu, C. Cheng, Z. Yang, R. Huang, and Y. Yang, Nat. Electron. **5**, 761–773 (2022).
[204]Y. Cai, F. Wang, X. Wang, S. Li, Y. Wang, J. Yang, T. Yan, X. Zhan, F. Wang, R. Cheng, J. He, and Z. Wang, Adv. Funct. Mater. **33**, 2212917 (2023).
[205]J. Li, W. Fu, Y. Lei, L. Li, W. Zhu, and J. Zhang, ACS Appl. Mater. Interfaces **14**, 8587–8597 (2022).
[206]Y. Meng, F. Li, C. Lan, X. Bu, X. Kang, R. Wei, S. Yip, D. Li, F. Wang, T. Takahashi, T. Hosomi, K. Nagashima, T. Yanagida, and J. C. Ho, Sci. Adv. **6**, eabc6389 (2020).
[207]Y. Tan, H. Hao, Y. Chen, Y. Kang, T. Xu, C. Li, X. Xie, and T. Jiang, Adv. Mater. **34**, 2206816 (2022).
[208]M. Li, F.-S. Yang, H.-C. Hsu, W.-H. Chen, C. N. Kuo, J.-Y. Chen, S.-H. Yang, T.-H. Yang, C.-Y. Lin, Y. Chou, M.-P. Lee, Y.-M. Chang, Y.-C. Yang, K.-C. Lee, Y.-C. Chou, C.-H. Lien, C.-L. Lin, Y.-P. Chiu, C. S. Lue, S.-P. Lin, and Y.-F. Lin, Adv. Funct. Mater. **31**, 2007587 (2021).
[209]C. Zhang, S. Wang, X. Zhao, Y. Yang, Y. Tong, M. Zhang, Q. Tang, and Y. Liu, Adv. Funct. Mater. **31**, 2007894 (2021).
[210]T. Lim, S. Lee, J. Lee, H. Choi, B. Jung, S. Baek, and J. Jang, Adv. Funct. Mater. **33**, 2212367 (2023).
[211]M. Wang, S. Cai, C. Pan, C. Wang, X. Lian, Y. Zhuo, K. Xu, T. Cao, X. Pan, B. Wang, S.-J. Liang, J. J. Yang, P. Wang, and F. Miao, Nat. Electron. **1**, 130–136 (2018).
[212]F. Xue, C. Zhang, Y. Ma, Y. Wen, X. He, B. Yu, and X. Zhang, Adv. Mater. **34**, 2201880 (2022).
[213]A. S. Sokolov, M. Ali, R. Riaz, Y. Abbas, M. J. Ko, and C. Choi, Adv. Funct. Mater. **29**, 1807504 (2019).
[214]X. Tang, L. Yang, J. Huang, W. Chen, B. Li, S. Yang, R. Yang, Z. Zeng, Z. Tang, and X. Gui, npj Flexible Electron. **6**, 93 (2022).
[215]L. Liu, Z. Cheng, B. Jiang, Y. Liu, Y. Zhang, F. Yang, J. Wang, X.-F. Yu, P. K. Chu, and C. Ye, ACS Appl. Mater. Interfaces **13**, 30797–30805 (2021).
[216]R. Yu, X. Zhang, C. Gao, E. Li, Y. Yan, Y. Hu, H. Chen, T. Guo, and R. Wang, Nano Energy **99**, 107418 (2022).
[217]N. Li, Q. Wang, C. He, J. Li, X. Li, C. Shen, B. Huang, J. Tang, H. Yu, S. Wang, L. Du, W. Yang, R. Yang, D. Shi, and G. Zhang, ACS Nano **17**, 991–999 (2023).
[218]L. Mennel, J. Symonowicz, S. Wachter, D. K. Polyushkin, A. J. Molina-Mendoza, and T. Mueller, Nature **579**, 62–66 (2020).
[219]C. Choi, J. Leem, M. Kim, A. Taqieddin, C. Cho, K. W. Cho, G. J. Lee, H. Seung, H. J. Bae, Y. M. Song, T. Hyeon, N. R. Aluru, S. Nam, and D.-H. Kim, Nat. Commun. **11**, 5934 (2020).
[220]H. Shao, Y. Li, W. Yang, X. He, L. Wang, J. Fu, M. Fu, H. Ling, P. Gkoupidenis, F. Yan, L. Xie, and W. Huang, Adv. Mater. **35**, 2208497 (2023).
[221]R. Yu, L. He, C. Gao, X. Zhang, E. Li, T. Guo, W. Li, and H. Chen, Nat. Commun. **13**, 7019 (2022).
[222]Z. Zhang, S. Wang, C. Liu, R. Xie, W. Hu, and P. Zhou, Nat. Nanotechnol. **17**, 27–32 (2022).
[223]J. Chen, Z. Zhou, B. J. Kim, Y. Zhou, Z. Wang, T. Wan, J. Yan, J. Kang, J.-H. Ahn, and Y. Chai, Nat. Nanotechnol. **18**, 882–888 (2023).
[224]Q. Zhang, E. Li, Y. Wang, C. Gao, C. Wang, L. Li, D. Geng, H. Chen, W. Chen, and W. Hu, Adv. Mater. **35**, 2208600 (2023).
[225]H. Xiong, L. Xu, C. Gao, Q. Zhang, M. Deng, Q. Wang, J. Zhang, D. Fuchs, W. Li, A. Cui, L. Shang, K. Jiang, Z. Hu, and J. Chu, ACS Appl. Mater. Interfaces **13**, 50132–50140 (2021).
[226]B. Huang, N. Li, Q. Wang, C. Ouyang, C. He, L. Zhang, L. Du, W. Yang, R. Yang, D. Shi, and G. Zhang, Adv. Mater. Interfaces **9**, 2201558 (2022).
[227]F. Ma, Y. Zhu, Z. Xu, Y. Liu, X. Zheng, S. Ju, Q. Li, Z. Ni, H. Hu, Y. Chai, C. Wu, T. W. Kim, and F. Li, Adv. Funct. Mater. **30**, 1908901 (2020).
[228]D. Xie, K. Yin, Z.-J. Yang, H. Huang, X. Li, Z. Shu, H. Duan, J. He, and J. Jiang, Mater. Horiz. **9**, 1448–1459 (2022).

[229]S. Hong, S. H. Choi, J. Park, H. Yoo, J. Y. Oh, E. Hwang, D. H. Yoon, and S. Kim, ACS Nano **14**, 9796–9806 (2020).
[230]J. Yu, X. Yang, G. Gao, Y. Xiong, Y. Wang, J. Han, Y. Chen, H. Zhang, Q. Sun, and Z. L. Wang, Sci. Adv. **7**, eabd9117 (2021).
[231]M. Kumar, J. Lim, S. Kim, and H. Seo, ACS Nano **14**, 14108–14117 (2020).
[232]X. Hou, C. Liu, Y. Ding, L. Liu, S. Wang, and P. Zhou, Adv. Sci. **7**, 2002072 (2020).
[233]L. Sun, Z. Wang, J. Jiang, Y. Kim, B. Joo, S. Zheng, S. Lee, W. J. Yu, B.-S. Kong, and H. Yang, Sci. Adv. **7**, eabg1455 (2021).
[234]Y. Chen, Y. Kang, H. Hao, X. Xie, J. Zeng, T. Xu, C. Li, Y. Tan, and L. Fang, Adv. Funct. Mater. **33**, 2209781 (2023).
[235]M. Y. Tsai, K. C. Lee, C. Y. Lin, Y. M. Chang, K. Watanabe, T. Taniguchi, C. H. Ho, C. H. Lien, P. W. Chiu, and Y. F. Lin, Adv. Funct. Mater. **31**, 2105345 (2021).
[236]C. Wang, Q. Sun, G. Peng, Y. Yan, X. Yu, E. Li, R. Yu, C. Gao, X. Zhang, S. Duan, H. Chen, J. Wu, and W. Hu, Sci. China Mater. **65**, 3077–3086 (2022).
[237]Y.-X. Hou, Y. Li, Z.-C. Zhang, J.-Q. Li, D.-H. Qi, X.-D. Chen, J.-J. Wang, B.-W. Yao, M.-X. Yu, T.-B. Lu, and J. Zhang, ACS Nano **15**, 1497–1508 (2021).
[238]Q. Yang, Z.-D. Luo, D. Zhang, M. Zhang, X. Gan, J. Seidel, Y. Liu, Y. Hao, and G. Han, Adv. Funct. Mater. **32**, 202207290 (2022).
[239]J. Zhang, T. Sun, S. Zeng, D. Hao, B. Yang, S. Dai, D. Liu, L. Xiong, C. Zhao, and J. Huang, Nano Energy **95**, 106987 (2022).
[240]C.-M. Yang, T.-C. Chen, D. Verma, L.-J. Li, B. Liu, W.-H. Chang, and C.-S. Lai, Adv. Funct. Mater. **30**, 2001598 (2020).
[241]S. Wang, X. Pan, L. Lyu, C.-Y. Wang, P. Wang, C. Pan, Y. Yang, C. Wang, J. Shi, B. Cheng, W. Yu, S.-J. Liang, and F. Miao, ACS Nano **16**, 4528–4535 (2022).
[242]L. Yin, C. Han, Q. Zhang, Z. Ni, S. Zhao, K. Wang, D. Li, M. Xu, H. Wu, X. Pi, and D. Yang, Nano Energy **63**, 103859 (2019).
[243]J. Zhou, H. Li, M. Tian, A. Chen, L. Chen, D. Pu, J. Hu, J. Cao, L. Li, X. Xu, F. Tian, M. Malik, Y. Xu, N. Wan, Y. Zhao, and B. Yu, ACS Appl. Mater. Interfaces **14**, 35917–35926 (2022).
[244]W. He, Y. Fang, H. Yang, X. Wu, L. He, H. Chen, and T. Guo, J. Mater. Chem. C **7**, 12523–12531 (2019).
[245]Z.-C. Zhang, Y. Li, J.-J. Wang, D.-H. Qi, B.-W. Yao, M.-X. Yu, X.-D. Chen, and T.-B. Lu, Nano Res. **14**, 4591–4600 (2021).
[246]M. C. Sahu, S. Sahoo, S. K. Mallik, A. K. Jena, and S. Sahoo, Adv. Mater. Technol. **8**, 2201125 (2023).
[247]Y. Lian, J. Han, M. Yang, S. Peng, C. Zhang, C. Han, X. Zhang, X. Liu, H. Zhou, Y. Wang, C. Lan, J. Gou, Y. Jiang, Y. Liao, H. Yu, and J. Wang, Adv. Funct. Mater. **32**, 2205709 (2022).
[248]J. Tang, F. Yuan, X. Shen, Z. Wang, M. Rao, Y. He, Y. Sun, X. Li, W. Zhang, Y. Li, B. Gao, H. Qian, G. Bi, S. Song, J. J. Yang, and H. Wu, Adv. Mater. **31**, 1902761 (2019).
[249]K.-U. Demasius, A. Kirschen, and S. Parkin, Nat. Electron. **4**, 748–756 (2021).
[250]J. Feldmann, N. Youngblood, C. D. Wright, H. Bhaskaran, and W. H. P. Pernice, Nature **569**, 208–214 (2019).
[251]Y. van de Burgt, A. Melianas, S. T. Keene, G. Malliaras, and A. Salleo, Nat. Electron. **1**, 386–397 (2018).
[252]Y.-T. Li, J.-Z. Li, L. Ren, K. Xu, S. Chen, L. Han, H. Liu, X.-L. Guo, D.-L. Yu, D.-H. Li, L. Ding, L.-M. Peng, and T.-L. Ren, ACS Appl. Mater. Interfaces **14**, 28221–28229 (2022).
[253]S. Wang, C.-Y. Wang, P. Wang, C. Wang, Z.-A. Li, C. Pan, Y. Dai, A. Gao, C. Liu, J. Liu, H. Yang, X. Liu, B. Cheng, K. Chen, Z. Wang, K. Watanabe, T. Taniguchi, S.-J. Liang, and F. Miao, Natl. Sci. Rev. **8**, nwaa172 (2021).
[254]X. Zhu, C. Gao, Y. Ren, X. Zhang, E. Li, C. Wang, F. Yang, J. Wu, W. Hu, and H. Chen, Adv. Mater. **35**, 2301468 (2023).
[255]L. Liu, W. Xu, Y. Ni, Z. Xu, B. Cui, J. Liu, H. Wei, and W. Xu, ACS Nano **16**, 2282–2291 (2022).
[256]J.-L. Meng, T.-Y. Wang, L. Chen, Q.-Q. Sun, H. Zhu, L. Ji, S.-J. Ding, W.-Z. Bao, P. Zhou, and D. W. Zhang, Nano Energy **83**, 105815 (2021).
[257]R. A. John, F. Liu, N. A. Chien, M. R. Kulkarni, C. Zhu, Q. Fu, A. Basu, Z. Liu, and N. Mathews, Adv. Mater. **30**, 1800220 (2018).
[258]Y. Nie, P. Xie, X. Chen, C. Jin, W. Liu, X. Shi, Y. Xu, Y. Peng, J. C. Ho, J. Sun, and J. Yang, J. Semicond. **43**, 112201 (2022).
[259]Y. Chen, W. Qiu, X. Wang, W. Liu, J. Wang, G. Dai, Y. Yuan, Y. Gao, and J. Sun, Nano Energy **62**, 393–400 (2019).
[260]J. Bian, Z. Cao, and P. Zhou, Appl. Phys. Rev. **8**, 041313 (2021).
[261]Z. Xu, F. Li, C. Wu, F. Ma, Y. Zheng, K. Yang, W. Chen, H. Hu, T. Guo, and T. W. Kim, NPG Asia Mater. **11**, 18 (2019).
[262]R. A. John, Y. Demirağ, Y. Shynkarenko, Y. Berezovska, N. Ohannessian, M. Payvand, P. Zeng, M. I. Bodnarchuk, F. Krumeich, G. Kara, I. Shorubalko, M. V. Nair, G. A. Cooke, T. Lippert, G. Indiveri, and M. V. Kovalenko, Nat. Commun. **13**, 2074 (2022).
[263]M. Mustaqeem, J.-Y. Lin, S. Kamal, A. Thakran, G.-Z. Lu, G. Naikoo, P.-T. Chou, K.-L. Lu, and Y.-F. Chen, ACS Appl. Mater. Interfaces **14**, 26895–26903 (2022).
[264]G. Moon, S. Y. Min, C. Han, S.-H. Lee, H. Ahn, S.-Y. Seo, F. Ding, S. Kim, and M.-H. Jo, Adv. Mater. **35**, 2203481 (2023).
[265]J. Wang, Z. Lv, X. Xing, X. Li, Y. Wang, M. Chen, G. Pang, F. Qian, Y. Zhou, and S.-T. Han, Adv. Funct. Mater. **30**, 1909114 (2020).
[266]R. Li, W. Wang, Y. Li, S. Gao, W. Yue, and G. Shen, Nano Energy **111**, 108398 (2023).
[267]X. Han, Y. Zhang, Z. Huo, X. Wang, G. Hu, Z. Xu, H. Lu, Q. Lu, X. Sun, L. Qiu, P. Yan, and C. Pan, Adv. Electron. Mater. **9**, 2201068 (2023).
[268]F. Luo, Y. Wu, J. Tong, F. Tian, and X. Zhang, Nano Res. **16**, 10108–10119 (2023).
[269]Y. Zhang, Z. Wang, J. Zhu, Y. Yang, M. Rao, W. Song, Y. Zhuo, X. Zhang, M. Cui, L. Shen, R. Huang, and J. J. Yang, Appl. Phys. Rev. **7**, 011308 (2020).
[270]C. Chen, X. Chen, X. Wu, X. Wang, Y. Ping, X. Wei, X. Zhuo, J. Lu, L. Zhu, J. Zhou, T. Zhai, J. Han, and H. Xu, Adv. Mater. **34**, 2107512 (2022).
[271]W. Zhu, C. Song, Q. Wang, H. Bai, S. Yin, and F. Pan, Natl. Sci. Rev. **10**, nwac173 (2023).
[272]Y. Xia, X. Chen, J. Wei, S. Wang, S. Chen, S. Wu, M. Ji, Z. Sun, Z. Xu, W. Bao, and P. Zhou, Nat. Mater. **22**, 1324–1331 (2023).
[273]J. Wang, N. Ilyas, Y. Ren, Y. Ji, S. Li, C. Li, F. Liu, D. Gu, and K. Ang, Adv. Mater. 2307393 (2023).
[274]W. Zhang, R. Mazzarello, M. Wuttig, and E. Ma, Nat. Rev. Mater. **4**, 150–168 (2019).